Production of Free Surface Water Jets Using Focused Underwater Shock Waves

Hilton Karnovsky

A research report submitted to the Faculty of Engineering, University of the Witwatersrand, in partial fulfilment of the requirements for the degree of Master of Science in Engineering.

Johannesburg 2000

Declaration

This report is submitted in partial fulfilment of the requirements for the degree of Master of Science in Engineering at the University of the Witwatersrand, Johannesburg, South Africa. All work contained therein reflects the efforts of the undersigned person only and not any other unless so acknowledged. In compiling this report, no form of copyright has been infringed.

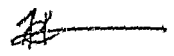

12 September 2000

H. Karnovsky
9407841/F

Abstract

It is possible to produce concentrated free surface water jets by rapidly accelerating a geometrically shaped curved deflector plate below the free water surface. This principle has been established using a self focusing electromagnetic acoustic source (FEMAS) and this report verifies it using a shock tube based mechanical analogue of that system. The shape, form and speed of the water jets produced vary between the two systems. Discrete pressure measurements using a needle hydrophone positioned at different points below the free water surface are presented. The variation in pressure amplitudes recorded highlight the scatter and uncertainty inherent in a complex coupled system, while the form of the pressure trace is dependant on the mechanical design of the system in use and the position of the needle hydrophone in the pressure field. To better understand the experimental system, a computer simulation using commercially available non-linear dynamic analysis software has been developed. This shows that the water surface jets result from the overall hydrodynamic flow initiated by rapid movement of the deflector plate below the water surface.

Acknowledgement

Over the past two years it has been my honour and privilege to work with Professor B.W Skews, one of South Africa's pre-eminent scientists. Without his knowledge, support and dedication this project would not have been possible. It has indeed been special to work with a man of such calibre and learning. May the Flow Research group, of which I have been a member, go from strength to strength. The support of the University of the Witwatersrand and the Foundation for Research and Development are gratefully acknowledged.

Many thanks to Mike Draxl and all the workshop staff who unselfishly gave of their time and expertise. Many other people have offered me help along the way and I thank them all.

Words cannot express my gratitude to my family – I hope I have done you proud.

Table of Contents

Table of Contents

Table of Contents

Page

List of figures

List of figures

List of figures

1. Introduction

A shock wave is a strong pressure wave in any elastic medium, such as a solid or fluid, which results from a violent pressure change. Such pressure change may be the result of an explosion, solid object moving with high velocity, lightning or any other process which causes a zone of high pressure to propagate through a medium at supersonic speed. As shown below, the shock propagates outwards from its source into the undisturbed material leaving behind a zone of disturbed material.

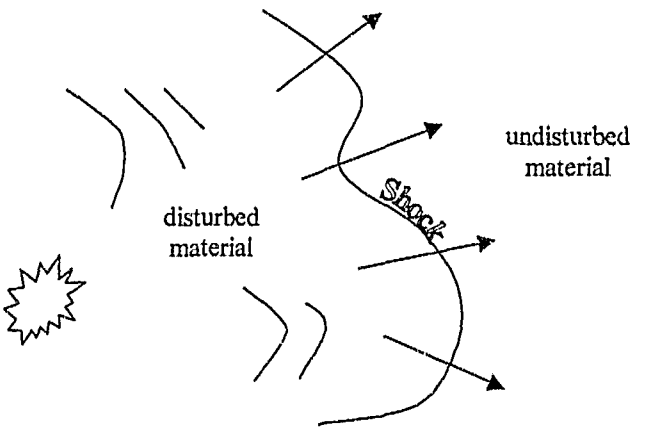

(a)

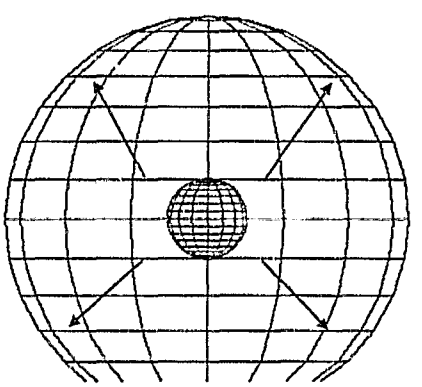

(b)

Figure 1.1 (a) Schematic propagation of a shock front
(b) Propagation of a spherical shock front

Theory shows that a stable shock front is a region in which temperature, density and flow velocity change their values in a few mean free paths (Wright 1961). As a result, these quantities are generally regarded as changing discontinuously at the shock.

1.1 Study of shock waves

The general study of shock wave phenomena began in earnest after the second world war. Since then, the shock tube in various forms has become the most commonly used experimental tool in this field. Shock tubes provide repeatable controlled shocks which can be used to gather reliable experimental data.

A basic shock tube consists of a rigid cylinder divided into two sections by a gas-tight diaphragm. A pressure difference is applied across the diaphragm and allowed to normalise. When the diaphragm is ruptured a shock wave travels into the low pressure (expansion) chamber, and a rarefaction wave travels into the high pressure (compression) chamber.

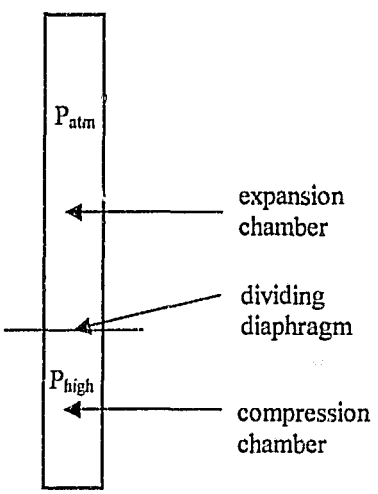

Figure 1.2 Schematic diagram of a basic shock tube

1.2 Pressure waves in a tube of constant cross section

The following theory allows one to examine the propagation of a pressure pulse in a stationary gas, enclosed in a tube of constant cross sectional area.

The speed of a sound wave in a gas is given by:

$$c = \sqrt{\frac{\gamma R_0 T}{M}} = \sqrt{\gamma R T}$$

Where: c = Speed of sound wave in a gas (m/s)
γ = Ratio of specific heats of gas in which sound wave propagates
R_0 = Universal gas constant (J/kg mol K)
M = Molecular weight
T = Temperature (K)
R = Gas constant (J/kg K)

This formula is based on the assumption that the propagated disturbances are sufficiently weak for all pressure and density variations to be negligible. When the strength of the disturbance is substantial enough for this assumption not to hold, two factors influence the speed of propagation. Firstly the disturbance compresses the gas, causing its temperature and hence its sound speed to rise. Thus the peak of a compression wave travels more quickly than the speed of sound in the undisturbed gas. Secondly there is a particle flow in the wave. As a result, the peak of the compression wave travels at an increased sound speed in fast moving air and hence its velocity of propagation relative to a stationary observer is increased. To facilitate mathematical analysis of these effects a new quantity (f) is defined.

$$f = \int_{\rho_0}^{\rho} c \frac{d\rho}{\rho}$$

$$e = e(p, \rho)$$

Where: ρ_0 = density of air into which the wave is travelling (kg/m^3)

Then: $\frac{\partial f}{\partial x} = \frac{c}{\rho}\frac{\partial \rho}{\partial x}$ and $\frac{\partial f}{\partial t} = \frac{c}{\rho}\frac{\partial \rho}{\partial t}$

Using the adiabatic expression that for a given fluid element $p\rho^{-\gamma}$ is constant, then:

$$\frac{\partial p}{\partial x} = \frac{\gamma p}{\rho}\frac{\partial \rho}{\partial x} = c^2 \frac{\partial \rho}{\partial x} = \rho c \frac{\partial f}{\partial x}$$

For a constant cross-sectional area (A), the equations of conservation of mass and momentum respectively may be written as:

$$\frac{\partial \rho}{\partial t} + \rho \frac{\partial u}{\partial x} + u \frac{\partial \rho}{\partial x} = 0$$

and $$\frac{\partial u}{\partial t}+u\frac{\partial u}{\partial x}+\frac{1}{\rho}\frac{\partial p}{\partial x}=0$$

These may be written in terms of (f) as:

$$\frac{\partial f}{\partial t}+c\frac{\partial u}{\partial x}+u\frac{\partial f}{\partial x}=0 \qquad (1.1)$$

and $$\frac{\partial u}{\partial t}+u\frac{\partial u}{\partial x}+c\frac{\partial f}{\partial x}=0 \qquad (1.2)$$

Adding and subtracting equations (1.1) and (1.2):

$$\frac{\partial}{\partial t}(f+u)+(u+c)\frac{\partial}{\partial x}(f+u)=0 \qquad (1.3)$$

and $$\frac{\partial}{\partial t}(f-u)+(u-c)\frac{\partial}{\partial x}(f-u)=0 \qquad (1.4)$$

These are the equations of propagation of waves in the direction of $(+x)$ with velocities (u+c) and (u-c) respectively. Equation (1.3) means that if a point travels with a velocity (u+c) then the value of the quantity (f+u) at that point will be constant. Similarly equation (1.4) means that the quantity (f-u) will be constant at a point travelling with velocity (u-c). The quantities (f+u) and (f-u) are known as the Riemann Invariants.

By definition: $$f=\int_{P_0}^{\rho} c\frac{d\rho}{\rho} \quad \text{and} \quad e=e(p,\rho) \qquad (1.5)$$

Using the relations $p\rho^{-\gamma}=k$ and $c=\sqrt{\left(\frac{\gamma p}{\rho}\right)}$

Equation (1.5) becomes: $$f=\frac{2c_0}{\gamma-1}\left\{\left(\frac{p}{p_0}\right)^{\left(\frac{\gamma-1}{2\gamma}\right)}-1\right\} \qquad (1.6)$$

Similarly the sound speed c may be rewritten as:

$$c=c_0\left(\frac{p}{p_0}\right)^{\left(\frac{\gamma-1}{2\gamma}\right)} \qquad (1.7)$$

Now consider the propagation of a pressure disturbance in what is elsewhere a uniform stationary gas. The pulse separates into two parts. The first represents a right travelling pressure wave with velocity (u+c) and the second a left travelling pressure wave with velocity (u-c). Concentrating on the right travelling wave, a point which is

initially in the undisturbed region ahead of the wave and travelling with velocity (u-c) will eventually be overtaken by the disturbed region travelling with velocity (u+c). But relation (1.4) applies to all points travelling with velocity (u-c). Hence all points ahead of the right travelling pressure wave are points of constant (f-u). Since the wave is moving through an initially undisturbed gas where f=0 and u=0, it follows that at every point in the wave:

$$u = f = \frac{2c_0}{\gamma - 1}\left\{\left(\frac{p}{p_0}\right)^{\left(\frac{\gamma-1}{2\gamma}\right)} - 1\right\} \qquad (1.8)$$

This equation gives the particle velocity as a function of pressure in the wave. The fact that the particle velocity is directed in the direction of propagation in a compression wave ($p \rangle p_0$) and against the direction of propagation in a rarefaction wave ($p \langle p_0$) follows at once from equation (1.8).

Using equations (1.7) and (1.8) the velocity of propagation of the wave can be found.

$$(u + c) = c_0\left\{\frac{\gamma + 1}{\gamma - 1}\left(\frac{p}{p_0}\right)^{\left(\frac{\gamma-1}{2\gamma}\right)} - \frac{2}{\gamma - 1}\right\} \qquad (1.9)$$

It follows that when the wave is weak, the velocity of propagation tends to c_0 - the velocity of sound in the undisturbed gas. It also follows that waves may be propagated at speeds considerably in excess of the velocity of sound provided they are sufficiently strong.

Furthermore, the waves change shape as they propagate. In a rarefaction wave, the pressure gradients tend to become less steep. In a compression wave, the pressure gradients tend to become more steep.

These processes can be shown as follows. Consider the rarefaction wave shown in figure 1.3(a). The velocity of propagation of that part of the wave at pressure (p) is given by equation (1.9). The arrows indicate the direction of particle flow, which is opposite to the direction of wave propagation. Since the part of the wave at high pressure travels more quickly than that at low pressure, the rarefaction wave necessarily becomes less steep as it propagates.

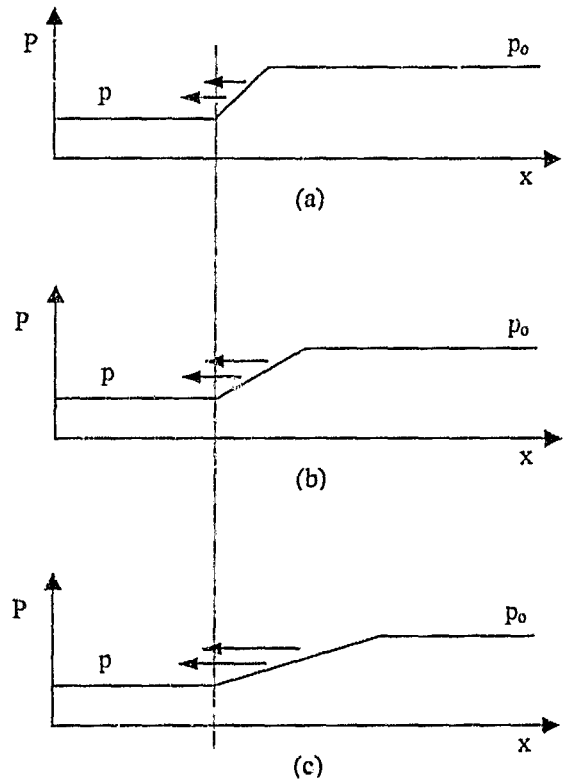

Note: Arrows indicate direction of particle flow

Figure 1.3 Propagation of a rarefaction wave

Similar arguments lead to the rule about the change in shape of a compression wave. That part of the wave at high pressure travels more quickly than the part at low pressure and so the wave steepens as it propagates. This is shown in the next figure:

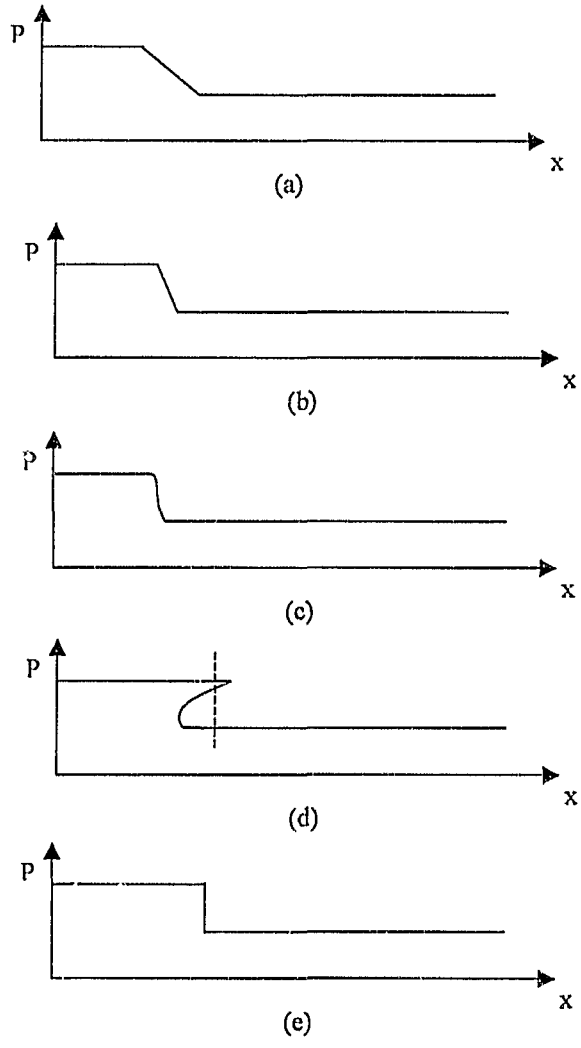

Figure 1.4 Propagation of a compression wave

If the process of the high pressure region overtaking the low pressure region carried on for some time, the situation shown in figure 1.4(d), where the high pressure region has caught and overtaken the low pressure region, would occur. However three pressures cannot simultaneously exist at one point in space. Instead a stable system results in which a shock front is formed. The wave shape is shown in figure 1.4(e).

In front of and behind the shock, changes occur sufficiently slowly for the theory already developed to apply, but separate theory needs to be developed which describes the behaviour at the shock itself.

1.3 The theory of shock waves

The conditions across a shock are evaluated on the basis that the thickness of the shock front is constant – i.e. the wave does not change shape as it propagates. The shock front does not necessarily need to be thin. Consider a shock front moving into still air with velocity (U). The pressure, temperature, density, internal energy per unit mass of gas and sound speed in front and behind the shock are represented by $p_0, p_1, T_0, T_1, \rho_0, \rho_1, e_0, e_1, c_0, c_1$ respectively. The flow velocity behind the shock is represented by (u). The following parameters are defined:

Shock strength: $$y = \left(\frac{p_1}{p_0}\right) \tag{1.10}$$

Shock compression: $$\eta = \left(\frac{\rho_1}{\rho_0}\right) \tag{1.11}$$

Shock Mach number: $$M = \left(\frac{U}{c_0}\right) \tag{1.12}$$

Consider the figure below as seen by an observer travelling at the same speed as the shock front.

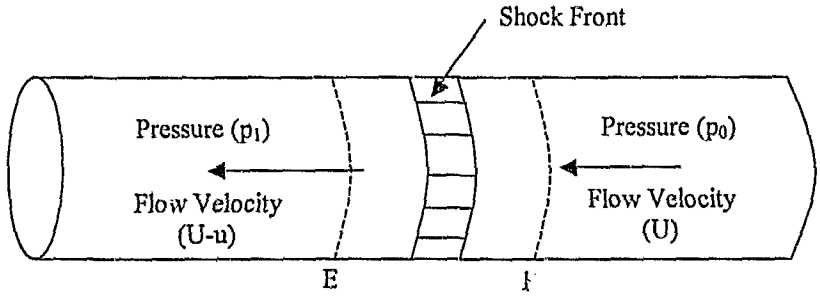

Figure 1.5 Shock front moving through a gas

Dividing the gas at points E and F in front of and behind the shock wave respectively, and examining the forces acting on region EF which contains the shock transition, the following can be deduced:

(a) The quantity of gas flowing into the transition region in time dt is $\rho_0 UAdt$ and that flowing out is $\rho_1(U-u)Adt$. By the law of conservation of matter:

$$\rho_0 U = \rho_1(U-u) = m \tag{1.13}$$

(b) The net force acting on the element EF is $(p_1 - p_0).1$. This must equal the rate of change of momentum of the gas inside the element which is (muA). Hence:

$$mu = p_1 - p_0 \tag{1.14}$$

(c) The net work done on the element EF in time dt can be equated to the increase in kinetic and internal energy of the gas passing through the shock front in time dt. This yields:

$$p_0 U + me_0 + \frac{1}{2}mU^2 = p_1(U-u) + me_1 + \frac{1}{2}m(U-u)^2 \tag{1.15}$$

Furthermore the internal energy of the gas in which the shock propagates is known as a function of pressure and density.

$$e = e(p, \rho)$$

The three dynamic equations (1.13 – 1.15) have become known as the Rankine Hugonoit relations.

For an ideal gas, where the ratio of specific heat at constant pressure to that at constant volume, γ, is a constant, the following is an expression for the internal energy of the gas:

$$e = \frac{p}{(\gamma - 1)\rho} \tag{1.16}$$

This equation facilitates solution of the Rankine Hugonoit relations. Assuming the pressure ratio given by equation (1.10) across the shock is specified, the unknowns U, u, ρ can be found. Remembering the equations for η, M, c_o the following solutions can be found:

$$\frac{U}{c_0} = M = \sqrt{\frac{(\gamma + \mu)}{(1 + \mu)}} \tag{1.17}$$

$$\frac{u}{c_0} = \frac{(1-\mu)(\gamma - 1))}{\sqrt{[(1+\mu)(\gamma + \mu)]}} \tag{1.18}$$

$$\frac{\rho_1}{\rho_0} = \eta = \frac{(\mu + \gamma)}{(1 + \mu\gamma)} \tag{1.19}$$

$$\frac{T_1}{T_0} = \gamma \frac{(1 + \mu\gamma)}{(\mu + \gamma)} \tag{1.20}$$

Where: $$\mu = \frac{(\gamma - 1)}{(\gamma + 1)} \tag{1.21}$$

1.4 Shock waves in liquids

The preceding sections have considered shock waves in gases; However in recent years liquid shock waves have made practical contributions to the sciences of medicine and metal forming. To study the effects of shock waves in liquids, it is necessary to relate pressure and density across a shock wave propagating through a liquid by an equation of state. (Thus far all analyses have been based on the basic equation of state for an ideal gas $pv = RT$)

In general, an equation of state can be expressed as:

$$\left(\frac{p}{p_0}\right) = \left(\frac{\rho}{\rho_0}\right)^{\varsigma} \tag{1.22}$$

Where: p = Instantaneous pressure (Pa)
p_0 = Hydrostatic pressure under ambient, zero velocity conditions (Pa)
ρ = Instantaneous density (kg/m^3)
ρ_0 = Equilibrium density (kg/m^3)

The exponent ς is a constant which depends on the nature of the medium and how the compression or expansion is carried out. The value of ς can be found empirically or by using the non-linear acoustic relationship (Mortimer 1997).

1.5 Equation of state for water

The modified Tait equation of state is used for shock pressures in water of less than 10kBar. It is based on the assumption that:

$$\rho(p,T) = \rho(0,T)(1 + \frac{p}{B})^{\frac{1}{n}} \tag{1.23}$$

and therefore

$$\frac{p_2 + B}{p_1 + B} = \left(\frac{\rho_2}{\rho_1}\right)^n \tag{1.24}$$

The constants B and n are characteristic constants of the medium, which are empirically determined. Actually B is a weak function of entropy, but can be considered a constant for moderate to weak shock waves in water. For the purposes of this report, B = 2955Bar = 295.5MPa and n = 7.44 are used (Mortimer 1997).

Shock waves in liquid can be described using the same equations as those for shock waves in air if the pressure p is replaced by $p' = p + B$ and the ratio γ is replaced by n. The following hydrodynamic relations can then be used (Mortimer 1997).

Shock wave speed: $$c = \sqrt{\frac{nB}{\rho_0}\left(\frac{p'}{B}\right)^{\left(\frac{n-1}{n}\right)}} \quad (1.25)$$

Acoustic velocity: $$c_0 = \sqrt{\frac{n(pB)}{\rho_0}} \quad (1.26)$$

Mach number for a shock wave in water:

$$M_s = \frac{V_s}{c_1} = \sqrt{\frac{(n+1)p'_{21} + (n-1)}{2n}} \quad (1.27)$$

Where: $$p'_{21} = \left(\frac{p_2 + B}{p_1 + B}\right) \quad (1.28)$$

p_1 = Pressure in undisturbed region ahead of shock (Pa)
p_2 = Pressure in disturbed region behind shock (Pa)

In water p'_{21} is generally close to unity because of the large values of B in equation (1.28). This leads to a shock Mach number also close to unity. As a result, hydrodynamic shocks are generally weak in the gasdynamic sense.

1.6 Production of liquid shock waves

Liquid shock waves can be of two types. Either continuous pressure oscillations or transient pressure pulses. Pressure oscillations usually offer low peak pressures and are thus not considered further. A number of techniques are available for producing transient pressure pulses.

1.6.1 Electrical spark discharges:

These shock wave generators work on the principle that by a sudden release of energy in a small volume a plasma is generated and expands, thereby emitting a shock wave. In nature a corresponding phenomenon is the thunderstorm, where an electric discharge seen as lightning is followed by an acoustic boom heard as thunder.

To generate the exploding plasma channel experimentally, a high voltage capacitor is typically discharged across electrodes in water. One such experimental configuration is detailed by Müller (1987).

1.6.2 Underwater explosions:
The detonation of submerged explosive charges is a well documented source of strong liquid shock waves (Kedrinskii 1978). By employing various charge shapes, different shock wave profiles result. A disadvantage of this method is the rising bubble of explosion products, resulting from the detonation, which can interfere with experimental results.

1.6.3 High power lasers or optoelectronic sources:
High power laser pulses can be used to cause localised heating in a fluid. The resulting expansion causes a spherical shock wave to propagate through the fluid. An alternative is to use a high power laser to impinge on a disk emitting a unipolar or bipolar pulse. This type of transducer is known as an optoacoustic source (Mortimer 1997).

1.6.4 Liquid shock tubes:
Shock tubes as described earlier have become the most commonly used tool for the study of gas shock waves. The liquid (hydrodynamic) shock tube produces shock waves in a liquid medium. It operates on a similar principle to a gas shock tube. In its most basic form, it is vertically mounted with a compression chamber at its top, middle expansion section and lower liquid filled test section. The compression and expansion chambers are separated by a diaphragm across which a pressure difference is applied. When the diaphragm is ruptured, a shock wave moves down the expansion chamber striking the air/liquid interface at its end. A transmitted shock propagates through the liquid test section. Variations on this basic configuration exist as required to suit individual test requirements. For the production of strong shock waves, a gas driven piston can be used to strike the free liquid surface. An alternative method to produce shock waves in a liquid is through the collision of submerged solid bars.

1.6.5 Electromagnetic emitters:
An electromagnetic acoustic source (EMAS) is shown schematically below.

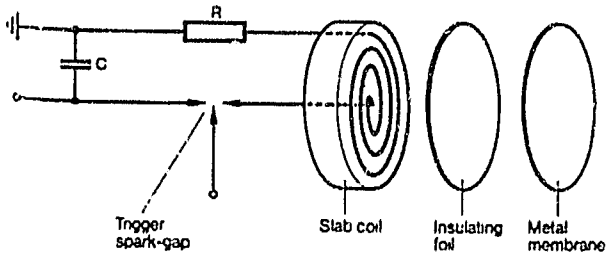

Figure 1.6 Electromagnetic acoustic source (Reichenberger (1988))

This device consists of a high voltage capacitor which is discharged through a flat pancake coil. An insulated metal disk is in close proximity with the coil. Lorentz forces produced by the eddy currents induced in the disk accelerate it away from the

coil. The disk acceleration produces a pressure pulse in a fluid filled cavity (Mortimer 1997).

1.7 General behaviour of shock waves

1.7.1 Reflection and diffraction

Shock waves reflect from hard material surfaces in one of two different configurations. For weak shock waves, where non-linearity is relatively weak, when the interface is relatively steep the reflection is regular. The reflected shock joins the incident shock at the surface. The angle of incidence is equal to the angle of reflection. On the other hand, irregular reflection occurs when the shock is strong and the slope of the surface gradual. This is called Mach reflection. For strong shock waves regular reflection can occur, but in this case the angle of incidence is not equal to the angle of reflection.

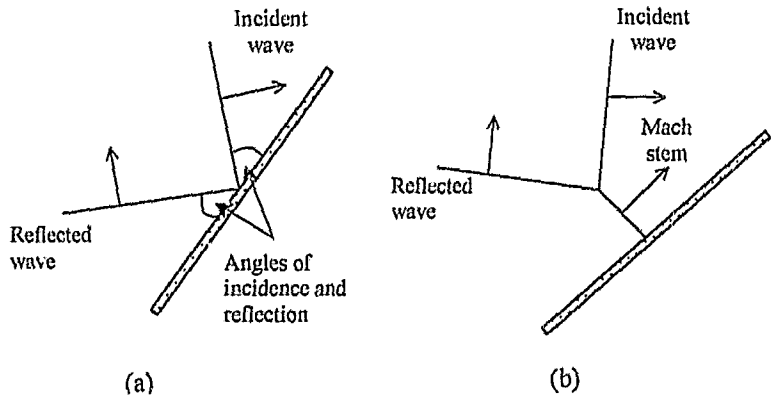

Figure 1.7 Reflection of a shock wave at a solid surface: (a) regular reflection (b) Mach reflection

For weak shock waves, the theory of shock reflection yields no solution at small angles of incidence. This was called the von Neumann paradox. Experiments show that in fact a type of Mach reflection occurs (Ben-Dor 1992) where the reflected shock starts out as a compression wave, and the phenomenon is now called von Neumann reflection.

Diffraction occurs when the length of a shock front increases as a result of its interaction with a solid body. The figure below shows a shock wave diffracting around a 90° corner.

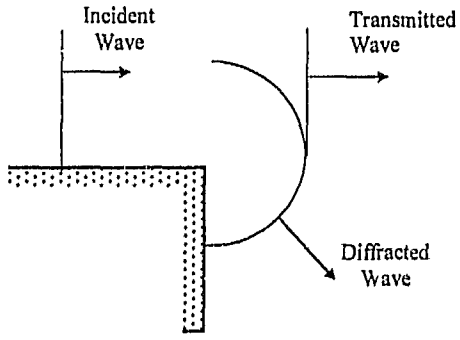

Figure 1.8 Diffraction of a shock wave around a 90° corner

The lower branch of the diffracted wave is compressive, and the upper part above the extension of the horizontal wall, is expansive. If the incident shock is of finite amplitude, the diffracted wave propagates laterally upwards along the shock, so the effect of the corner is communicated to the region above the extension of the horizontal wall.

1.7.2 Refraction

Refraction occurs when a shock wave is bent by material inhomogenuities or at material interfaces. Generally when a shock wave refracts, it also reflects. Both regular and irregular refraction occur, depending on shock strength and the interface properties. These processes are shown in the figure below:

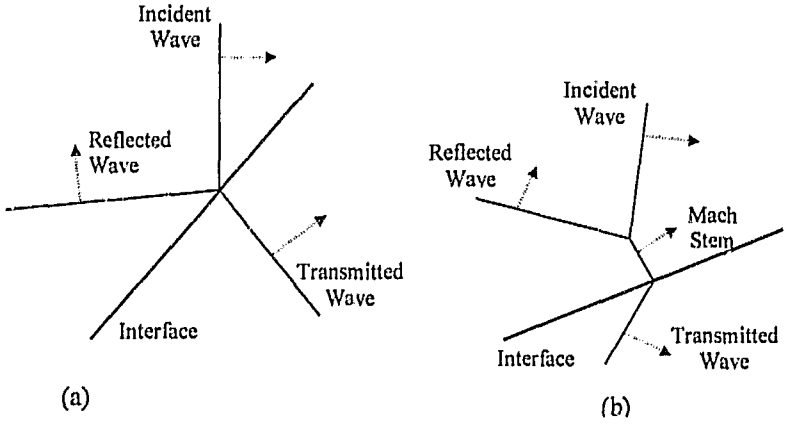

Figure 1.9 Refraction of shock waves from an interface (a) Regular refraction (b) Irregular refraction

The direction in which the shock front bends at the material interface depends on the speed of sound in the two materials. In the most basic analysis, when the shock wave moves from a slow into a fast sound speed material, the transmitted shock bends upstream of the incident shock.

1.7.3 Scattering and attenuation

Scattering occurs by the reflection and refraction of waves from small, randomly distributed non-uniformities in the propagation medium. The reflected waves are called "back scattered" waves and the transmitted waves "forward scattered". Forward scattering manifests itself as either perturbations of amplitude and shape of the main shock front or a field of wavelets a short distance behind the shock propagating parallel to the shock path. Back scattered waves can both re-reflect from the medium and also nonlinearly overtake the incident wave, tending to restore its strength.

Viscous dissipation in shock waves does not directly affect their strength, only their thickness. The strength of shocks is influenced only by waves/disturbances generated at the front or those generated downstream which overtake it. Downstream disturbances which affect shock strength can be generated by viscous boundary layers. Here the displacement effect induces weak expansion waves which overtake the shock and attenuate it.

1.8 Focusing of shock waves

Plane shock waves are deformed by propagation through non-uniform or moving media, or when they reflect from curved surfaces such as ellipsoids. Such waves, once formed, tend to converge and focus. They can acquire both concave and convex curvatures, as shown below (see Chapter 2 for more details):

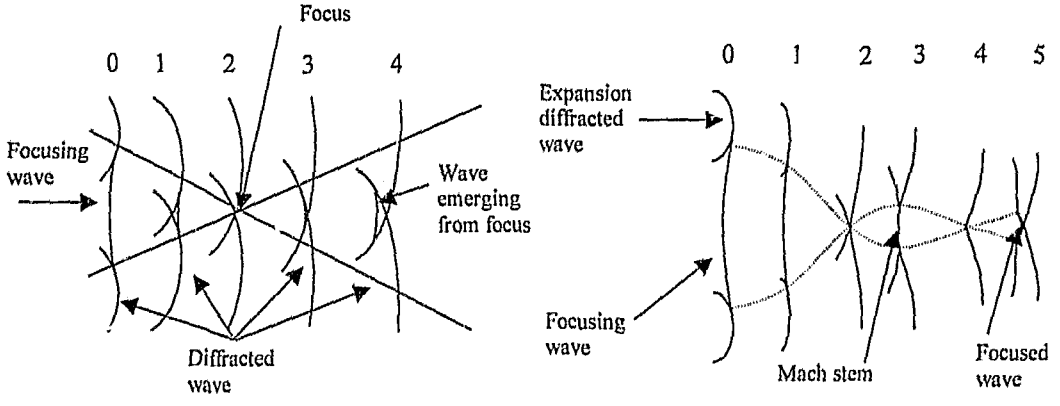

Figure 1.10 Focusing of an acoustic shock

The convex curvatures are diffracted waves while the concave curvatures are the focusing waves. The diffracted waves are expansion waves, separating the surrounding lower pressure fluid from the focused front. In acoustic theory all the focusing rays converge to a point. Therefore at the focus the amplitude is infinite.

Beyond the focus, since the focused wave travels a longer distance than the diffracted waves, it falls behind them and the front folds at a cusp (see figure 1.10 (a)). The behaviour of weak shocks in real liquids differs from that predicted by theory. The real focused pressure amplitudes achievable are limited by small non-linearities in the medium. The diffracted waves propagate laterally along the shock front and they cross on the axis of symmetry (see figure 1.10 (b)), before the focusing shock reaches the geometric focus. The inner parts of the diffracted fronts near the axis steepen and become compressive before stage 2 (see figure 1.10 (b)). The converging fronts are unstable and form sharp corners as in Mach reflection. The same instability manifests itself on focusing fronts; The compressive diffracted waves become the reflected waves of a Mach reflection about the axis of symmetry. The focusing front plays the role of the incident wave of the Mach reflection. The strongest wave at focus is the Mach stem shown in figure 1.10(b). Thus non-linearity limits the development of the infinite amplitude predicted by acoustic theory to the strength of a Mach stem.

A number of devices have been used to generate focused shock waves. The most simple method used experimentally is to reflect a plane shock from a curved (elliptical/parabolic) surface inserted at the end of a shock tube. The effect is to reverse the direction of propagation of the shock wave and introduce a curvature which focuses the shock at the geometrical focus of the reflector used.

Other experimental shock wave focusing techniques are outlined below:

1.8.1 Electromagnetic shock wave generators

Mortimer (1997) details the construction of a self focusing electromagnetic acoustic source (FEMAS). This was intended to produce a converging shock wave, thus eliminating the need for external concentrators such as lenses or reflectors. Pressure measurements in the field of the FEMAS units show that the shock wave generated did in fact converge. The effect of changing the concave disk geometries was also investigated. It was found that the limit of pressure amplification in these tests was diffraction (Mortimer 1997).

The figure below show the pressure traces recorded at the focus of the FEMAS in different media.

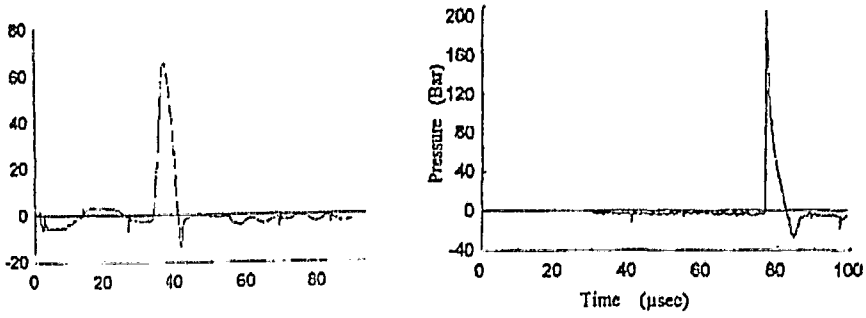

Figure 1.11 Pressure traces recorded at the focus of the FEMAS in (a) Water (b) FC-43 (Mortimer 1997)

Another configuration which can be used to focus the shock wave produced by an electromagnetic generator is shown below.

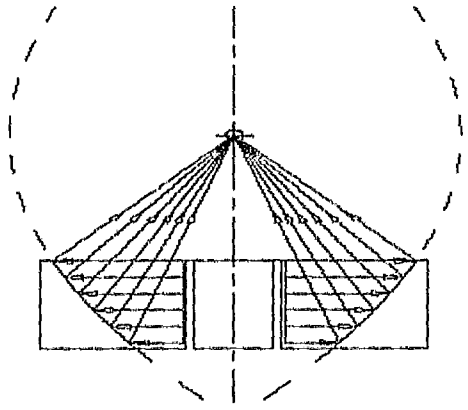

Figure 1.12 Cylindrical electromagnetic generator enclosed in a parabolic reflector (http://www.galcit.caltech.edu/ ~brad/bioscience/litho/workshop/endo/endo_2.html)

A cylindrical electromagnetic generator is enclosed in a parabolic reflector. The parabola is rotated about its central axis to form a three dimensional reflecting surface. Only a small segment of the parabola is used however, and the shock focuses to a point that otherwise would have been inside the surface of revolution. In figure 1.12 the arrows show the parallel horizontal rays of the expanding cylindrical shock leaving the shock generator and their paths converging towards the focus of the parabolic section after reflection.

1.8.2 Piezoelectric shock wave generators:
(http://www.galcit.caltech.edu/ ~brad/bioscience/litho/workshop/endo/endo_2.html)

Piezoelectric elements can be arranged on a spherical surface to generate a focusing shock wave when a voltage is applied across them. The shock focuses at the centre of the sphere. This type of arrangement is shown below:

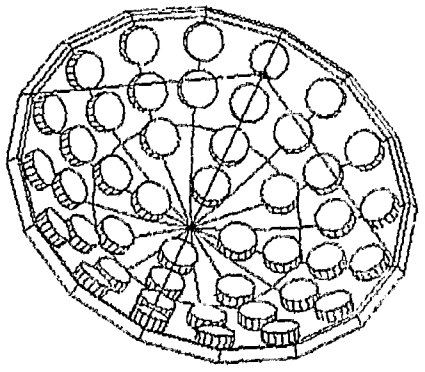

Figure 1.13 Piezoelectric shock wave source

1.9 The production of free surface water jets using focused underwater shock waves

Mortimer (1997) showed that it is possible to produce concentrated free surface water jets using focused underwater shock waves created by an FEMAS.

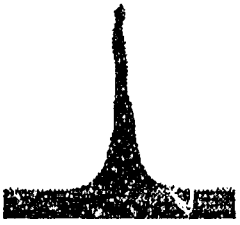

Figure 1.14 Free surface water jet produced using an FEMAS (Mortimer 1997)

Similarly in a previous work which is not available in the public domain, the author has shown that it is possible to produce free surface water jets using a mechanical analogue of the FEMAS used by Mortimer (Karnovsky 1998) – See Appendix A1.

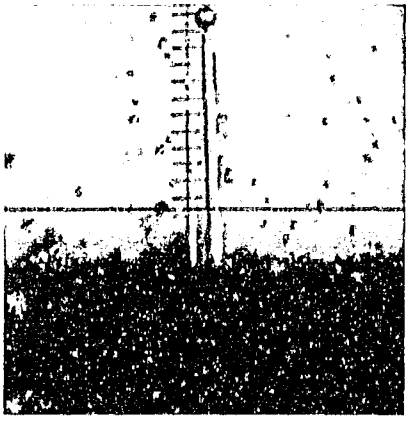

Figure 1.15 Free surface water jet using mechanical analogue of FEMAS (Karnovsky 1998)

In this system it is necessary to rapidly accelerate a curved plate below a free water surface through a small distance (±5mm). An efficient way to achieve this is to allow a gas shock wave to strike a constrained but flexibly mounted curved plate from below, thereby loading it impulsively with the high pressure behind the passing shock.

To this end a shock tube based test rig was designed and built. It consisted of a vertically mounted shock tube with driver section at its lower end and transparent water tank at its top end. At the end of the shock tube and base of the water tank geometrically shaped plates were flexibly mounted with their concave surfaces facing upwards. As the shock wave travels up the shock tube, it strikes the deflector plate at

its end forcing it to accelerate rapidly towards the free water surface above. Water surface effects as shown in figure 1.15 result.

The shock tube, water tank and curved "deflector" plate configurations are shown below.

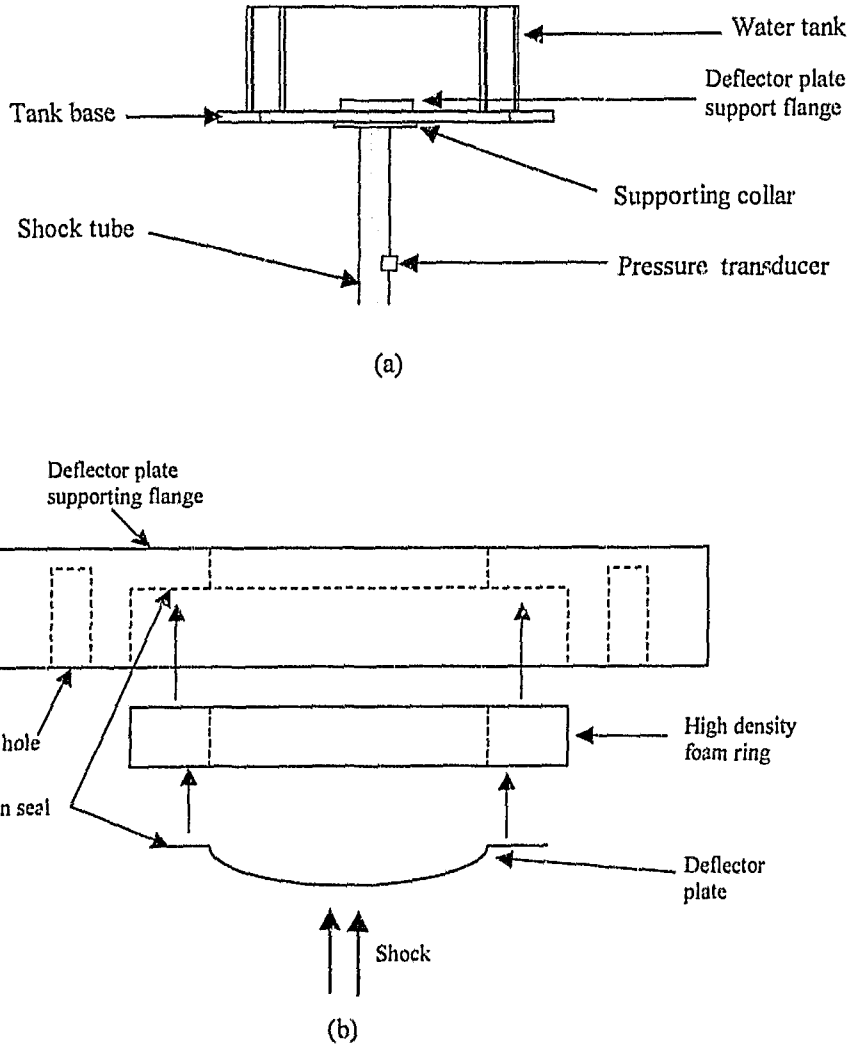

Figure 1.16 (a) Shock tube and water tank configuration
(b) Exploded view of deflector plate and supporting flange

The current research further explores the liquid shock waves and free surface water jets produced. Pressure measurements are used to characterise and understand the observable physical phenomena. Different deflector plate configurations are explored. Finally non-linear dynamic analysis software is used to simulate the water jet production process.

2. Literature Review

Mortimer studied liquid wave focusing and the production of free surface liquid jets using focused underwater shock waves (Mortimer 1997). The aim of this research was to explore the state-of-the-art of liquid shock wave experimentation and the application of liquid shock waves to new areas. One new area is the production of pulsed liquid surface jets using focused shock waves. These pulsed liquid jets have potential applications in material sorting and rock breaking.

In material sorting, particles reach the end of a conveyor belt or similar system and are allowed to fall freely through an inspection region. While undergoing projectile motion, desired particles can be deflected from the rest using a water jet. Water jets are preferable to air/gas jets because they diffuse less rapidly. Thus they maintain a higher momentum flux over larger distances. They also provide better momentum transfer on collision with the target particle (Mortimer et al. 1995). In rock breaking applications, water jets are used for the high "water hammer" pressures developed during the initial stages of jet impact. When a high velocity liquid slug strikes a solid surface, a reflected shock wave develops in the slug and travels backwards along its length at close to the speed of sound in the liquid. Initially very high pressures develop in the contact zone. These, coupled with cavitation effects resulting from the reflection process, can produce significant surface damage (Lesser et al. 1983). The high impact pressure only lasts until the expansion waves from the edge of the jet column reach the reflected shock wave (Mortimer 1997).

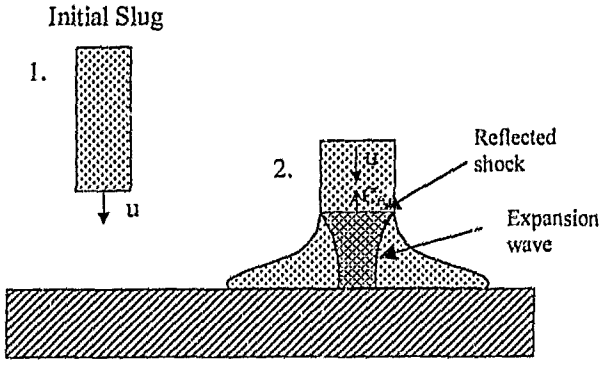

Figure 2.1 Schematic of liquid slug impacting a solid surface (Mortimer 1997)

Focused underwater shock waves can be used to produce the water jets required by the abovementioned applications. The process of focusing shock waves in air was first explored by Sturtevant and Kulkarney (Sturtevant et al. 1976). They found that weak shock waves curved concave towards the direction of propagation, converge and tend to focus.

For a shock wave at a perfect geometrical focus, different focusing configurations are possible depending on the shock strength (Sturtevant et al. 1976). The following figure summarises these possibilities.

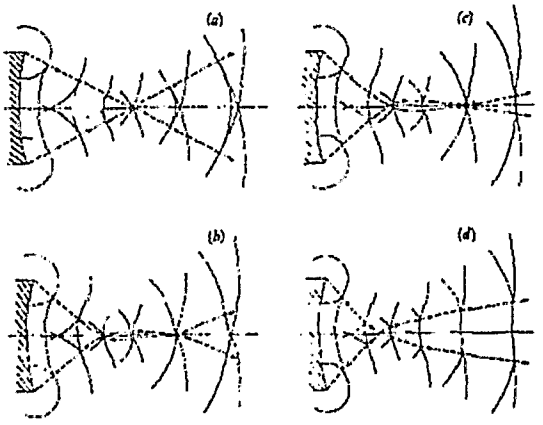

Figure 2.2 Different possible configurations for focusing shock waves
(a) sound pulses (b) weak shocks (c) moderately strong shocks
(d) strong shocks (Sturtevant et al 1976)

For very weak shocks (figure 2.2(a)), which can be considered acoustic shocks, the focusing process is described by the geometrical acoustics of Keller(1954). The front propagates normal to itself with a fixed speed at all times. In an isentropic atmosphere, the trajectories of points on the shock (rays) are straight lines normal to the shock front and cross as shown below. The surface on which adjacent rays cross is called a caustic surface.

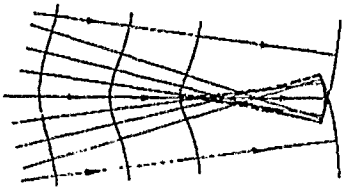

Figure 2.3 Focusing of weak shocks according to geometrical acoustics (Sturtevant et al. 1976)

For weak shocks as shown in figure 2.2(b), the wave pattern initially has three distinguishable components. The circular wavefront in the centre, concave to the right, is the reflected shock travelling towards the focus. Extending from this wavefront on either side are diffracted shocks emanating from the sharp corners of the

parabolic reflector. These expansion waves meet each other before the shock front reaches the focus. This gives the shock front a crossed and folded configuration. Thereafter the diffracted shocks precede the focused shock, which follows between the folds.

Figure 2.2(c) shows the borderline case of a moderately strong shock. In this case, the shocks come very close to a second crossing, but then move away. The focal spot is almost pinched off at that point, but not quite, so the waves leaving the focus are not crossed. For shocks weaker than this the shock fronts cross twice, giving a finite focal spot and crossed shock fronts. The stronger the shock, the larger the focal spot and the smaller the triangular loop in the shock fronts. For still stronger shocks figure 2.2(d), the focal spot becomes semi-finite and the loop disappears. In the focal spot, the shock wave is plane and normal, and the pressure amplitude is finite. Thus strong shocks conform to the theory of shock dynamics. Here rays are considered to travel orthogonal to the shock fronts, however the shock front can travel at different speeds along different rays depending on its amplitude. This effect turns the shock front and bends the rays. The concave portion of the shock amplifies and accelerates relative to the not-so-concave portions. The rays then curve away from the focus and the shock front becomes "smooth" as illustrated in the figure below. The rays do not cross and the pressure amplitudes are finite. The shock emerges flattened and it has no loops.

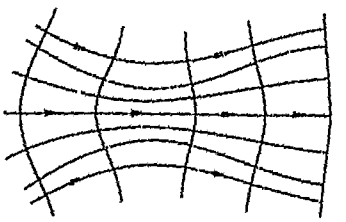

Figure 2.4 Focusing of a weak shock according to shock dynamics (Sturtevant et al. 1976)

The trajectories of the three wave intersections divide the flow into regions that can be identified by the kinds of waves occurring in them. Each of the regions exhibits a characteristic pressure history.

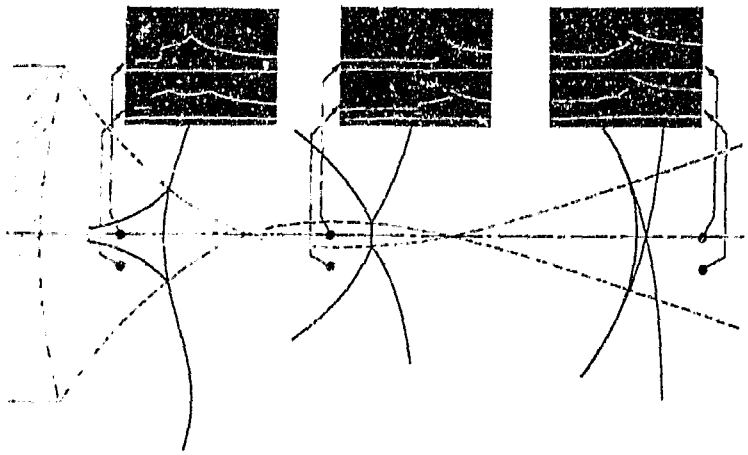

Figure 2.5 Characteristic pressure histories of the three wave intersections (Sturtevant et al. 1976)

In the above figure, shocks are seen as discontinuities of pressure, whereas diffracted waves appear as discontinuities of slope. Even though only the weak shock case is shown, the pressure traces remain qualitatively the same in all cases, though for strong shocks the focal region extends to infinity, so crossed shock fronts and the corresponding pressure traces do not appear. From figure 2.5 it can also be seen that the first crossing of the trajectories of the three wave intersections is the point of maximum amplitude. This amplitude is severely attenuated at later instants by the two overtaking diffracted expansions (Sturtevant et al. 1976).

Sturtevant and Kulkarny (1976) found that non-linear gasdynamic effects limit the pressure amplitude achievable at the focus of a shock wave. There are two predominant non-linear effects. Firstly the steepening of the diffracted field behind the converging shock front, which leads to a diffracted shock. Secondly the diffracted shock can form either a reflected shock or the Mach stem of a Mach reflection.

More specifically there is a transition Mach number which separates these last two cases. When shock convergence is achieved by reflection from an elliptical reflector, depending on the diameter to focal length ratio (D/f) of the reflector, the transition Mach number is found to lie between 1.05 and 1.10 (Grönig 1985). For Mach numbers below this transition value, when the centre part of the focusing shock wave reaches the focal region it steepens up and accelerates. This causes a Mach stem which prevents further focusing. The Mach stem shrinks beyond the focus and the wave leaves the focal region crossed and folded as predicted by geometrical acoustics. Thus if the plane of symmetry is considered as an ideal reflecting wall, then the whole process corresponds to a transition from Mach to regular reflection.

For Mach numbers above the transition value, no wave crossing is observed beyond the focus, but the Mach stem length is continuously increasing. The geometry

corresponds more to Whitham's shock dynamics (Whitham 1958); However, contrary to predictions, the Mach stem is not bent convex.

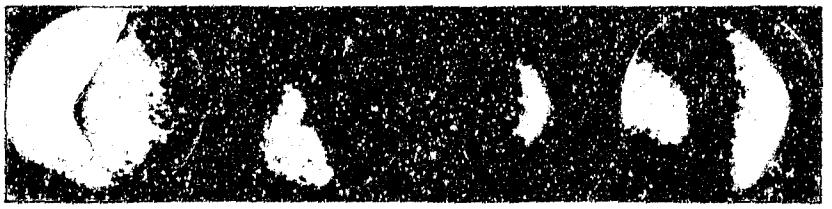

(a)

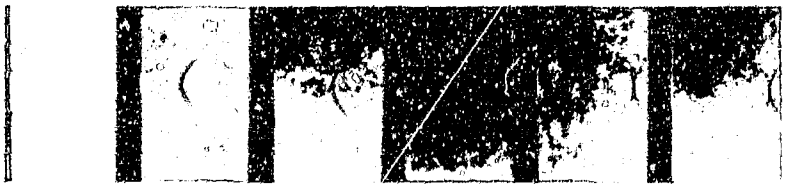

(b)

Figure 2.6 Wave focusing in air (a) M=1.0068 (b) M=1.072 (Grönig 1985)

The gasdynamic focus, defined as the axial position where maximum pressure occurs, is inside the geometrical focal length (Sturtevant et al. 1976, Nishida et al. 1987).

In air, the pressure amplification achieved by a converging shock wave is of the same order of magnitude as the original pressure pulse (e.g. Sturtevant et al. (1976) amplification = 5 for shock Mach number = 1.1). In water, because in the gasdynamic sense shock waves up to a few hundred bar can be regarded as rather weak, during the focusing process very high pressure intensifications can occur. This means that the focusing of such a wave obeys rules very close to the theory of geometrical acoustics.

Müller (Müller 1987, 1989) investigated the focusing of weak spherical shock waves in water using both shallow and deep ellipsoidal reflectors. In the case of shallow reflectors, which utilise only 5% of the primary shock energy, focusing occurs close to the geometrical focus and high pressure amplifications result. For deep reflectors, which utilise over 50% of the primary shock energy, increased non-linear effects lead to wider focal areas and lower focal amplitudes. The maximum pressure amplification of about 100 recorded at the focus in Müller's experiments, compared to the incident shock wave at the reflector surface, was achieved using a shallow reflector. This corresponded to a pressure of 1300Bar at the focal point. For shallow reflectors, since the focusing shock waves are very weak, the reflection and focusing evolve according to the laws of geometrical acoustics with a small focal spot of only a few millimetres. Diffraction effects are also minimal because the incident angles of the front normals are low and the initial shock is not diffracted in such a way that it disturbs the converging shock front. Müller used a shadowgraph system to visualise the

focusing process. Pressure histories were measured at different positions in the converging field.

The analysis of converging fields in liquids is complicated by their high propagation velocity and short pulse length of only a few microseconds. Since commercial pressure probes are not capable of meeting such requirements, Müller and Platte custom designed and built a micro pressure gauge based on an ordinary needle (Platte 1985). The needle was coated with a thin layer of polyvinylidene fluoride (pvdf), polarised at the top by a corona discharge after solidification. The body of the needle forms one contact itself and the other is a thin layer of silver conductive paint and a metal tube.

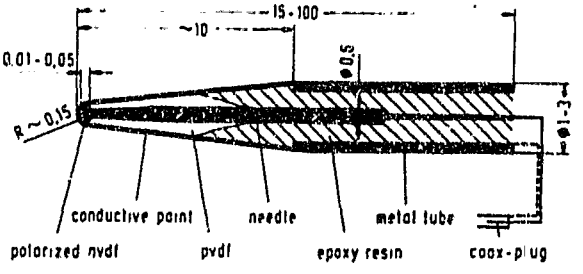

Figure 2.7 Needle hydrophone custom designed and built for analysis of shock waves propagating through liquid media (Müller 1987)

In Müller's experiments, the elliptical reflectors used were positioned opposite to the shock wave source such that the centre of the shock wave produced coincided with the one focus of the reflector. The following figure shows a schematic cross section of this arrangement. That part of the hemispherical shock wave, inside the angle α, which strikes the reflector surface, propagates towards the second focus (F_2) after reflection.

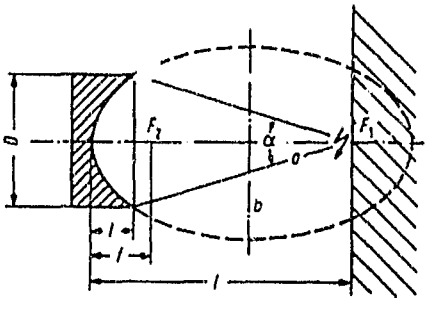

Figure 2.8 Schematic of shock wave focusing by reflection from an ellipsoidal surface (Müller 1987)

The following figure shows a set of experimental results obtained.

Figure 2.9 Shadowgraph of the focusing process (Müller 1987)

The incident shock wave has passed from right to left. On the extreme left of every frame is the silhouette of the reflector edge. The reflected shock can be seen moving towards the focus. Diffracted waves from the reflector edge can also be seen. The focus is reached in the fourth frame. After the focus, the shock front diverges again. Later the diffracted shock crosses in front of the reflected shock and cavitation bubbles appear in the focal region. The focal position shown in the fourth frame coincides with the geometrical focus of the shallow ellipsoidal reflector used in the experiment.

The following figure shows the pressure history of the focusing process shown above. The reflected shock is shown by solid lines and the diffracted shock by dashed lines.

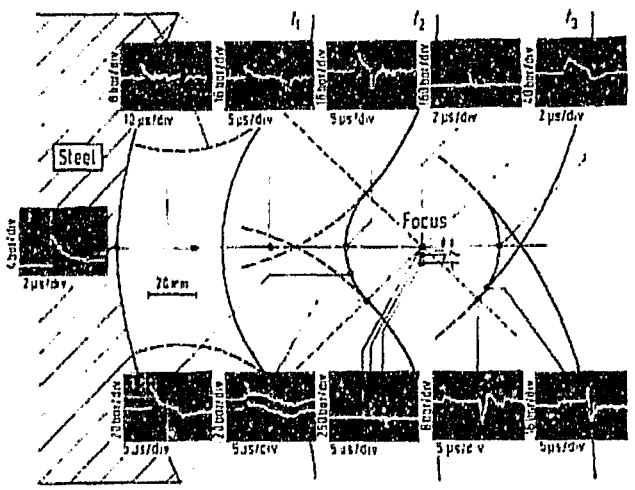

Figure 2.10 Pressure distribution in the focusing field of an elliptical reflector (Müller 1987)

The left oscillogram in the middle shows the pressure profile of the incident shock wave without a reflector. The upper profiles show the pressure history on the reflector axis, while the lower profiles show the pressure distribution at a distance from the

reflector axis. Considerable amplification at the focal spot can be seen. The negative peak which follows the focusing shock wave is caused by the diffracted expansion wave from the reflector's edge. The middle lower profile shows the pressure amplitude at the focal spot and at distances of 1mm and 2mm away. At 1mm from the focal spot there is 60% and at 2mm only 35% of the pressure amplitude at the focal spot remaining. This shows that the focal area is very small.

The figure below shows the pressure distribution in the diverging part of the wave field behind the focus, as well as the crossing over of the diffracted waves.

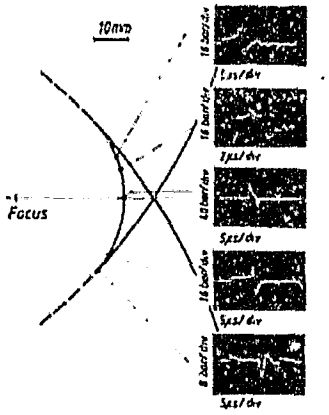

Figure 2.11 Pressure distribution in the diverging front behind the focus (Müller 1987)

Throughout the focusing process the pressure distribution conforms to the predictions of acoustic theory except in the focal region. The dimensions of the focal region are very small and the pressure drops sharply perpendicular to the reflector axis.

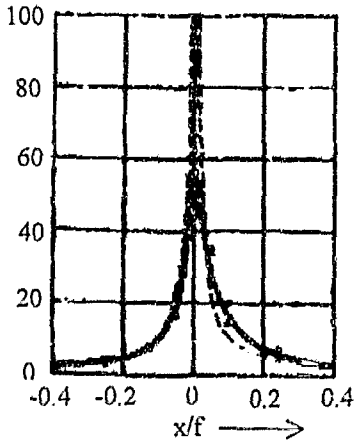

Figure 2.12 Pressure distribution on axis of symmetry (x) versus distance from focus (Müller 1987)

Müller found that the maximum peak pressures are achieved by reflectors with greater D/f (Diameter/focal length) ratio i.e. decreasing focal length. The reason for this effect is small non-linearities occurring during the focusing process which have more influence when the reflected shock must travel a greater distance to the focal point. These non-linearities cause the focal region to grow and the energy density to decrease. The results obtained are shown below.

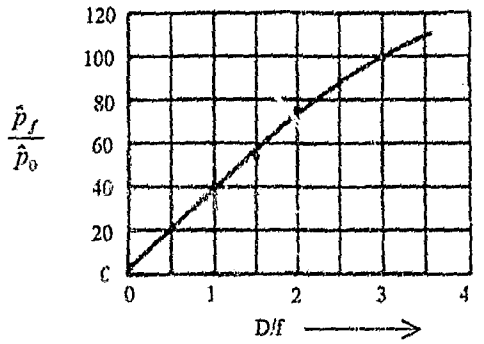

Figure 2.13 Pressure amplification at focus versus D/f (Müller 1987)

Although shallow reflectors generate higher pressure amplitudes at the focus, the higher energy content at the focus of a deep reflector causes better disintegration of materials/solids placed in the focal area (Müller 1989). Therefore the ellipsoidal reflectors used in lithotripsy and other medical applications are usually deep with large aperture sizes to minimise the energy density in the shock wave field outside of the focal area. This helps to avoid tissue damage while still concentrating enough energy at the focus to fracture kidney or gallstones.

Takayama et al. (1983) also carried out experiments on the production and focusing of underwater shock waves. Spherical shock waves were produced by radiating a submerged lead azide pellet with a Q-switched ruby laser beam. Both spherical and ellipsoidal reflectors were used to focus the shock front. In the case of the spherical reflector, detonating products from the underwater explosion prevent the reflected shock wave from focusing at the geometrical focal point of the reflector. Using ellipsoidal reflectors the reflected shock does focus, but this focal spot is a few millimetres away from the reflector's geometrical focus. The authors attribute this difference to non-linear effects.

Mortimer(1997) extended the focusing of shock waves to include the production of pulsed water jets. Through the use of both an EMAS and an FEMAS, electrical discharges were used to produce a shock wave in a fluid filled cavity. These shock waves were then focused onto a free water/air surface, causing a pulsed water jet. This is called the shock-reflection method because the water jet is caused by the reflection of a high amplitude shock wave from the water/air interface.

Results of the interaction of a shock pulse from both an EMAS and an FEMAS with the free water/air interface were recorded using a high speed digital camera. For the EMAS, tearing of the liquid surface was initially observed. The results initially show "streaks" which represent water particles torn from the water surface by the reflected shock wave. Gross water surface deformation evolved at later times. Mortimer approximates the streak velocity at 4m/s, and the surface deformation velocity at 0.4m/s. The surface deformation evolves into an unstable "cumulative" jet as shown below.

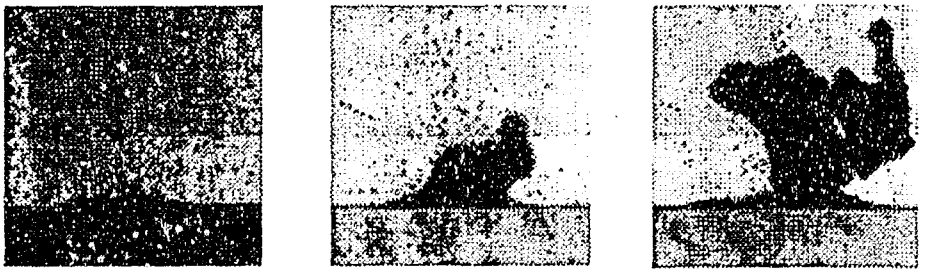

Figure 2.14 Experimental results showing initial streaking and evolution of surface deformation for an EMAS (Mortimer 1997)

Mortimer attributes the initial streaking to the reflection of the incident shock pulse from the water surface, while the surface deformation is attributed to the overall hydrodynamic flow caused by the physical motion of the EMAS disk. The results obtained were shown to depend on the water level above the EMAS. When this water level was changed, the recorded results showed corresponding changes. Figure 2.15 shows the initial streaking of the water surface for a lower water level than that of figure 2.14.

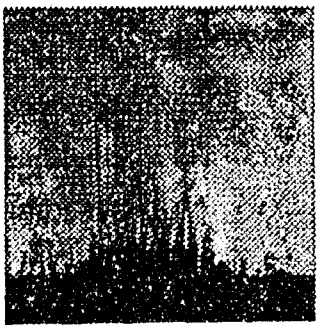

Figure 2.15 Experimental result showing initial streaking for lower water level (Mortimer 1997)

The higher wave pressures (since the liquid surface is now closer to the disk surface) cause more "streaking". The high speed water droplets are moving at approximately 5m/s and the slower cumulative jet at approximately 0.7m/s. This may reflect the

higher pressures resulting at the water/air interface when the shock wave is reflected from a lower water surface.

Interaction of the shock pulse produced by an FEMAS with the water/air interface is similar to that for the EMAS. First there is the initial tearing of the liquid surface followed by a slower cumulative jet. For the FEMAS, the initial streaks are more localised while the surface deformation evolves more rapidly and is more stable than that of the EMAS. The streaks travel at approximately 6m/s and the surface deformation at approximately 3m/s.

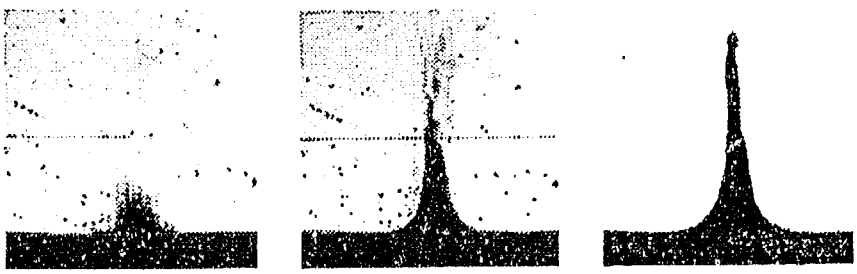

Figure 2.16 Experimental results showing initial streaking and evolution of surface deformation for FEMAS (Mortimer 1997)

Cavitation effects are noted below the water surface as a result of the focusing process.

In order to increase the pressure pulse at the free water surface, Mortimer used a converging nozzle together with the EMAS unit (Mortimer 1997). This arrangement and the result obtained are shown below.

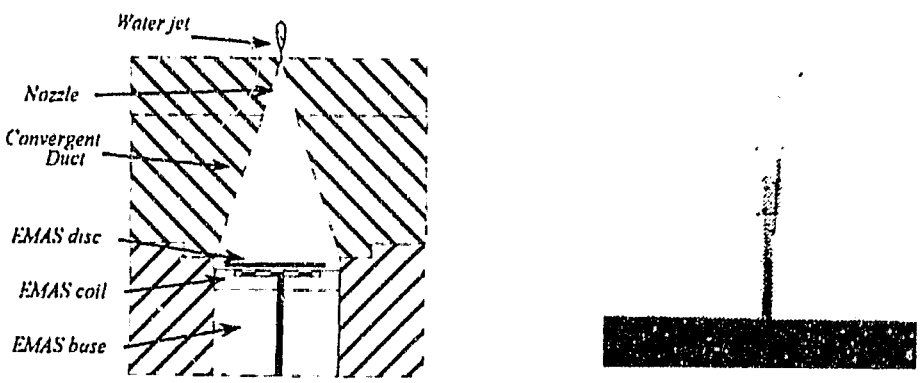

Figure 2.17 Experimental setup and result using an EMAS and converging nozzle (Mortimer 1997)

Approximate jet velocity using the converging nozzle is considerably higher than that of jets produced by the EMAS/FEMAS alone. Mortimer was unable to determine the velocity accurately, due to limitations of the experimental equipment used, but approximates it at between 40m/s and 100m/s (depending on the EMAS/FEMAS discharge voltage used). A n anomaly which resulted when using the converging nozzle was the presence of a secondary pulsation which Mortimer hypothesises is due to internal reflections within the nozzle and or an unstable jet.

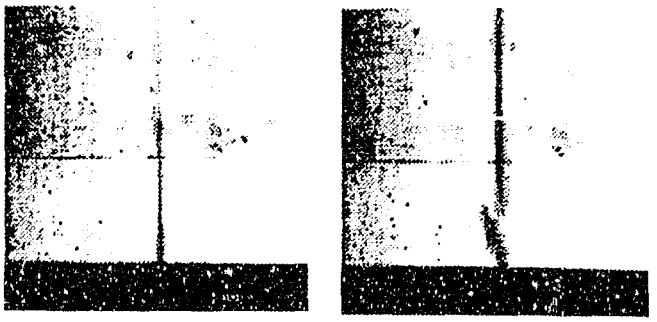

Figure 2.18 Initial jet and secondary pulsation using EMAS ar d converging nozzle (Mortimer 1997)

The study of actual water jet phenomena at a water/air interface is well established (Kedrinskii 1978); However the earliest studies have focused on the water jets produced at the water/air interface by detonation of an underwater explosive charge. Despite this difference, many of the observations stemming from these experiments can be generalised to water jets produced by other hydrodynamic shock wave sources.

Kedrinskii (Kedrinskii 1978) recorded the production of four distinct jet/plume types as a result of an underwater explosion. The jet shape which occurs is mainly dependent on the underwater depth of the explosive charge. The four water jet types and their mechanisms of formation are shown below.

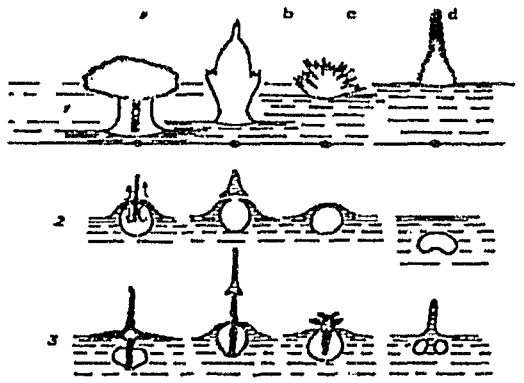

Figure 2.19 Water jet profiles resulting from underwater explosions at different depths (Kedrinskii 1978)

For low explosion depths (figure 2.19(a)), a flat cylindrical plume develops at the centre of which there grows a thin and narrow column of water. As the explosion depth increases, the flat cylindrical plume remains, but from its centre a cupola appears from which in turn grows a thin and narrow secondary jet (figure 2.19(b)). This secondary jet is wider than before. With further increases in explosion depth, the secondary jet's rise time increases to the point where the cupola attains its maximum height before the narrow secondary jet appears above it. Since the water jets under consideration are produced by underwater explosions, interaction of the gas cavity carrying the detonation products from the explosion with the surface effects produced at the water/air interface by the passing shock becomes apparent in tests requiring longer development/rise times. Thus in figure 2.19(c), as explosion depth increases to a critical level, the surface effects caused by the shock wave just begin to develop before the cavity with the detonation products reaches the surface, tearing the surface effects into a feather shape. For explosion depths greater than this critical level (figure 2.19(d)), the detonation products reach the surface soon after the shock wave itself, with a high buoyancy velocity. The water between the rising cavity and the free surface is ejected vertically upward, forming a high narrow fountain.

It is interesting to note that the shapes of water jets described by Kedrinskii resemble closely those recorded by Mortimer (1997) and Karnovsky (1998), the latter using non-explosive experimental techniques. Mortimer has photographed jets which resemble figure 2.19(2a), but without the expanded base caused by the rising detonation products. Karnovsky has photographed and recorded the stages of development of jets which resemble the shapes shown in figure 2.19(1a,b,d). One test also closely resembled the jet shape shown in figure 2.19(2a), i.e. a wide base of water with a thin vertical stream issuing from its centre. This result was not repeatable however.

Based on the experimental results obtained, Kedrinskii (Kedrinskii 1978) was able to characterise the principle characteristics of the jet flows discussed above. These are presented here because of the similarity between the jets recorded by Kedrinskii and those recorded by Mortimer and Karnovsky.

$$H_* = 60Q^{1/4}$$

$$T_* = 2.25Q^{1/8}$$

$$V = 29Q^{0.55}h^{-1.66}$$

$$M_* = 300Q$$

Where: H_* = Maximum height of ascent (m)
Q = Explosive charge weight (kg)
T_* = Time of ascent (s)
M_* = Amount of liquid in jet (kg)
V = Maximum jet velocity (m/s)
h = Explosion depth (m)

Just as these equations characterise the water jets produced in terms of the mass of explosives used, so it may be possible to characterise those produced by non-explosive techniques according to a fundamental variable such as shock strength.

Further experimentation by Kedrinskii proved that similar free surface water jets could be produced by accelerating a solid sphere or cylinder initially immersed in the liquid towards the free surface (Kedrinskii 1978). Before reaching the surface, the sphere is slowed down to simulate the development of the explosion cavity.

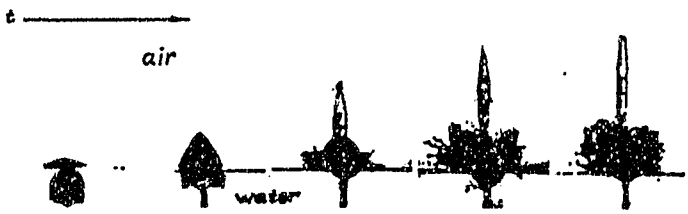

Figure 2.20 Water jet produced by accelerating a solid sphere initially immersed in liquid towards the free surface (Kedrinskii 1978)

Based on the experimental results obtained, Kedrinskii was able to describe the jet formation process occurring in all instances using the following model. When a shock wave from whatever source interacts with a free water surface, spalling occurs and a recess is formed at the water surface. The expanding detonation products cavity creates a velocity field orthogonal to the surface of the recess. Inflow of this recess leads to the formation of a cumulation jet. Thus a directional vertical jet develops on the initially plane surface.

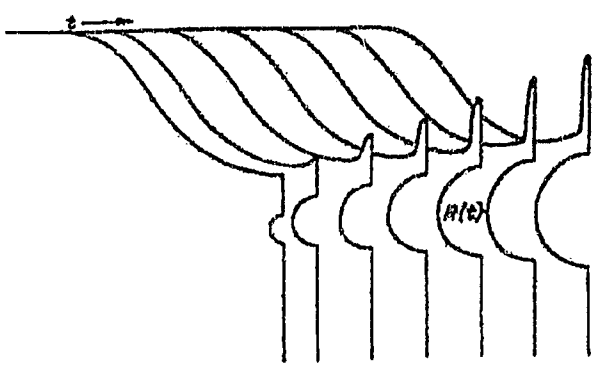

Figure 2.21 Development of a water jet at a surface recess (Kedrinskii 1978)

For the water jets caused by detonation of an explosive charge very close to the free water surface, the basis of the jet structure is a jet tandem. The first jet is formed as a result of the inertial motion of the layer of liquid above the explosion cavity, and the second as a result of closure of the open pocket formed after depressurisation of the explosion cavity. (This process is similar to the spalling model above). Furthermore,

the development of the second jet is the same as the flow originating as a result of the surface closure of the water pocket caused by the high velocity penetration of a bullet into a liquid (Kedrinskii 1978)

A similar explanation for water jet formation was documented by Zeff et al (1999, 2000). Here the authors report a theoretical and experimental study of the generation of a singularity by inertial focusing in which no break up of the fluid surface occurs. The singularity forms on a water surface undergoing vertical excitation of the form $a = a_0 \sin(\omega t)$ in which the acceleration amplitude a_0 is near a critical a_c. To create the event a glycerine-water mixture with viscosity 2.0cm^2 s is oscillated in a periodic wave state. Should the acceleration amplitude suddenly be increased to above a_c the collapsing minimum entrains an air bubble below the fluid surface. The resulting inertial collapse focuses the kinetic energy of the moving fluid along a central axis and produces a narrow, high-speed vertical jet as shown below.

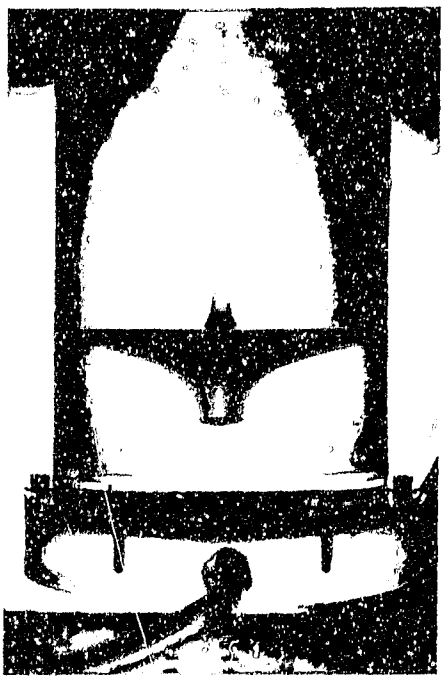

Figure 2.22 Water jet produced by collapse of a surface wave minimum (Zeff et al. (2000))

Velocities near the tip of the jet can exceed 50m/s whereas typical velocities in the pre-jet waves are in the order of 3cm/s. Rayleigh instability in the jet causes the formation of a droplet at its tip and eventually causes the jet to break into droplets.

3. Equipment

The shock tube used had been designed and built by the author in 1998 (Karnovsky 1998). It consists of a vertically mounted round shock tube, leading into a square water tank. The shock tube is divided into a high pressure driver chamber and low pressure expansion chamber separated by a diaphragm station. Plastic diaphragms of 50micron polyurethane were used. The diaphragm station is secured with eight retaining bolts. The maximum driver pressure available is 6Bar. A hole in the wall of the shock tube, through which the diaphragm is ruptured, also serves as a vent during testing allowing the high pressure in the shock tube to normalise to atmospheric levels. The water tank at the end of the shock tube has 600*600*200mm inner dimensions. A deflector plate assembly separates the air in the shock tube expansion chamber from the water in the water tank.

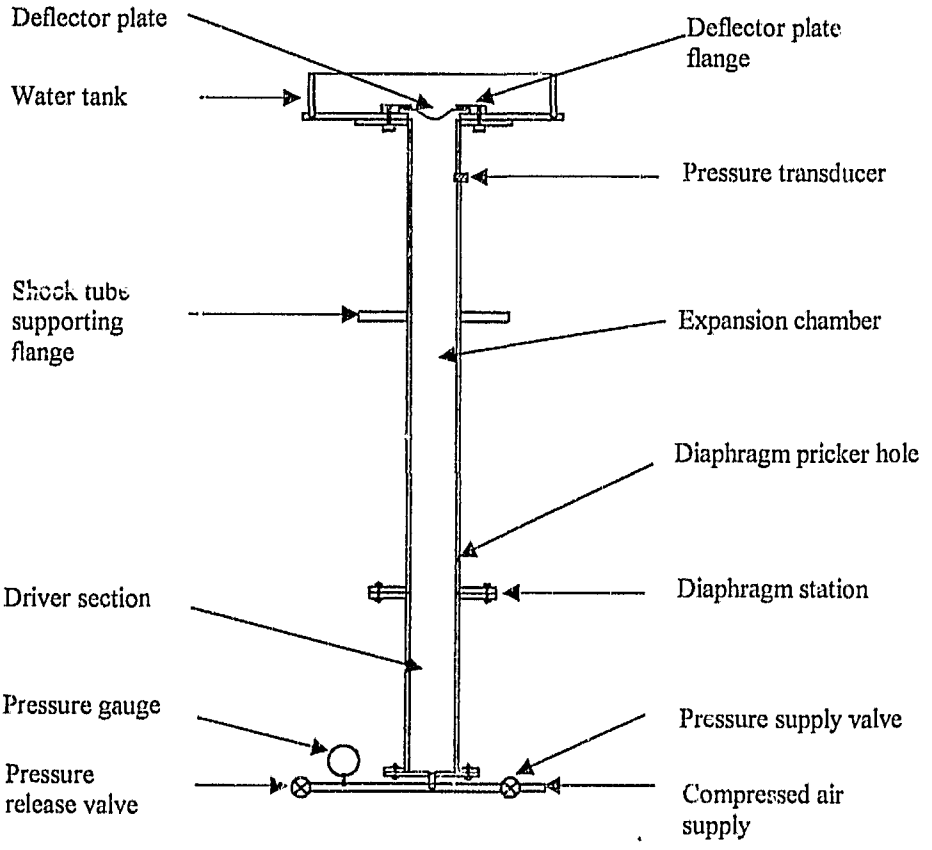

Figure 3.1 Schematic view of the shock tube used

3.1 Deflector plate assembly

The deflector plate assembly consisted of a flexibly mounted 0.5mm thick copper deflector plate supported and attached to the shock tube with a mild steel flange. The deflector plate itself was formed in a custom designed die (Karnovsky 1998) to a parabolic profile with 50mm focal length and 10mm flat supporting ring on its outside. Initial copper disk blank diameter was 75mm. Final pressed diameter was 73mm.

Flexibility resulted from mounting the copper deflector plate against a 10mm thick high density foam ring. The foam was sourced from Sondor Industries Ltd. It is a closed-cell, cross-linked ethylene vinyl acetate foam of density 45kg/m^3.

Commercially available silicon sealant was used to attach the deflector plate to the foam ring and the foam ring to the supporting flange. Silicon has the advantage of providing a tough but flexible waterproof seal. One disadvantage is its long curing time – minimum twenty four hours.

A schematic diagram of the deflector plate assembly is shown below.

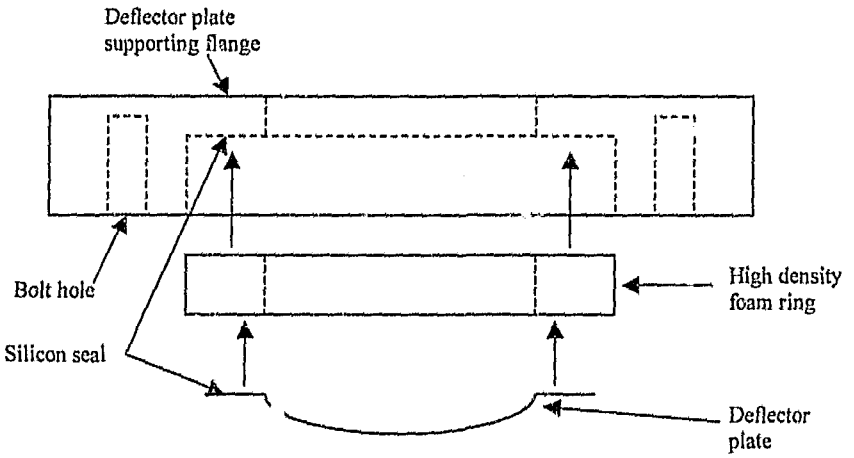

Figure 3.2 Schematic view of deflector plate assembly

Using the above deflector plate assembly, some successful test results were obtained, but the majority of results were not useful. This situation was exacerbated by frequently having to change the deflector plate assembly when leakage occurred. This leakage of water from the water tank into the shock tube occurred when a silicon seal on the deflector plate assembly had been compromised. To correct the situation required rebuilding the entire assembly. Apart from being disruptive to the test schedule, rebuilding the deflector plate assembly did not allow continuity of results. This is because the new assembly, being hand built, would not match exactly the previous one. Furthermore, each assembly's stiffness would decrease as testing progressed, yielding better water jets and more defined pressure peaks recorded by the

oscilloscope. Thus the results obtained using a newly replaced deflector plate assembly would not necessarily match those obtained with the previous assembly.

To avoid this required redesign of the test equipment. Such redesign was not intended to compromise the basic philosophy underlying this research - of a flexibly mounted deflector plate struck from below by a shock wave and producing a water jet above. For this reason only a new deflector plate assembly design was sought which would eliminate those aspects of the current design which disrupted the testing procedure.

Professor Skews suggested using a bellow to provide the flexible mounting to which the deflector plate could be attached. The advantage of this is that the use of one bellow for all tests would provide a single set of mechanical properties leading to consistent test results.

The feasibility of such a system was explored in conjunction with a local industrial bellow manufacturer – Bellow Weld (Pty) Ltd. This company designs and manufactures bellows to all manner of specifications. Its representatives were confident that it was possible to produce a bellow unit which would attach to the shock tube end flange and water tank without requiring major reworking to either. Also, the bellow would be able to withstand high pressures without deforming yet still not be so stiff that it did not allow deflector plate movement. Another important requirement was that the deflector plate at the end of the bellow should be held straight in position so as not to produce a lopsided water jet. The following figure shows the delivered product.

(a) (b)

Figure 3.2 (a) Deflector plate mounted on a stainless steel bellow and support flange
(b) Support flange incorporating o-ring seals

The middle bellow section was designed and built by Bellow Weld, while the bottom flange, o-rings and deflector plate were designed by the author and machined at the School of Mechanical Engineering Workshop. Bellow Weld welded the flange and deflector plate to the bellow. The bottom flange was designed to allow convenient attachment to the shock tube end flange and water tank. Its o-ring seals were designed to withstand a pressure of 15Bar in the shock tube. Dial pins were incorporated for better alignment with the water tank base. The deflector plates as well as the deflector

plates used, was pressed in a die custom designed by the author (Karnovsky 1998). The material used was 0.5mm stainless steel plate. It was welded ("hydroscaled") to a lip on the end of the bellow.

Preliminary tests immediately exposed a design flaw in the bellow. The high pressure region behind even low strength shock waves (1Bar driver pressure) was enough to cause considerable permanent elongation of the bellow assembly. Higher shock wave strengths had consistently been used in previous tests.

To overcome this a displacement limiting mechanism was designed. A cross section and the finished product are shown below. The displacement limiter not only limits the extension of the bellow, but also provides a wide surface, level with the deflector plate in its relaxed state and encases the bellow convolutions. These features minimise unwanted hydrodynamic effects caused by flow around the bellow convolutions when a test is run.

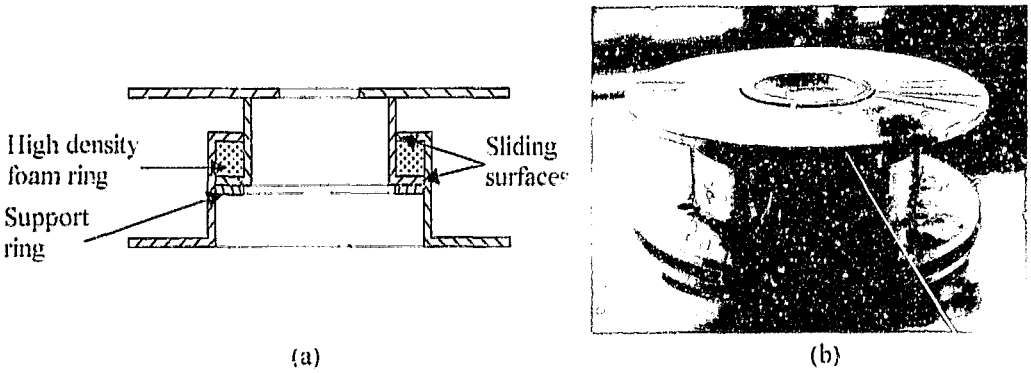

Figure 3.4 (a) Schematic section of bellow displacement limiter
(b) Picture of displacement limiter

The displacement limiter incorporates a ring of high density foam as shown in figure 3.4. Preliminary tests showed that with the displacement limiter fitted there was too much resistance for the bellow system to produce even appreciable water surface deformation. To allow the system to move more freely, the foam ring was removed completely, but the displacement limiter was otherwise left unchanged. Better results were obtained.

3.2 Data acquisition system

A pressure transducer (PCB Electronics model 113A21) was fitted to the expansion chamber of the shock tube, 150mm from its end, using a precision machined saddle brazed into the shock tube wall. Further data on this transducer and its calibration curve can be found in Appendix A2. Output from the transducer was coupled to an ICP line power unit (PCB Piezoelectrics, model 482A10 serial number 665) via microdot coaxial cable. The signal output from this unit was fed directly into a high

speed digital oscilloscope (Yokogawa DL1200A – serial number 21XF5181) with a printer function incorporated.

3.3 Needle hydrophone

A needle hydrophone was used to measure pressure at different points in the water tank. This consists of a metal needle, rounded at its tip, coated with a layer of polyvinylidene fluoride (pvdf). The metal needle both supports the pvdf layer and acts as one of its electrodes. The other electrode, which also acts as an electrical shield, is a conductive layer on the outside of the pvdf produced by application of a conductive paint. The whole arrangement is mounted onto the end of a thin metal pipe, which is connected to a coaxial cable at its other end. To insulate the wire inside the metal pipe, it is filled with a non-conductive epoxy resin (Platte 1985).

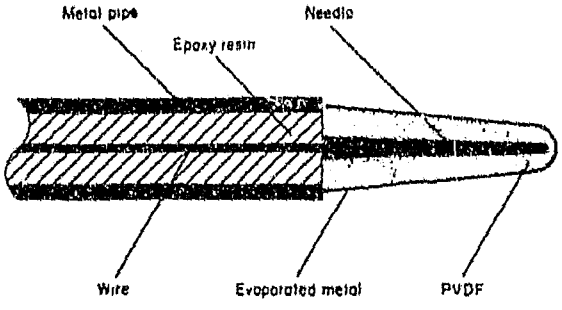

Figure 3.5 Cross sectional view of the needle hydrophone (Platte 1985)

The needle hydrophone is designed for high energy ultrasound measurements as well as for recording blast waves in water. It has a very small sensitive diameter of less than 0.5mm and a very short rise time of approximately 50ns. More information on the unit used and its technical specifications can be found in Appendix A3.

3.4 Needle hydrophone positioning system

Pressure measurements are required at discrete points in the water tank. In order to provide accurate positioning of the needle hydrophone in three dimensions it was necessary to custom design and build a needle hydrophone positioning system. Two such systems were built. The first was a computer controlled, stepper motor driven system and the second a manual positioning system.

3.4.1 Stepper motor positioning system

This system used four stepper motors (North American Philips Controls Corporation type A82709-M2 , RE28075), salvaged from old computers, controlled using the parallel port of a pc to position the needle hydrophone in three dimensions. The unit

incorporated toothed belt and pulley drives, precision shafting and linear bearings for accuracy.

Preliminary tests showed that the unit was only accurate to within 5mm of any desired position in the X or Y directions. This inaccuracy was traced to the stepper motors, the coils of which must be energised with very precise timing to achieve accurate positioning. Further work was done to improve positioning accuracy, but it was found that improved timing could only be achieved using a custom designed stepper motor controller card fitted to the pc. These are expensive and require new stepper motors to be bought as well. It was decided to redesign the positioning system not to include the stepper motors.

3.4.2 Manual needle hydrophone positioning system

The manual needle hydrophone positioning system design was intended to retain as much as possible from the stepper motor positioning system yet provide the required positioning accuracy. A picture of the unit is shown below.

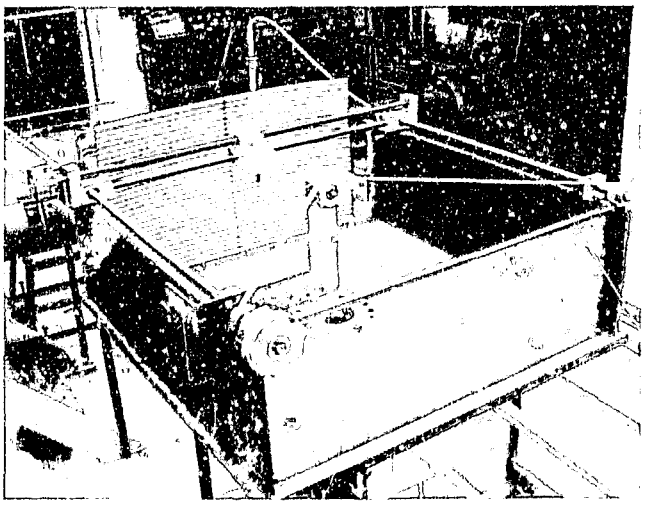

Figure 3.6 Manual positioning system

The belt drives and shafting of the original system were replaced by screw threads which were manually turned to position the needle hydrophone as required. To avoid any twisting in the system, the two screw drives along the length of the water tank were connected with a toothed belt and pulley system. The unit provided accuracy measurable to within 0.5mm of any required needle hydrophone position.

4. Results Using Foam Ring Deflector Plate Assembly

Over the period 25 October to 20 December 1999, tests were conducted aimed at complementing the test results already presented by the author (Karnovsky 1998). These original results show the water surface effects which result from impulsively loading a flexibly mounted curved deflector plate below a free water surface. The current set of tests were intended to explore the pressure fields below the water surface which drive the water surface effects recorded. A full description of the experimental equipment can be found in Chapter 3.

The manual 3-D needle hydrophone positioning system allowed repeatable positioning of the needle hydrophone at any point in the water tank. The main test results were pressure traces captured by the oscilloscope. These were recorded both on hardcopy and electronically – using a pc interface program written for the University of the Witwatersrand by N. Harbor.

A typical test result, including the oscilloscope settings for each channel in use, is shown below. Channel 1 is directly connected to the needle hydrophone. Channel 2 is connected via amplifier to the pressure transducer mounted in the wall of the shock tube, 150mm below the water tank base.

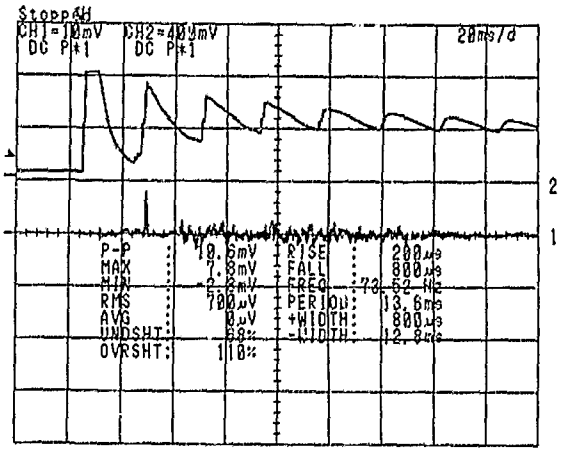

Figure 4.1 Typical test result

The oscilloscope's data analysis functions were used to facilitate real time interpretation of the pressure trace output by the needle hydrophone in each test. This included maximum and minimum voltages. The times at which these occurred can be measured off the actual signal trace.

During initial testing, sensitivity of the coaxial cable connecting the needle hydrophone to the oscilloscope was noted. Bumping the cable induced a voltage signal which was clearly recorded by the oscilloscope. To minimise this effect, the coaxial cable was encased in snug fitting silicon tubing and raised to avoid contact with any solid surfaces.

The walls of the shock tube used were designed to withstand a 15Bar internal pressure. Most tests however were performed in the range of driver pressures from 3-5Bar. These pressures yielded adequate results in terms of the shock wave produced and water surface effects recorded by a high speed digital camera. Higher driver pressures produced water surface effects which extended beyond the window recorded by the digital camera. The higher resulting pressure in the shock tube expansion chamber also compromised the silicon seals used around the deflector plate in a comparatively low number of tests.

Since the water surface effects result from impulsively loading a deflector plate with a passing shock wave, it is necessary to understand the form and characteristics of that shock wave and to ensure that these are repeatable (within the limits of the experimental apparatus used). The pressure transducer in the shock tube wall allowed analysis of the actual shock wave rising up the shock tube. A typical pressure trace can be seen in figure 4.1.

The shock wave's rising edge consists of two distinct portions. The first rising edge is the high pressure behind the passing shock wave itself as it passes the pressure transducer travelling up the shock tube towards the deflector plate. The second rising edge represents this same high pressure as it is reflected from the deflector plate at the end of the expansion chamber, back towards the driver chamber. In between is a region of constant pressure as the shock wave travels between the pressure transducer and the deflector plate and back (300mm). After the highest pressure is reached there is another region of constant pressure before the expansion wave reflected from the opposite end of the shock tube passes the pressure transducer.

The figure below shows an enlargement of the pressure characteristics described. From it, the times at which each pressure change occurs can be measured.

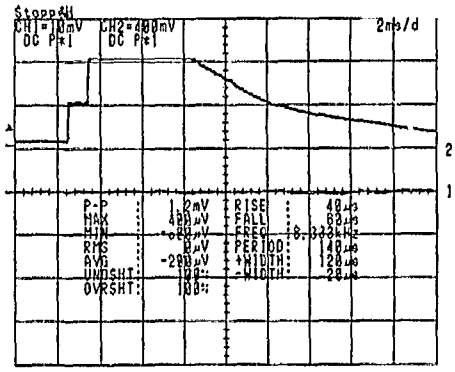

Figure 4.2 Pressure history in the shock tube expansion chamber 150mm from its end

As the shock wave travels up the shock tube, and strikes the flexibly mounted deflector plate, the deflector plate moves upwards against its flexible foam mounting, and then returns to its original position as the pressure in the shock tube normalises. Above the deflector plate is water. As the deflector plate moves upwards, so the water

above it moves upwards under the same action. The deflector plate is curved concave upwards. This curvature it thought to have the effect of directing the water movement towards its geometrical focus specifically by turning and focusing the passing shock wave towards the same geometrical focus, thus producing localised water surface deformation which can be recorded by high speed photography. A typical example of this water surface deformation is shown below.

Figure 4.3 Water jets produced at the water/air interface

Splash effects are noted at the base of the central water surface deformation. It is thought that these are caused by interference between water rising under the influence of the deflector plate movement and shock wave and the inner lip of the deflector plate supporting flange.

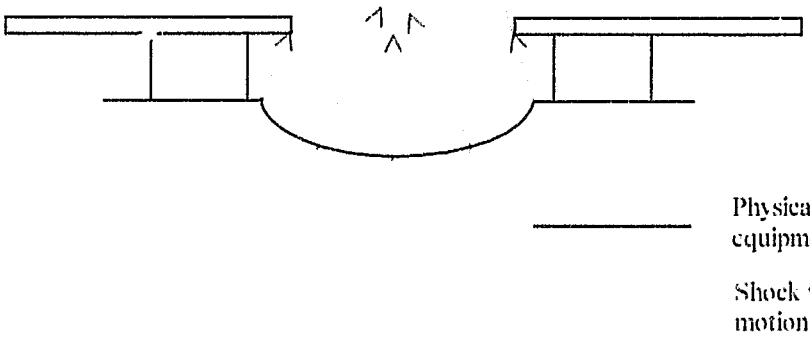

Figure 4.4 Schematic hypothesis of the cause of splash effects at the base of the water jet

Considering the above, an anomalous result was noted by the author (Karnovsky 1998). Using a flat deflector plate, produced a similar water surface deformation to that produced when using a curved deflector plate. It was hypothesised that this

anomaly results because the water surface deformation is caused by a rising column of water, energised by the impulsive loading of the deflector plate below, and not as a result of any focusing process. This is not to imply that the focusing effect is not present, but rather that it is being masked by the overall hydrodynamic flow initiated by the movement of the deflector plate (Karnovsky 1998).

The photographic results obtained could not conclusively prove any of the above. Instead, it was suggested by Professor Skews that a map of the pressures driving the water surface deformation would better clarify its mechanism of formation, and the roles played by different experimental variables such as deflector plate shape, water depth and shock strength. Furthermore, measurement of the pressure field within the water jet itself would give an indication of the energy available within the moving body of water to do useful work. This is important to know, because the overall aim of this research is to explore new techniques for industrial applications such as rock breaking and particle sorting.

For the purpose of measuring pressures below the water surface, a needle hydrophone identical to that used by Müller (Müller 1987) and Mortimer (Mortimer 1997) was used. This particular unit was custom designed by Müller to facilitate his shock wave focusing research. It is now commercially available through Müller Ingenieurtechnik of Aachen Germany (see Appendix A3). Using this particular unit has the advantage that it was specifically designed for an application almost identical to the one at hand, and its effectiveness has been independently verified by Mortimer (Mortimer 1997).

Despite this, initial test results using the needle hydrophone showed inexplicable results. Collaboration with staff members of the department of Electrical Engineering at the University of the Witwatersrand, showed that because of the needle hydrophone's ultra low rise time, the required oscilloscope time/division setting was of the order 20ms/div or less. At this setting, certain of the available oscilloscope units became susceptible to noise which masked the experimental results. The Yokogawa DL1200A unit used in subsequent testing did not exhibit this problem. It was set to trigger on the rising edge of the voltage output by the pressure transducer in the shock tube wall, as the shock wave passed. None of the oscilloscope's built in amplification or filtering functions were used.

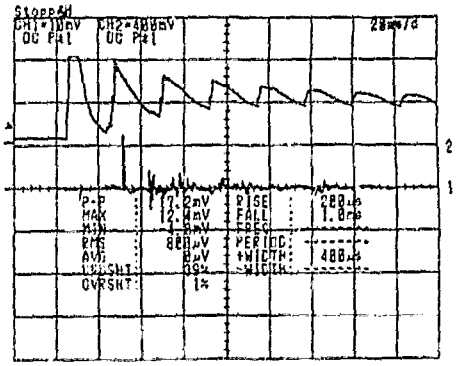

Figure 4.5 Example of a successful test result

In figure 4.5 , the result recorded by the oscilloscope for a successful test is shown. Approximately 25milliseconds after the initial pressure rise in the shock tube, the needle hydrophone registers a sharp pressure rise. This corresponds to a peak output voltage of 12.4mV. Since the sensitivity of the needle hydrophone, as supplied by its manufacturer, is 1.35mV/Bar, the peak output voltage represents a pressure of 16.74Bar at the tip of the needle hydrophone. This pressure is a passing high speed phenomenon. It rises and falls within 1.2ms. The high pressure is followed by a smaller valued but more prolonged negative pressure (approximately –1Bar for 4ms). The combination of a high positive pressure followed by a low negative pressure is consistent with results obtained by others when investigating shock wave focusing (Mortimer 1997, Štuka et al 1995). From 60ms onwards, the needle hydrophone registers a series of small pressure peaks and troughs. These may or may not correspond to the movement of the deflector plate caused by reflection of the now decaying shock wave within the closed shock tube. Other possible causes are reflection of the passing shock wave from the water surface and tank walls, and cavitation effects as the shock wave travels through the water.

It is interesting to note that the shock wave travels the distance between the pressure transducer in the shock tube wall and the deflector plate in approximately 233μs. Despite this, the needle hydrophone only registers a sharp pressure rise approximately 25ms after the initial pressure rise recorded in the shock tube. This delay is ascribed to the inertia of the deflector plate sembly which delays transmission of the shock wave energy from the gas shock below it to the water in the tank above it.

The original experimental objectives were to perform pressure tests using different water levels and shock tube driver pressures. This would lead to maps of the pressure fields driving the photographable water surface effects for different experimental parameters. The pressure maps, in turn, would help to characterise the effects of varying shock strength and water depth on the water jets produced. They could also provide insight on whether a curved deflector plate does in fact focus the passing shock wave at its geometrical focus or not.

To achieve the above, approximately 140 tests were performed and their results recorded. Comparatively few of these tests could be considered successful i.e. showing a distinct high pressure peak as in figure 4.5. The following figure shows a test conducted with a 95mm water level and 3.5Bar driver pressure. No distinct pressure peak is discernable, despite the fact that the needle hydrophone was positioned only 40mm above the centre of the deflector plate.

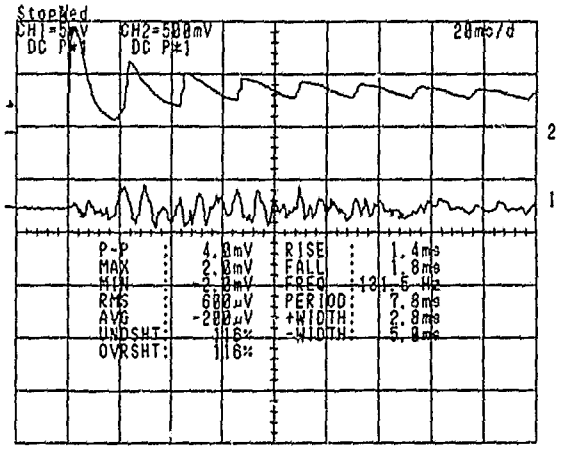

Figure 4.6 Example of an unsuccessful test result

In the above figure, the needle hydrophone registers a series of distinct pressure peaks and troughs over the times 40-120ms. There may be some correlation between these pressure changes and those recorded within the shock tube expansion chamber as the shock wave is reflected between closed ends (Channel 2 in figure 4.6). None of the above pressure peaks are of a form which is easily recognisable as resulting from shock wave focusing – a high pressure peak with very short rise and fall times.

The pressure traces recorded by the oscilloscope did not always remain constant over a number of tests. Some tests showed the surprising result of repeated high pressure peaks with comparatively long rise and fall times. These peaks do not have any obvious correlation with the pressure changes occurring within the shock tube. An example is shown below.

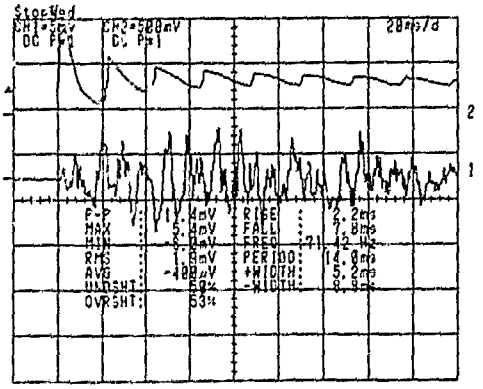

Figure 4.7 Repeated high pressure peaks with comparatively long rise and fall times

It was noticed that the type of test result shown above, would consistently occur in the few tests before significant water leakage from the water tank into the shock tube was noticed. This water leakage always indicated that the silicon seal which sealed the deflector plate to its foam mounting had been compromised. The conclusion drawn from this is that the test result shown in figure 4.7 is caused by air being forced past the silicon seal when a test is run. This leakage becomes progressively worse as testing continues until rising air bubbles in the water tank become noticeable to the naked eye. Once leakage has occurred, it is necessary to drain the water tank and replace the entire deflector plate assembly. This process is particularly disruptive to the testing procedure because of the time it requires, as well as the time required to allow the shock tube itself to dry out. Often leakage was noted as frequently as in five test intervals.

Furthermore, when testing was resumed, the new test results did not necessarily match those recorded with the previous deflector plate assembly. The assembly's stiffness decreases with time as its foam mounting ring becomes more pliable, and the deflector plate itself deforms slightly becoming less rigid.

To avoid the problem of leakage past the silicon seal, two different commercially available sealants were tried (Pratley Flexiseal and Bostik 2638 One-part polyurethane sealant). Both exhibited inferior flexibility and shock resistance to the silicon originally used. The sealing problems outlined, coupled with the need for consistent test results, ultimately necessitated redesign of the deflector plate assembly.

Although the abovementioned problems did not allow a consistent set of test results to be obtained, valuable information was nevertheless recorded. Approximately fourteen test results were similar to those shown in figure 4.5. Of these, the main variations noted are in:

- the amplitude of the peak pressure
- the time at which the peak pressure occurs
- the shape of the peak pressure's rise and fall
- the occurrence of a negative pressure immediately preceding the pressure peak
- the general form of the pressure trace following the peak pressure's rise and fall

4.1 Variation in peak pressure amplitude

Peak pressures recorded ranged from 3.0161Bar to 29.4068Bar. The smallest 3.0161Bar was recorded at the centre of the deflector plate 10mm above the top face of its supporting flange height. This surface (flange height) represented the closest that the needle hydrophone could be positioned to the deflector plate, without risking damage as the deflector plate moved. It was thus used as a datum throughout testing. The lowest (3.0161Bar) peak pressure was actually lower than that recorded at flange height on the centre of the deflector plate (3.7701Bar). The test results are shown below:

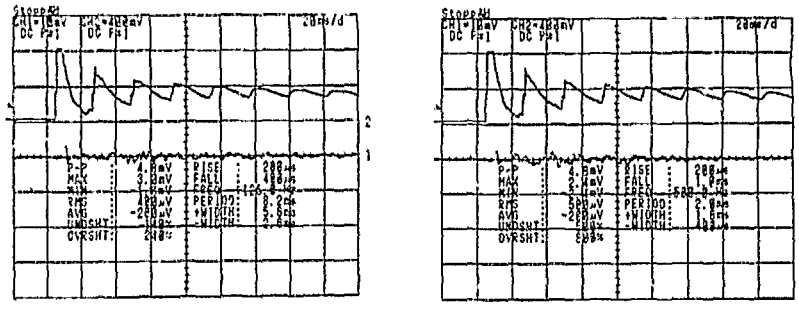

(a) (b)

Figure 4.8 Results for 3Bar driver pressure and 100mm water level with needle hydrophone positioned (a) at flange height (b) 10mm above flange height on the deflector plate axis

The water level in the tank has a decisive effect on the magnitude of the peak pressure recorded in a test. In the above figure, the water level was 100mm above the tank base. In the figure below that water level has been lowered to 45mm. The recorded peak pressure has increased to 29.4068Bar. Thus approximately halving the water level has increased peak pressure almost tenfold.

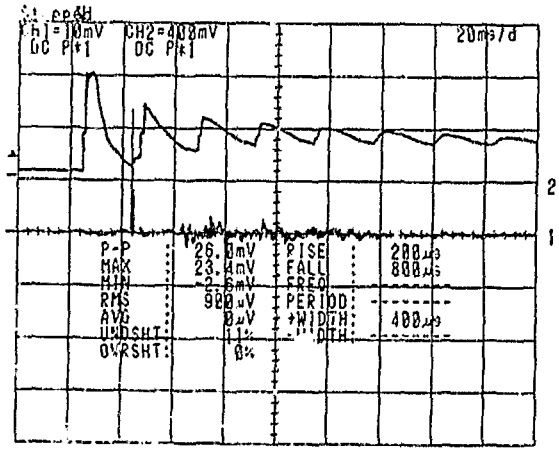

Figure 4.9 Result for 3Bar driver pressure and 45mm water level with needle hydrophone positioned at flange height on the deflector plate axis

In figure 4.8 and figure 4.9 the driver pressure was 3Bar. Interestingly, the time at which the peak pressure occurs is earlier for the higher water level. This despite the higher inertia and hydrostatic pressure resulting from the extra water above the deflector plate.

4.2 Time at which pressure peak occurs

The time at which peak pressure occurs within the recorded test frame varies greatly. In most tests they occur within 40ms of the first pressure rise recorded in the shock tube. In two tests though, the high pressure peaks occur approximately 145ms and 98ms after the pressure rise in the shock tube. Judging by the amplitude of the peaks and troughs in both these tests, leakage of high pressure air from the shock tube into the water tank past a silicon seal is suspected. The effect of this leakage on the characteristics of the high pressure peak is unknown, but it can be assumed that the later time at which this high pressure occurs is related in some way to the leak.

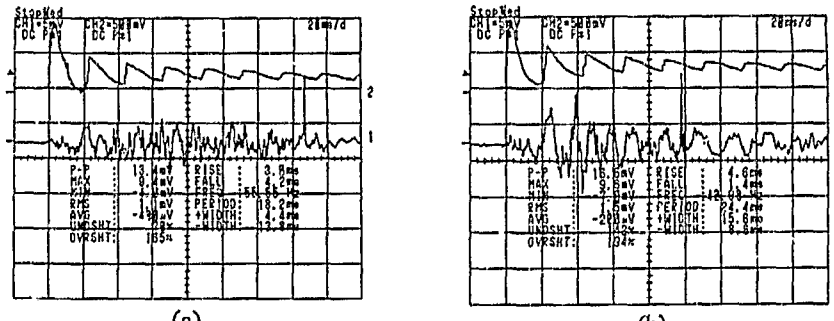

(a) (b)

Figure 4.10 Results for 3.5Bar driver pressure and 95mm water level with needle hydrophone positioned 30mm above flange height (a) on the deflector plate axis (b) 70mm off the deflector plate axis

The following figures show the correlation between the height of the needle hydrophone above the deflector plate and the recorded position of the pressure peak.

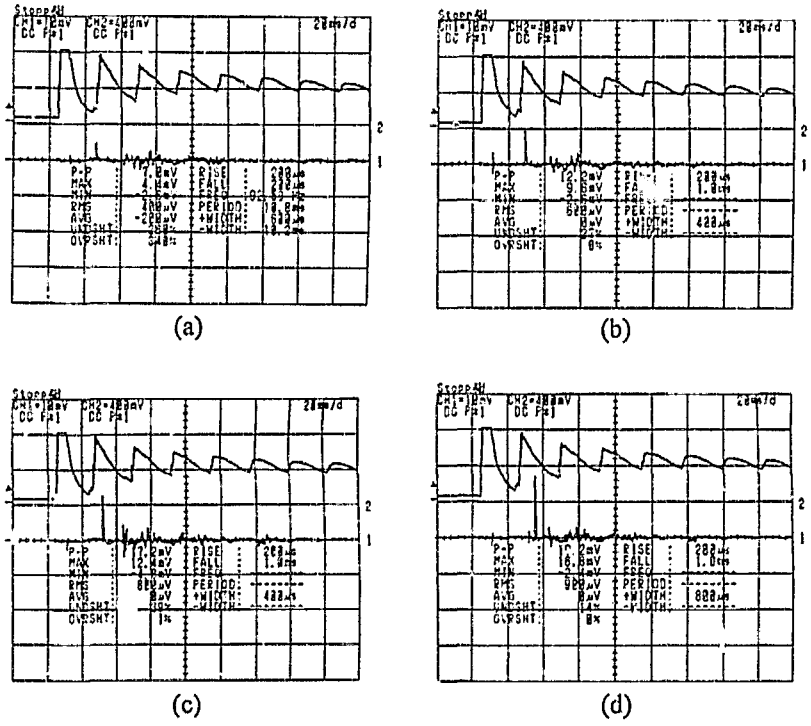

Figure 4.11 Results for 4Bar driver pressure and 65mm water level with needle hydrophone positioned on the deflector plate axis (a) at flange height (b) 10mm (c) 20mm (d) 30mm above flange height

As the needle hydrophone is positioned progressively higher above the deflector plate, so the high pressure peak occurs later in the recorded signal trace. In figure 4.11(a-d) these times are approximately 22ms, 25ms, 30ms and 32ms respectively. This result is to be expected because of the extra distance the shock wave and moving water molecules must travel before reaching the tip of the needle hydrophone as it is raised.

The time at which the high pressure peak occurs does not appear to be highly dependent on the shock tube driver pressure used. In the following figure, the shock tube driver pressure is 6Bar and the needle hydrophone is positioned 30mm above flange height. The high pressure peak occurs approximately 35ms after the high pressure in the shock tube. This is similar timing to figure 4.11, where the shock tube driver pressure is 4Bar.

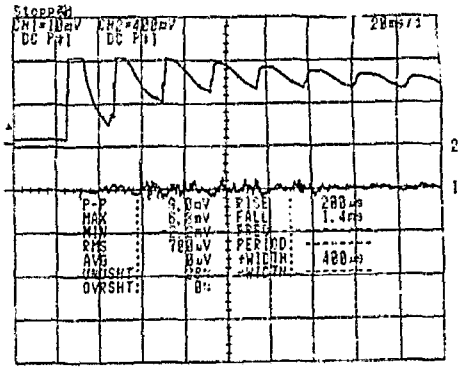

Figure 4.12 Result for 6Bar driver pressure and 65mm water level with needle hydrophone positioned at centre of deflector plate 30mm above flange height

No consistent correlation between the water level in the tank, and the time at which the high pressure peak occurs has been noted.

4.3 Shape of the pressure peak's rise and fall

Each recorded pressure peak is unique to a particular test. Although the pressure peaks, which are considered to represent passing shock waves, have short rise and fall times and a high pressure amplitude, each exhibits characteristics which are not necessarily repeatable. This is illustrated in the following figure.

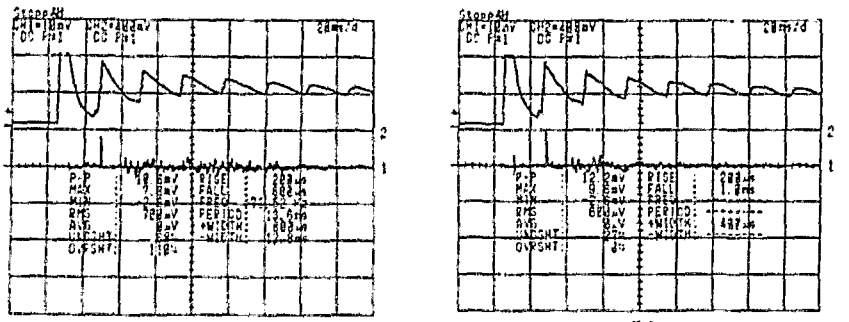

(a) (b)

Figure 4.13 Results for 4Bar driver pressure and 65mm water level with needle hydrophone positioned 10mm above flange height on the deflector plate axis

Although the above two tests were conducted under identical experimental conditions, marked differences in the test results recorded can be seen. Most striking is the difference in pressure amplitudes obtained. This despite the fact that no obvious

differences between the pressure traces recorded in the shock tube (channel 2) can be seen. Furthermore, figure 4.13(b) shows an initial pressure peak and trough approximately 6ms after the initial pressure rise in the shock tube, which is far more pronounced than the equivalent in figure 4.13(a). Both of the main pressure peaks are immediately followed by negative pressure troughs but this phenomenon is more pronounced in figure 4.13(b).

One consistent set of test results was obtained which showed the change in peak pressure as the needle hydrophone is positioned consecutively higher above the centre of the deflector plate. In figure 4.11 the deflector plate used had a focal length of 65mm. This coincides roughly with the positioning of the needle hydrophone in figure 4.11(d) above the flange height. Thus, from the above, it can be seen that peak pressure increases as pressure measurements are taken further away from the surface of the deflector plate and closer to its geometrical focus.

The shape of the pressure peak recorded by the oscilloscope varies depending on the needle hydrophone's height above the deflector plate. This is because the peaks' rise and fall times remain similar irrespective of height above the deflector plate. Pressure amplitudes however increase with increasing distance above the deflector plate. The result of this is that pressure peaks recorded closer to the deflector plate appear short and broad while those recorded further away appear tall and narrow.

4.4 Occurrence of a negative pressure immediately before and after the pressure peak

Most of the pressure peaks recorded are immediately followed by a noticeable negative pressure.

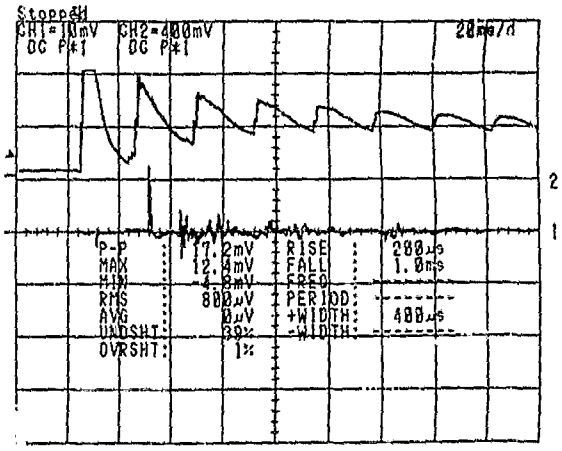

Figure 4.14 Result for 4Bar driver pressure and 65mm water level with needle hydrophone positioned 20mm above flange height. Illustrates the negative pressure immediately following the high pressure peak

This negative pressure represents an expansion wave immediately following the high pressure shock wave travelling through the water. It is thought to originate either at the corners of the deflector plate as the shock wave passes, or at the inner edges of the deflector plate supporting flange or bolt fastenings. Considering the progression of tests shown in figure 4.11, the negative pressure wave occurs about 8ms after the high pressure, but this time interval decreases and the negative pressure's amplitude increases as the needle hydrophone is moved further away from the deflector plate. This behaviour is consistent with an expansion wave which gradually steepens and catches up with the travelling shock wave ahead of it.

Some test results display a distinct negative pressure ahead of the recorded high pressure as shown below.

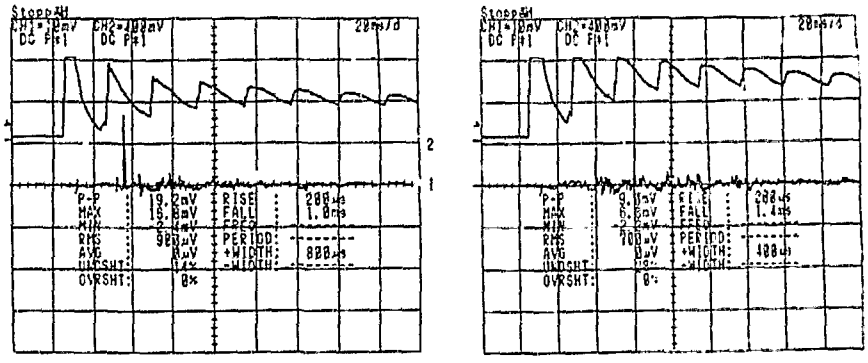

(a) (b)

Figure 4.15 Results for (a) 4Bar (b) 6Bar driver pressure and 65mm water level with needle hydrophone positioned 30mm above flange height on the deflector axis

This phenomenon is not consistent throughout the recorded results, nor is its form. In figure 4.15(a) the preceding negative pressure is similar in form to that following the high pressure. This gives the high pressure trace a symmetrical appearance. In figure 4.15(b) the wave is not followed by an appreciable expansion and hence the preceding negative pressure is not repeated after the high pressure trace.

4.5 General form of the pressure trace following the peak pressure's rise and fall

Test results recorded by the oscilloscope cover a 200ms interval. The initial pressure rise in the shock tube occurs at approximately 25ms on the time scale. Following this, a high pressure is recorded in the water tank generally within 40ms depending on experimental conditions. This high pressure is thought to represent the shock wave travelling through the liquid medium towards its focus. Once this shock wave has passed, the pressure trace continues to oscillate about its steady state axis, indicating rapid but low amplitude pressure variations. This behaviour is seen in every recorded test result.

Two possible explanations are proposed. The first is that cavitation bubbles occur in the liquid behind the passing shock wave. These cause the recorded pressure variations as they pass the needle hydrophone. Štuka et al.(1995) have found that in non-degassed water, the cavitation threshold is lower than 0.5MPa. Thus where a negative pressure is recorded after the shock wave, cavitation could well occur. This is further verified by photographic results (Karnovsky 1998) where dark regions observed below the water surface are thought to be rising clouds of cavitation bubbles.

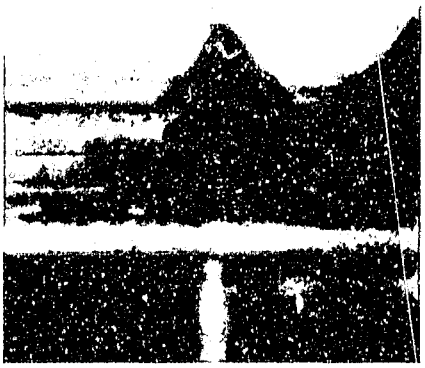

Figure 4.16 Photographic test result showing a dark cloud below the water surface thought to be cavitation bubbles

The second explanation is that the pressure variations are caused by the physical movement of the deflector plate against its flexible mounting, driven by the high pressure behind the shock wave. However it is questionable whether the inertia of the materials involved would allow them to respond so quickly to the high pressure, that they could set up pressure variations in the water tank which are recorded just 40ms after the shock wave has passed.

5. Results Using Bellow Deflector Plate Assembly

The overall thrust of the current research is to develop water jets which can be used in industrial applications. A novel method for producing water jets using a flexibly mounted deflector plate driven upwards by a shock wave has been developed (Karnovsky 1998). To gain more insight it is necessary to characterise the underwater pressure fields which drive the water jets.

Chapter 4 has presented and explored pressure measurement tests which were intended to map the underwater pressure fields. Although a number of individual tests were successful, the majority did not record useable results. This due to frequent changes of the deflector plate assembly when leakage of water from the water tank into the expansion chamber was noted.

A new deflector plate assembly using a bellow to provide flexibility (see section 3.1) was designed to overcome the above problem. This new assembly incorporated a displacement limiter to avoid excessive bellow extension. The results obtained are detailed below.

5.1 Water jets produced with the bellow system

The water jets produced by the bellow system with displacement limiter are similar to those photographed using the original foam ring deflector plate assembly (Karnovsky 1998). A series of photographs showing development and decay of these jets can be found in Appendix A1.

Figure 5.1 Water jet produced using the bellow deflector plate assembly

The bellow with displacement limiter is more flexible and allows the deflector plate greater vertical movement than the hard body deflector plate assembly originally had. Despite this greater shock tube driver pressures were required to produce comparable results. It is thought this is due to the inertia of the water which must be displaced by the top flange on the displacement limiter during vertical movement.

A number of tests recorded a tearing of the water surface, similar to that documented by Mortimer (1997). This effect could result as the shock wave is reflected from the water/air interface. It is shown below:

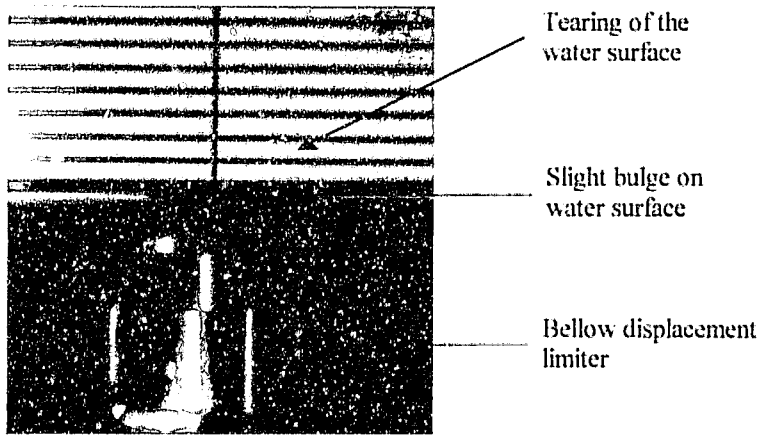

Figure 5.2 Tearing of the water surface as the shock wave is reflected from the water/ air interface

5.2 Pressure measurement results

Pressure measurements were conducted using the same 3-D needle hydrophone positioning system and needle hydrophone previously described. No changes other than replacement of the deflector plate assembly and the addition of a displacement limiter were made to the experimental equipment.

Over 120 tests were conducted and recorded to obtain data from which a map of the pressure field set up below the water surface by the deflector plate movement could be constructed. During these tests, the current bellow system proved superior to the previously used deflector plate assembly in terms of consistency and reliability of results. No changes or replacements were required throughout testing, which was particularly advantageous.

All pressure measurements were conducted at a water level of 120mm measured from the base of the water tank. This gave a 50mm region between deflector plate height and the water surface in which pressure measurements could be taken. The water level above the deflector plate was sufficient to effectively damp any violent water surface effects which could potentially have damaged the needle hydrophone. The datum level for the needle hydrophone was taken as the top surface of the displacement limiter, which was the same height as the outer edges of the deflector plate in its rest position. The lowest possible positioning of the needle hydrophone tip was at least 5mm above the displacement limiter top flange, as both deflector plate and displacement limiter were free to move 5mm upwards during testing.

5.3 Pressure measurement results at varying heights on the axis of the deflector plate

In the first set of pressure measurements undertaken, the needle hydrophone was positioned at the centre of the deflector plate and results recorded for tests at incremental needle hydrophone heights. The progression of results is shown below.

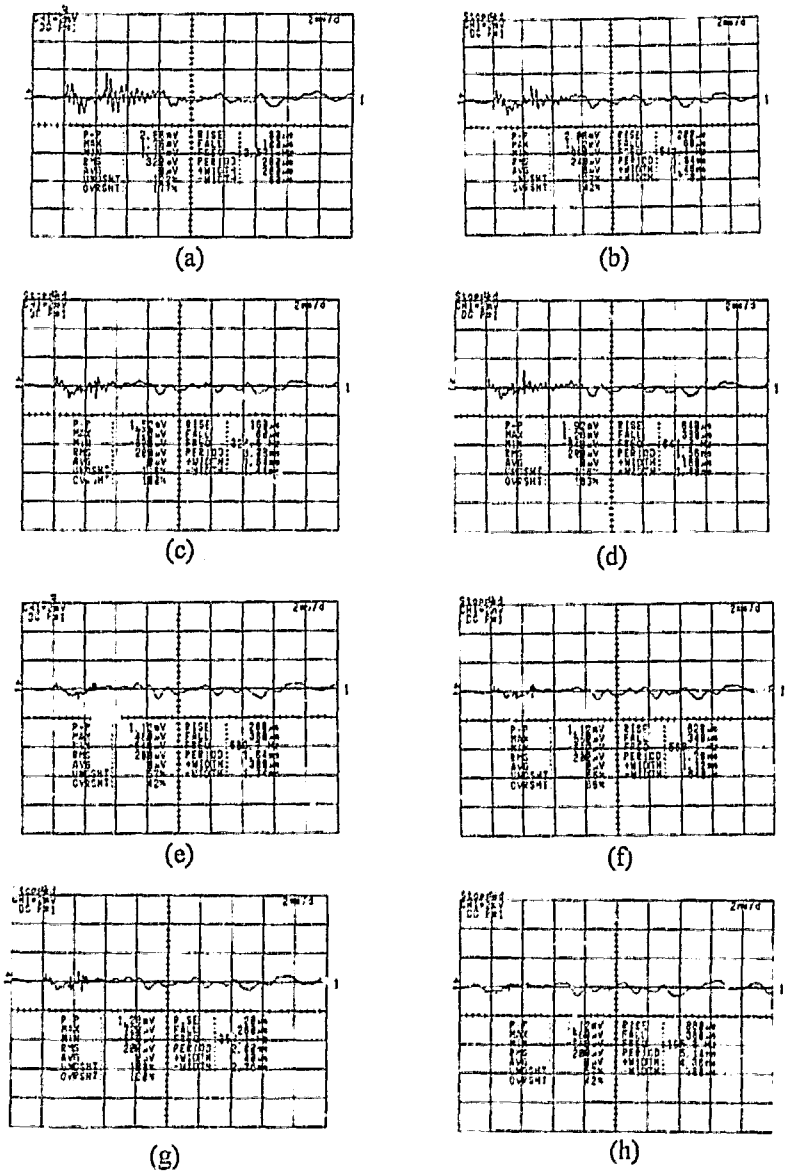

Figure 5.3 Results for 3.5Bar driver pressure and 120mm water level with needle hydrophone positioned on deflector plate axis (a) 5mm (b) 10mm (c)15mm (d) 20mm (e) 25mm (f) 30mm (g) 35mm (h) 40mm above flange height

In figure 5.3 the largest pressure amplitude is recorded closest to the deflector plate. Since the needle hydrophone's sensitivity is 1.35mV/Bar, the recorded pressure amplitude is 3.890Bar. This recorded pressure decreases consistently with increasing distance away from the deflector plate. Close to the water surface, the recorded pressure is 1.5147Bar (figure 5.3(h)) and the pressure peak is hardly distinguishable on the pressure trace. Despite this decreasing pressure amplitude, as testing progresses away from the deflector plate so the results show a change from a number of distinct pressure peaks to one distinct peak (figure 5.3(d)).This effect is due to diffraction and near-field edge effects as opposed to steepening – which would require a larger time frame or distance to occur because of the low pressure wave amplitude.

In figure 5.3 a number of tests seem to suggest that positive recorded pressures are followed by negative recorded pressures and vice versa. This oscillation is highlighted in the figure below.

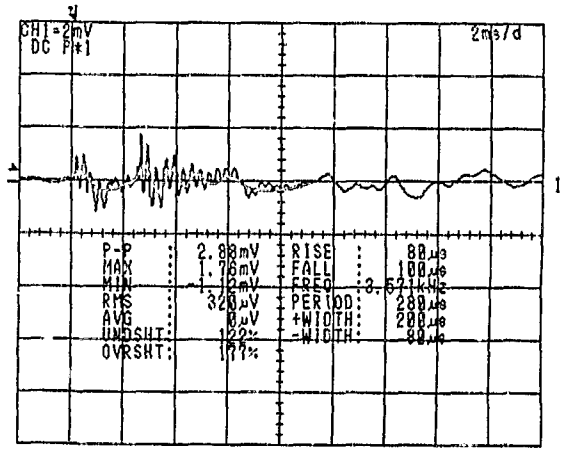

Figure 5.4 Result highlighting the oscillation between positive and negative pressures

It is also interesting to note that most of the pressure variations recorded occur within the first 8ms after the oscilloscope has triggered, the pressure trace flattening and spreading out thereafter. To explore the behaviour of the system over a longer time frame, the tests of figure 5.3 were repeated at both 2ms/div and 20ms/div consecutively. Sample results are shown:

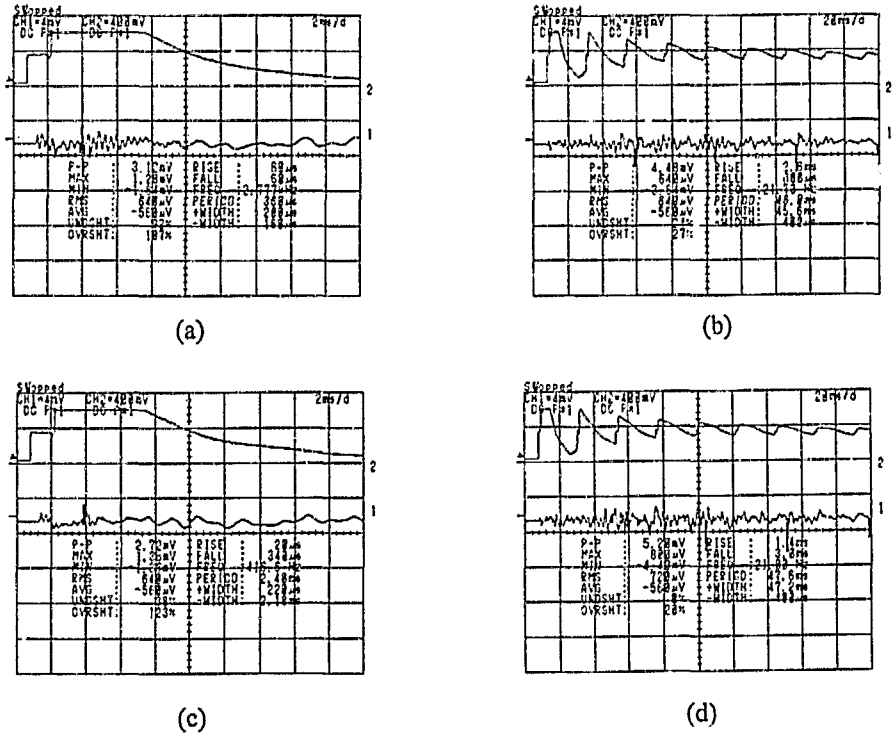

Figure 5.5 Two sets of tests repeated using different time/division oscilloscope settings: (a+b) Results for 3.5Bar driver pressure and 120mm water level with needle hydrophone positioned 5mm above flange height

(c+d) Results for 3.5Bar driver pressure and 120mm water level with needle hydrophone positioned 10mm above flange height

Periodically spaced negative peaks are noted in figures 5.5(b+d). Their cause cannot be accurately pinpointed, but their periodicity and consistency in both tests suggest that they are real phenomena and not attributable to experimental error. These negative peaks do not appear in tests where the needle hydrophone is positioned more than 10mm above the displacement limiter.

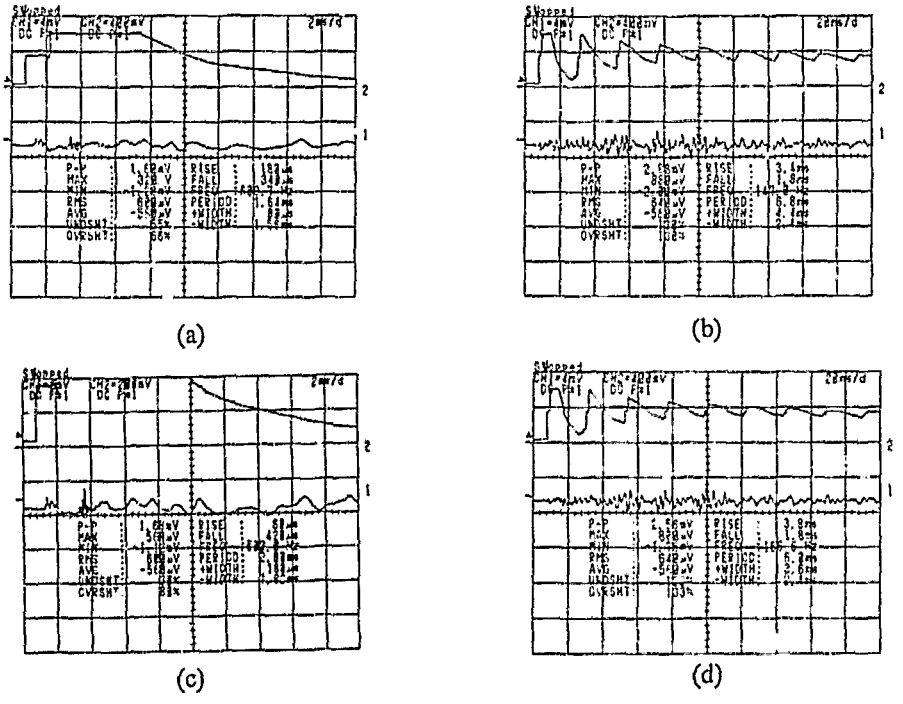

Figure 5.6 Two sets of tests repeated using different time/division oscilloscope settings: (a+b) Results for 3.5Bar driver pressure and 120mm water level with needle hydrophone positioned 15mm above flange height

(c+d) Results for 3.5Bar driver pressure and 120mm water level with needle hydrophone positioned 20mm above flange height

Tests conducted at the 20ms/div oscilloscope setting are instructive, but do not provide the resolution necessary to analyse the actual shock wave focusing phenomenon. Judging from the tests already run, the shock wave seems to pass the needle hydrophone within 10ms of the initial pressure rise in the shock tube. For this reason, a 2ms/div oscilloscope setting was used in subsequent tests.

5.4 Pressure measurement results at constant height and varying needle hydrophone positions

To build a map of the underwater pressure fields requires pressure measurements at various points in the water tank. Measurements were taken at 5mm height increments.

The needle hydrophone was positioned at a chosen height and its position along the length (expressed as a distance in front of or behind the deflector plate's axis of symmetry) of the water tank varied in 5mm increments. Test conditions were 3.5Bar shock tube driver pressure and 120mm water level throughout testing. The results are summarised below. To infer the pressure field at a given height in a particular position, the maximum pressures recorded in two tests symmetrically in front of and behind the deflector plate axis were averaged. These pressure fields are combined to form an overall pressure map above the moving deflector plate.

5.4.1 5mm above the deflector plate

Only two tests were conducted with the needle hydrophone 5mm above the deflector plate. The results are shown below:

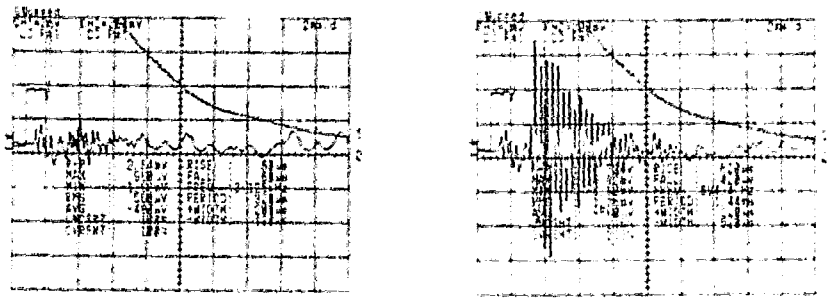

(a) (b)

Figure 5.7 Results for 3.5Bar driver pressure and 120mm water level with needle hydrophone positioned 5mm above flange height (a) on deflector plate axis (b) 5mm in front of deflector plate axis

In figure 5.7(b) where the needle hydrophone was positioned 5mm off the deflector plate axis, disproportionately large pressure peaks are noted. These are considered too large to represent the passing shock wave. Rather they may represent contact between the deflector plate and the tip of the needle hydrophone. The needle hydrophone was checked after the test and found to be functioning correctly. No further tests were conducted at this height above the deflector plate.

5.4.2 10mm above the deflector plate

When the needle hydrophone is at this height, a single distinct pressure peak is recorded at the centre of the deflector plate. This is not recorded in any other position at this height.

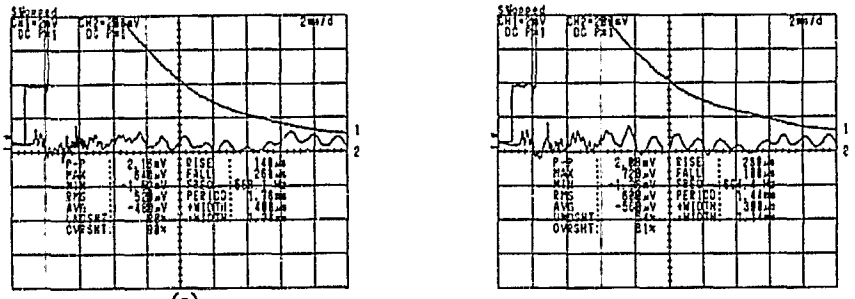

(a) (b)

Figure 5.8 Results for 3.5Bar driver pressure and 120mm water level with needle hydrophone positioned on the deflector plate axis 10mm above flange height

Two other notable tests were recorded 5mm in front and 15mm behind the deflector plate axis. The results are shown below:

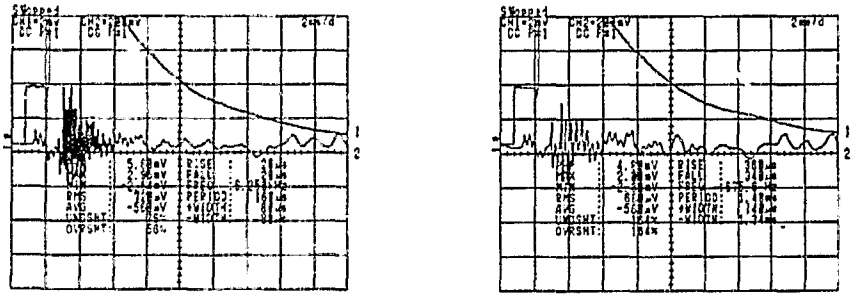

(a) (b)

Figure 5.9 Results for 3.5Bar driver pressure and 120mm water level with needle hydrophone positioned 10mm above flange height (a) 5mm in front of deflector plate axis (b) 15mm behind deflector plate axis

In figure 5.9(a) the needle hydrophone was in the same position but 5mm above figure 5.7(b). This might suggest that the result shown in figure 5.7(b) is in fact a true pressure measurement and did not indicate contact between the deflector plate and needle hydrophone.

The following pressure field can be inferred 10mm above the deflector plate rest height.

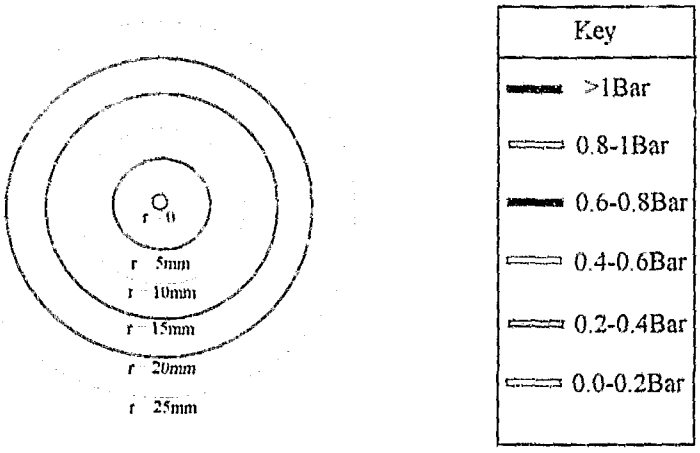

Figure 5.10 Pressure field 10mm above deflector plate

5.4.3 15mm above the deflector plate

Two separate tests confirmed the existence of high pressure peaks on the deflector plate axis. Unlike figure 5.8(a) above, these peak pressures are recurring and not just concentrated in one peak. The average maximum peak pressure on the deflector plate axis 15mm above the deflector plate is 3.24Bar

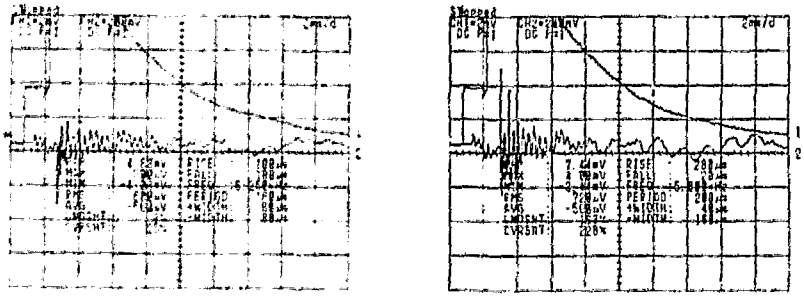

Figure 5.11 Results for 3.5Bar driver pressure and 120mm water level with needle hydrophone positioned 15mm above flange height on deflector plate axis

It is noted that large negative pressures accompany the positive pressures recorded on the axis of the deflector plate.

Consistent distinct pressure peaks are recorded 10mm off the deflector plate axis. Pressure peaks were also recorded 5mm and 15mm off the deflector plate axis, but these were not repeatable.

The following pressure field can be inferred 15mm above the deflector plate rest height.

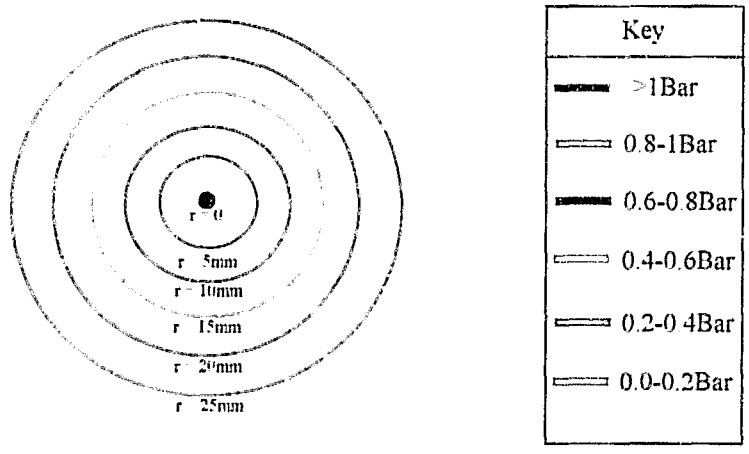

Figure 5.12 Pressure field 15mm above deflector plate

5.4.4 20mm above the deflector plate

At this height, single distinct pressure peaks are recorded on the deflector plate axis and 5mm in front of it but these are not consistent as shown below:

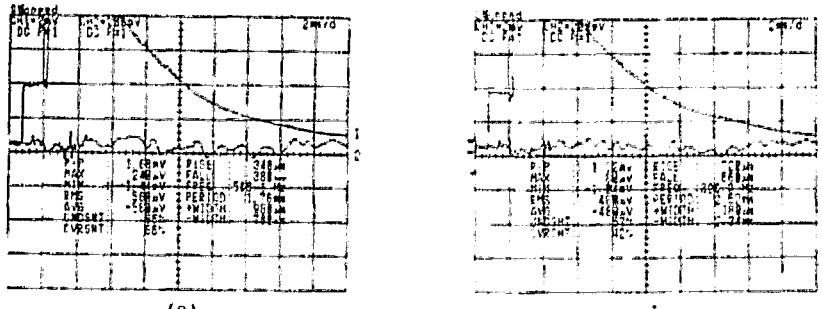

Figure 5.13 Results for 3.5Bar driver pressure and 120mm water level with needle hydrophone positioned 20mm above flange height on deflector plate axis

The following pressure field can be inferred 20mm above the deflector plate rest height.

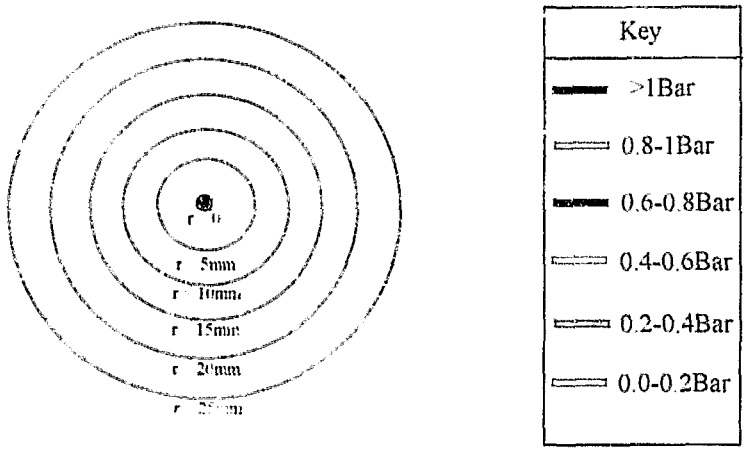

Figure 5.14 Pressure field 20mm above deflector plate

5.4.5 25mm above the deflector plate

Pressure peaks are recorded on the deflector plate axis. These are of low amplitude and their form varies from test to test.

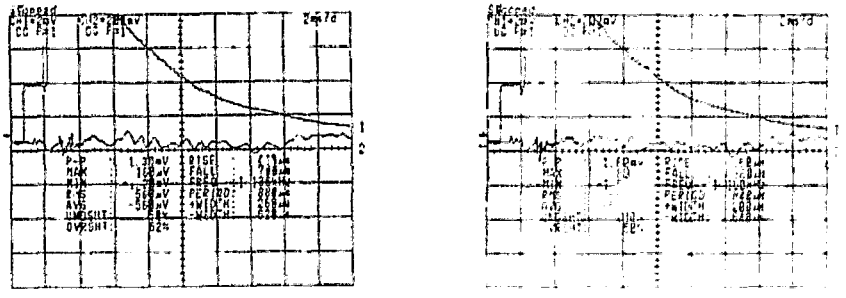

(a) (b)

Figure 5.15 Results for 3.5Bar driver pressure and 120mm water level with needle hydrophone positioned 25mm above flange height on deflector plate axis

No other repeatable flow features were recorded at this height, although two tests showed pressure peaks 10mm and 15mm behind the deflector plate.

The following pressure field can be inferred 25mm above the deflector plate rest height.

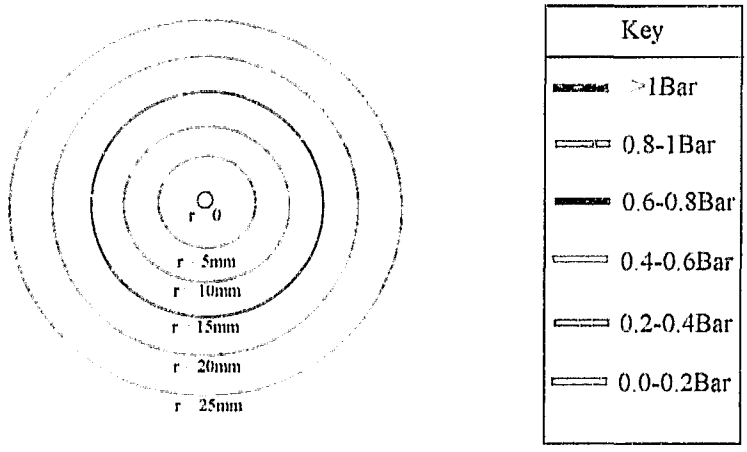

Figure 5.16 Pressure field 25mm above deflector plate

5.4.6 30mm above the deflector plate

No distinct pressure peak is recorded on the deflector plate axis. In front of and behind the axis, pressure variations are noted in the time frame where the shock wave is expected to pass the needle hydrophone (approximately 2ms after the first pressure rise in the shock tube). 15mm Behind the deflector plate axis a small pressure peak is recorded while 10mm in front of the deflector plate axis a steepening of the pressure trace occurs. This steepening is recorded for a number of tests at this needle hydrophone height.

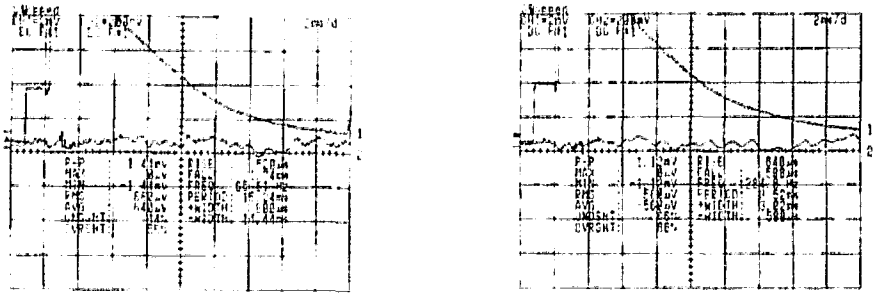

Figure 5.17 Results for 3.5Bar driver pressure and 120mm water level with needle hydrophone positioned 30mm above flange height (a) 15mm behind (b) 10mm in front of the deflector plate axis

The following pressure field can be inferred 30mm above the deflector plate rest height.

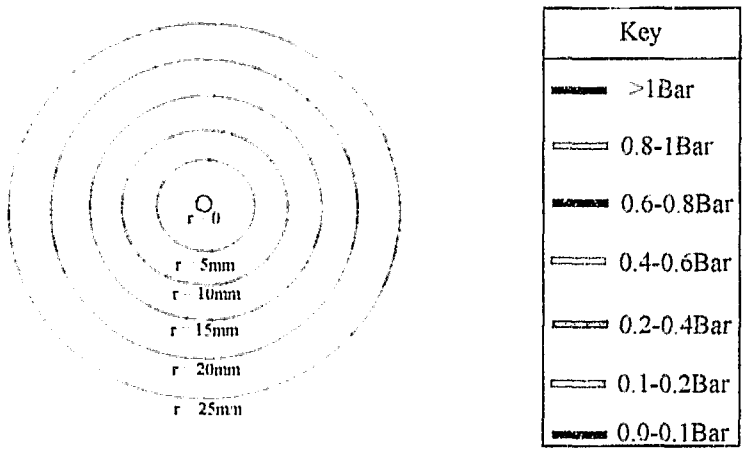

Figure 5.18 Pressure field 30mm above deflector plate

5.4.7 35mm above the deflector plate

Slight steepening of the recorded pressure trace is noted on the deflector plate axis and single peaks were recorded 10mm and 30mm in front of the axis.

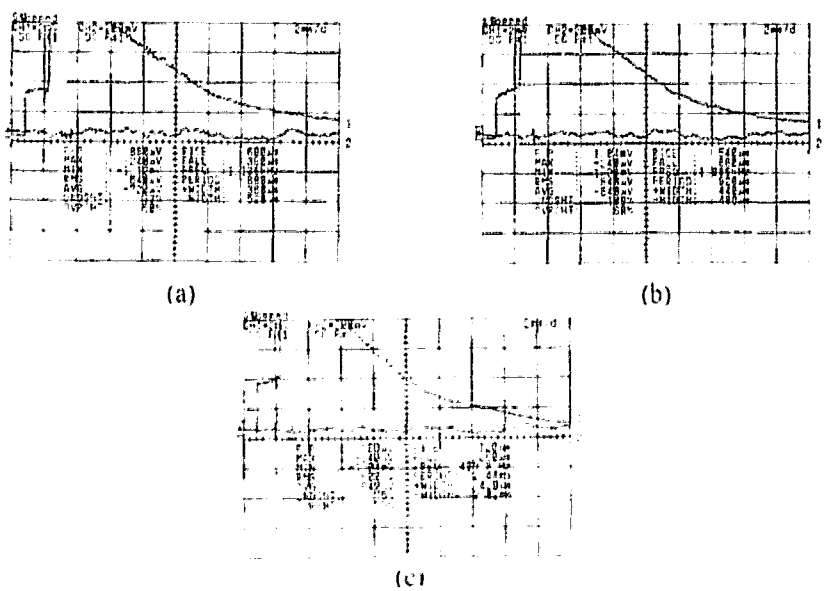

Figure 5.19 Results for 3.5Bar driver pressure and 120mm water level with needle hydrophone positioned 35mm above flange height (a) on the centre of (b) 10mm in front (c) 30mm in front of the deflector plate axis

The following pressure field can be inferred 35mm above the deflector plate rest height.

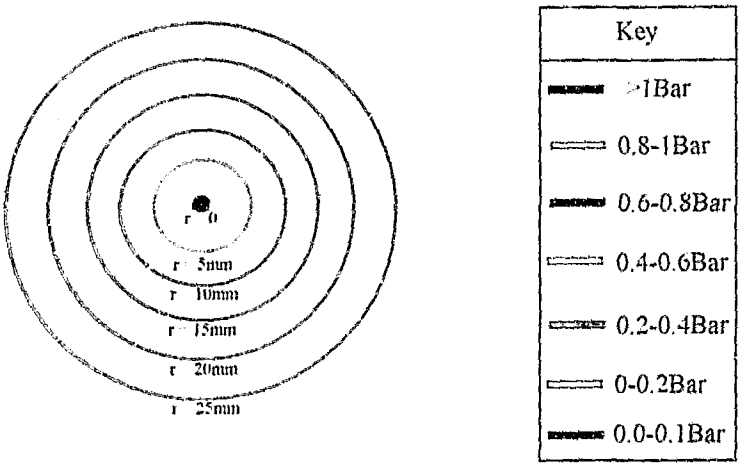

Figure 5.20 Pressure field 35mm above deflector plate

6. Appendix

Proper use of Autodyn required [illegible] trial and error, a working simulation [illegible] important features of the physical experimental setup [illegible] such initial input to Autodyn.

[illegible] Outlet nozzle left [illegible] the sealing shoe!

wave. This high pressure region is in direct contact with a spherically shaped deflector plate. The deflector plate material is stainless steel. Stainless steel offers greater stiffness than copper, preventing flexing and deformation during the simulation. To increase simulation speed - by increasing the grid spacing on the water subgrid, which is the largest subgrid defined - the deflector plate thickness is defined as 2mm. This as opposed to the 0.5mm thick deflector plate used in the actual experiment. In front of the deflector plate is a water region and in front of that air at atmospheric conditions.

For convenience the problem setup has been entered into Autodyn horizontally. Gravity has accordingly been defined in the negative x direction.

In the experiment, an elliptically shaped deflector plate shape was pressed in a custom designed die. Autodyn does not incorporate a predefined elliptical shape. The closest predefined shape is a sphere. Thus a spherically shaped deflector plate has been used.

Separate subgrids were defined for the shock and deflector plate. The water and atmospheric air share the same subgrid. The shock and water/atmospheric air subgrids are defined as Eulerian while the deflector plate subgrid is defined as Lagrangian. The nodes of an Eulerian subgrid remain static throughout the simulation, while the material moves independently within the defined geometrical limits. In a Lagrangian subgrid, the nodes are attached to the material and hence the subgrid distorts as the material moves. Interactions between Lagrangian and Eulerian subgrids are selected by defining a polygon around the Lagrangian subgrid and specifying with which Eulerian subgrid it is to interact.

Boundaries allowing material in/outflow from any of the Eulerian subgrids can be added as required. These were experimented with, but none were found to make a significant difference to the simulated results. They were therefore not included.

In figure 6.1 when defining the air subgrid on the extreme left, representing the high pressure region behind the shock wave, the following material properties have been used:

Material name : GAIR
Density: 5.0190kg/m^3
Internal Energy: 673.3277E3 J/kg
Velocity (x, y, radial): 0m/s

The shock subgrid extends beyond the deflector position in figure 6.1 to allow the high pressure shock subgrid to remain in contact with the steel deflector plate as it moves forward.

The steel deflector subgrid is 2mm thick. It is free to deform as the simulation progresses and interacts with both the shock wave and water subgrids. Excessive deformation is avoided by defining the deflector plate material as stainless steel instead of copper. Defining deflector plate thickness as 2mm instead of the experimental 0.5mm allows a coarser subgrid definition, minimising processing time. The material properties used are:

Material name: STNLS STEEL
Density: 7860kg/m^3
Internal Energy: 134.1E3 J/kg
Velocity (x, y, radial): 0m/s

To the right of the deflector plate is a 124mm water region. The water material properties used are:

Material name: GWATER
Density: 1000kg/m^3
Internal Energy: 45900.8270 J/kg
Velocity (x, y, radial): 0 m/s

As the deflector plate is forced forwards by the high pressure behind it, so it in turn forces the water forwards producing a noticeable surface bulge. A void region develops immediately in front of the deflector plate. This occurs as a matter of course in Autodyn, possibly representing a region in which cavitation occurs. Using different predefined water models does lessen the impact of the void areas on the simulation, but does not eliminate them completely. This remains so even when the material properties of the water model used are changed so as not to allow material failure. The void region does have the advantage of highlighting the gross water movements through the contrast of different material colours and hence improving the users understanding of the relevant water dynamics.

Above the water surface is air at atmospheric conditions. The material properties used are:

Material name: GAIR
Density: 1.2029kg/m^3
Internal Energy: 191.4408E3 J/kg
Velocity (x, y, radial): 0m/s

All material definitions require an internal energy. For fluids, the following equation has been used (Müller 1987):

$$e = \frac{p + B}{\rho(n-1)}$$

Where: e = Internal energy (J/kg)
p = Pressure (Pa)
ρ = Density (kg/m^3)
B, n = Material constants

For stainless steel the following internal energy equation has been used:

$$e = c_v \Delta T$$

Where: e = Internal energy (J/kg)
c_v = 0.447
T = Temperature (K)

The above equations, although well known and widely used, are not referred to in the Autodyn Users Manual and could not be confirmed with the program vendors. It is assumed that they are correct for calculating the internal energy of a fluid and solid as required by the material properties input prompts.

No boundaries or constraints other than the geometrical limits of each subgrid have been imposed on the movement of materials throughout the simulation. These geometrical limits are based on those found in the physical experiment.

To control the magnitude of the water surface effects produced during the simulation, the shock and deflector subgrids are deactivated after a specified time. When a subgrid is deactivated, it remains visible on the screen but is not considered any further by the simulation. Depending on the simulation setup, the shock and deflector subgrids were deactivated when the simulation reached 15-50μs real time.

Autodyn incorporates an axial symmetry function, allowing the user to define only one half of a symmetrical simulation setup and have the program mirror it around the horizontal axis. Using this feature has the advantage of conserving computer resources and hence improving processing speed. Initially the axial symmetry function was used, but more accurate results were obtained by defining the experimental setup in its entirety. It is suspected that this is because of the mathematical singularity which results close to the axis of symmetry when processing an axisymmetric simulation.

Below are a set of thumbnail images showing the progression of results through the simulation

(a)

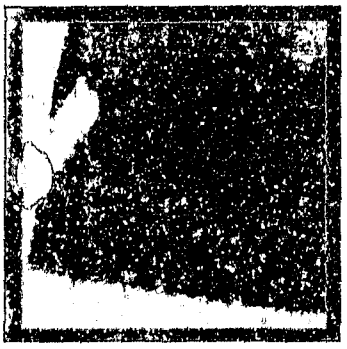

(b)

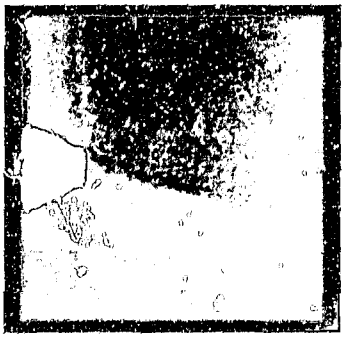

(c)

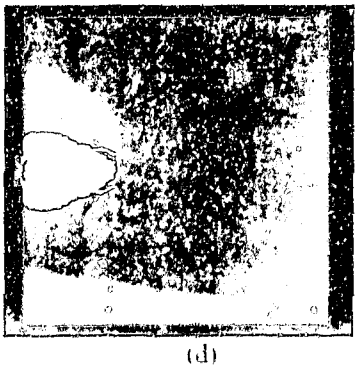

(d)

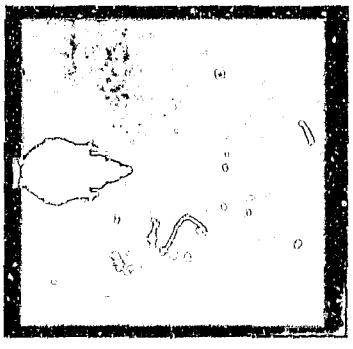

(e)

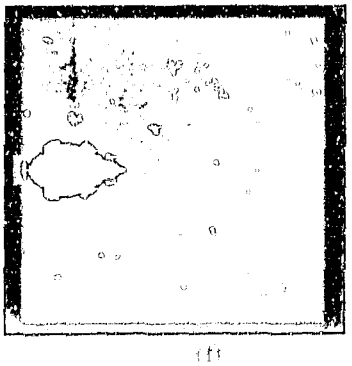

(f)

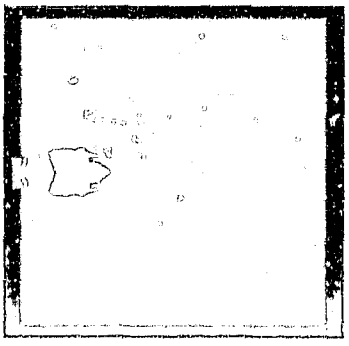

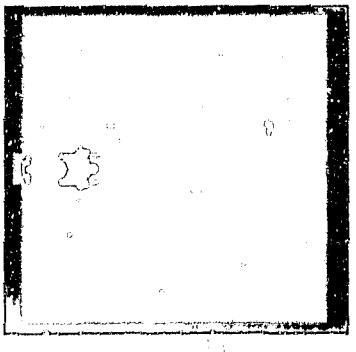

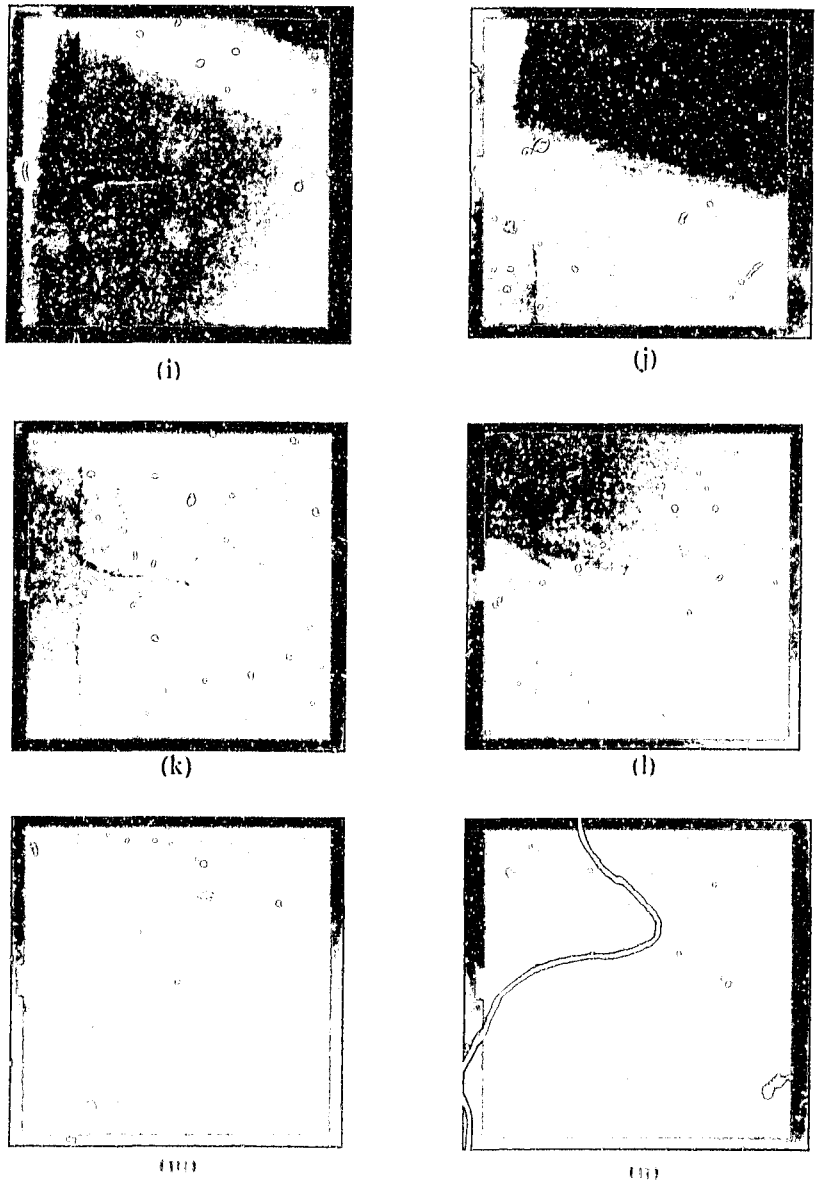

Figure 6.3: Phases [illegible] cavities and [illegible]

Good [illegible] and those [illegible] frames.

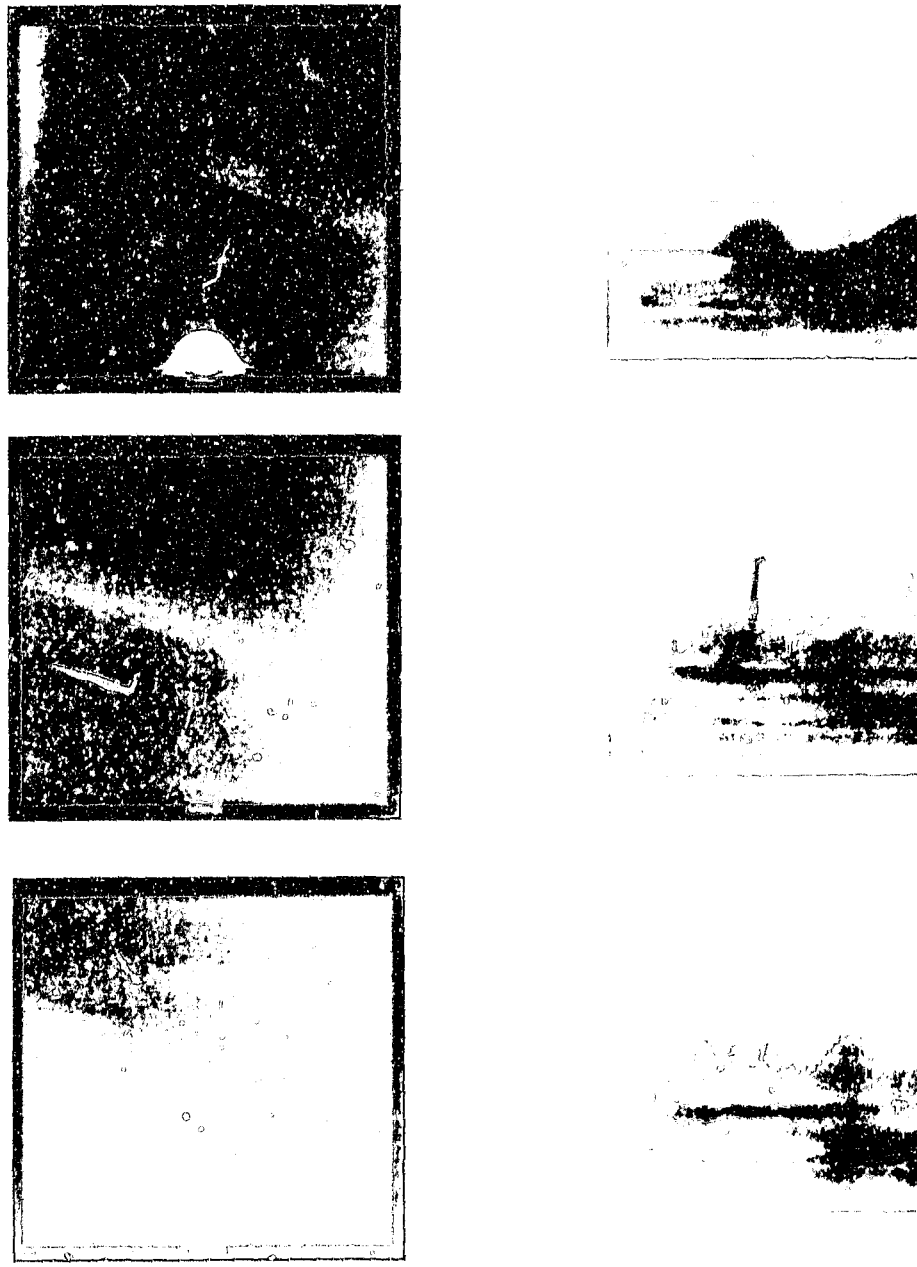

Figure 6.3 Comparison of simulated and physical results

Using Autodyn to simulate the experimental results allows greater resolution and hence insight into the mechanism of formation of the water jets which are the focus of this study. The simulation shows that as the deflector plate moves forwards, so a pressure field is set up in the water ahead of it. The movement of the deflector plate also causes a bulge in the water surface. This bulge becomes the base from which the water jet will grow. The most significant flow field created by movement of the deflector plate is the water flow which under the influence of the pressure field moves away from its rest position, roughly directed towards the outer sides of the water tank. When the deflector plate ceases moving (subgrid deactivated) the water which has been forced outwards then moves back towards the centre of the tank. As this water returns, it meets in the centre of the deflector plate with water returning from the opposite direction. These two "walls" of moving water are forced upwards by their own inertia, forming a tall narrow column of rising water which is seen as a water jet. This process can be seen in figure 6.2.

7. Discussion

The objectives of the current research were to further explore the mechanism of formation of the water jets already presented by the author (Karnovsky 1998). Maps of the underwater pressure fields driving these jets would clarify whether they are the result of a shock wave focusing process in which the focal point coincides with the water surface, or some other physical phenomenon.

To this end, test equipment was required which would facilitate pressure measurements in the area of the water jets produced. An existing vertically mounted gas shock tube was used as the basic test rig. By subjecting a submerged deflector plate to a shock wave from below, a water jet was produced on a free water surface

Previous authors (Müller (1987), Mortimer (1997)) also working in the field of shock wave focusing, had used a needle hydrophone to take pressure measurements of passing shock waves. The needle hydrophone is a custom designed pressure transducer with very small sensitive diameter and ultra short rise time. Its specifications matched the requirements of the current research. A positioning system which allowed accurate 3-D positioning of the needle hydrophone within the test section was designed as an attachment to the existing test rig. The first such system was computer controlled, driven by stepper motors but did not provide the accuracy and repeatability required. It was modified to be manually operated. The result was measurable accuracy to within 0.5mm of any required position.

In the first set of pressure measurements undertaken, pressure fields in the water were set up using the same deflector plate assembly previously documented by the author (Karnovsky 1998) to produce photographable water surface effects. Here a curved deflector plate was mounted against a high density foam ring, for vertical flexibility, and supported from above by a steel flange. However repeated failure of a silicon seal disrupted testing and prevented continuity of results. It became obvious that a redesign of the deflector plate assembly was required. Despite this, valuable information had been collected.

Approximately 25ms after the shock wave passed a pressure transducer 150mm below the deflector plate a sharp pressure rise would be recorded by the needle hydrophone often followed by a weak negative pressure. This form of pressure trace has been documented by others working in the field of shock wave focusing (Mortimer 1997, Štuka et al 1995). The water level above the deflector plate has a decisive effect on the peak pressure recorded by the needle hydrophone. In one instance, halving the water level increased peak pressure almost tenfold. For a constant water level, peak pressure at flange height would tend to decrease 10mm above flange height and then increase again above this level. Generally as the needle hydrophone is positioned higher above the deflector plate, so the pressure peak occurs later on the pressure trace. This is to be expected because of the extra distance the shock wave must travel before reaching the tip of the needle hydrophone as it is raised. The time at which the pressure peak occurs does not appear to be highly dependent on the shock tube driver pressure or water level used. Most of the pressure peaks are followed by a negative pressure. This is thought to be an expansion wave originating at the corners of the deflector plate and inside edge of its supporting flange. Initially the negative pressure

is recorded about 8ms after the pressure peak, but this time interval decreases as measurements are taken further away from the deflector plate. Such behaviour is consistent with an expansion wave which gradually steepens and catches up with the travelling shock wave ahead. Some tests recorded a negative pressure ahead of the pressure peak. This phenomenon was not consistent and its source is unknown

As noted above, redesign of the deflector plate assembly was required. In the new design, the deflector plate was welded onto a thin wall stainless steel bellow to allow it vertical flexibility. A displacement limiter surrounded the bellow to prevent excessive movement. This displacement limiter also had the advantage of preventing any unwanted hydrodynamic effects from fluid flow around the bellow convolutions. To produce a water jet with the bellow deflector plate assembly required a greater shock tube driver pressure than a similar water jet using the original deflector plate assembly discussed above. Furthermore, a number of the initial water jets produced were lopsided -- probably due to fabrication imbalances in the bellow. This improved as testing progressed. The water jets produced using the bellow system are generally smaller, broader and less coherent than those produced by the foam ring deflector plate assembly. They also have a larger rise time. These differences reflect the larger mechanical inertia of the bellow mounted deflector plate compared to its foam ring mounted equivalent. Therefore, to achieve the most efficient energy transfer between shock wave and resulting water jet it is necessary to minimise the mass and inertia of the deflector plate assembly. Despite its greater inertia, the major advantages gained from the bellow deflector plate assembly were consistency and reliability. Once installed in the test rig, no further attention was required throughout testing.

When photographing the water jets produced with the bellow system, streaking of the water surface was noted before the actual water jet developed. This is a similar phenomenon to that documented by Mortimer (1997) under similar experimental conditions. The similarity between the two can be seen below.

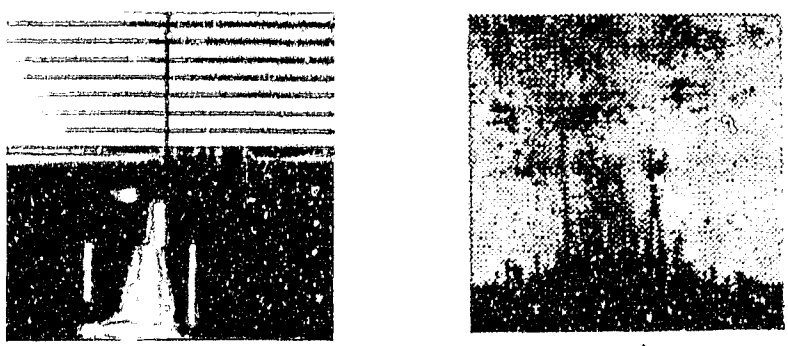

(a) (b)

Figure 7.1 Streaking produced (a) with bellow flange assembly (b) by Mortimer (1997)

Mortimer noted that the streaking represents high speed water particles energised and torn from the water surface as a passing shock wave is reflected from the water/air interface at the free water surface. On the other hand, the actual water jet results from the overall hydrodynamic flow initiated by movement of the curved deflector plate.

The pressure measurement tests conducted with the bellow system were for a constant water level. The recorded pressure amplitudes were generally lower than those recorded with the foam ring deflector plate assembly, while the actual pressure traces adopt a noticeably different form. Inertia of the bellow and displacement limiter, as well as drag created by fluid flow around them, are thought to limit the pressure amplitudes achievable with this system. The same forces damp the system's response to impulsive shock wave loading, resulting in a number of smaller high pressure peaks recorded by the needle hydrophone as opposed to one large peak. These differences are shown below.

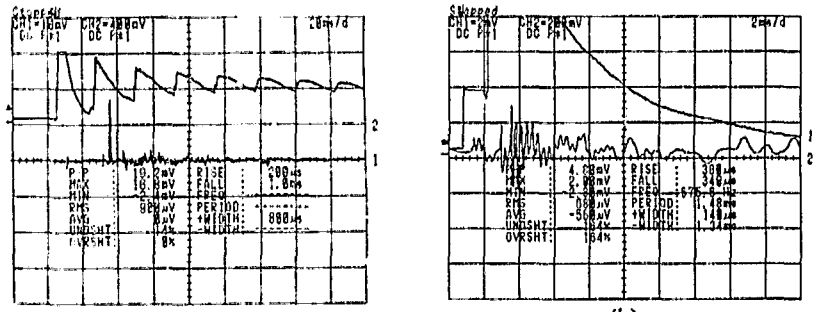

(a) (b)

Figure 7.2 Qualitative difference in pressure trace recorded with:
(a) Foam ring deflector plate assembly
(b) Bellow system deflector plate assembly

For the bellow system, the largest pressure peaks were recorded closest to the deflector plate. Their amplitude decreased with decreasing distance to the water surface. Close to the water surface the pressure peak was hardly visible on the pressure trace. Despite this, as needle hydrophone distance away from the deflector plate increased, the pressure traces recorded change from a number of distinct pressure peaks to one peak. This is attributed to diffraction and near-field edge effects. Pressure fields were calculated at 5mm height increments between deflector plate and water surface. These are instructive but it must be noted that they are based on tests which in many instances were not repeatable. The pressure fields show an almost smooth transition from higher to lower pressures with increasing distance above the deflector plate. Thus the pressure waves set up by the deflector plate are damped by the water above. This is in contradiction of results obtained with the foam ring deflector plate assembly, where pressure increases with increasing distance above the deflector plate. The foam ring deflector plate assembly has a lower inertia than the bellow system assembly with displacement limiter. Therefore it causes greater water particle velocities in the water tank. The moving water particles are directed towards the geometric focus of the deflector plate. This movement is reflected in the increasing pressures recorded by the needle hydrophone when approaching the focal point. The bellow system deflector plate assembly, with its own response to the impulsive shock wave loading damped by its mechanical properties, does not initiate water movement on the same scale as the foam ring assembly.

Photographic results show dark clouds between the water surface and deflector plate assembly during testing. Resolution is inadequate to make a definite statement but it is thought that these clouds represent cavitation bubbles. Such bubbles, if impacting on the tip of the needle hydrophone must have some effect on the pressure trace recorded. When high pressure air was forced past the silicon seal of the deflector plate assembly it resulted in large repetitive pressure peaks and troughs being recorded. Similarly cavitation bubbles behind the passing shock wave could be responsible for the pressure fluctuations recorded behind the initial high pressure peaks.

During the course of experimentation, non-linear dynamic analysis software (Autodyn) became available with the capability to simulate the physical experimental situations already discussed. Although a number of idealisations were required, a simulation was set up which represented a curved deflector plate, driven forward by a high pressure region behind it, impacting a fluid from below. The water ahead of the deflector plate is forced outwards to the side, creating a cavity in the water. In time this cavity collapses and the kinetic energy of the moving water is focused into a central eruption which emerges from the water surface as a water jet. The form of this jet matches closely those photographed by the author during experimentation. Its mechanism of formation is similar to that hypothesised by Kedrinskii (1978) and visualised by Zeff et al.(2000).

8. Conclusions

It has been shc wn that it is possible to use a deflector plate driven by the high pressure behind a passing shock wave as a mechanical analogue of the FEMAS documented by Mortimer (1997). The free surface water jets produced vary in form, shape and speed depending on the mechanical design of the test equipment. The overall hydrodynamic flow initiated by movement of the deflector plate using the present experimental equipment represents a complex coupled system whose physical properties are inherently subject to scatter and variation. This hinders interpretation of the physical measurements undertaken during experimentation.

Non-linear dynamic analysis software can be used to simulated the water jet phenomenon observed experimentally with good correlation between the experimental and simulated results. This type of simulation allows a means of exploring the effects of varying experimental parameters such as water depth and shock strength. Furthermore the simulation offers insight into the mechanism of formation of the water jets . This confirms that the water jet results from collapse of a cavity which forms below the water surface.

Zeff et al.(2000) documented an alternative mechanical system which produces free surface water jets by vertically exciting a free water surface. The resulting water jet is of exceptional form and concentration, suggesting that this type of system holds advantages over the FEMAS and its shock tube based analogue.

Recommendations

A better understanding of the physical characteristics of free surface water jets is required before they can be used in industrial applications. The most promising experimental tools for further studies are computer simulations and test rigs which harmonically excite the water surface. Future studies could concentrate on characterising the free surface water jets according to a fundamental experimental parameter such as amplitude of excitation as well as quantifying the energy available within the jet to do useful work and its distribution throughout the jet formation process.

8. References

- Ben-Dor G (1992) Shock wave reflection phenomena, Springer-Verlag New York.
- Grönig H (1985) Shock wave focusing phenomena. In: Bershader D, Hanson R (eds) Proceedings of the 15th International Symposium on Shock Tubes and Waves (Stanford). Stanford University Press, pp 43-56
- Karnovsky H (1998) Production of free surface water jets using focused underwater shock waves. BEng (Mech) final year research project, University of the Witwatersrand
- Kedrinskii VK (1978) Surface effects from an underwater explosion (review). Zh. Prikl. Mekh. Tekh. Fiz. 4: 66-87
- Keller JB (1954) Geometrical Acoustics I. The theory of weak shock waves. J. Applied Physics (25)8: 938-947
- Lesser MB, Field JE (1983) The impact of compressible liquids. Ann. Rev. Fluid Mech. 15: 97-122
- Mortimer BJP (1997) Liquid Wave Focusing and the Production of Pulsed Jets. PhD Dissertation, University of the Witwatersrand, Johannesburg
- Mortimer BJP, Skews BW, Jongens AWD (1995) The feasibility of using pulsed water jets for material sorting. Journal of the South African Acoustics Institute (JSAAI) 6: 23-33
- Müller M (1987) Experimental investigations on focusing of weak spherical shock waves in water by shallow ellipsoidal reflectors. Acoustica 64: 85-93
- Müller M (1989) Focusing of shock waves in water by different ellipsoidal reflectors. In: Kim YW (ed) AIP conference proceedings 208: Current topics in shock waves – 17th International symposium on shock waves and shock tubes (Bethlehem, PA). American Institue of Physics, pp143-148
- Nishida M, Kishige H (1987) Numerical simulation of focusing process of reflected shock waves. In: Grönig H (ed) Proceedings of the 16th International Symposium on Shock Tubes and Waves (Aachen), pp 551-557
- Platte M (1985) A polyvinylidene fluoride needle hydrophone for ultrasonic applications. Ultrasonics May 1985: 113-118

- Reichenberger H (1988) Lithotripter systems. Proc IEEE 76(9): 1236-1246
- Štuka Č, Šunka P, Benes J (1995) Nonlinear transmission of focused shock waves in nondegassed water. In: Brun R, Dumitrescu LZ (eds) Proceedings of the 19th ISSW (Marseille). Springer-Verlag, Berlin Heidelberg, pp 445-448
- Sturtevant B, Kulkarny VA (1976) The focusing of weak shock waves. J. Fluid Mech. 73(4): 651-671
- Takayama K, Esashi H, Sanada N (1983) Propagation and focusing of spherical shock waves produced by underwater microexplosions. In: Archer R, Milton B (eds) Proceedings of the 14th ISSW (Sydney). New South Wales University Press, Sydney, pp 553-562
- Whitham GB (1958) On the propagation of shock waves through regions of non-uniform area or flow. Journal of Fluid Mechanics 4: 337-360
- Wright JK (1961) Shock tubes, Methuen and Co LTD
- Zeff BW, Fineberg J, Lathrop DP (1999) Formation of a self-focusing singularity on a fluid surface. Physics of Fluids 11(9): S8
- Zeff BW, Kleber B, Fineberg J, Lathrop DP (2000) Singularity dynamics in curvature collapse and jet eruption on a fluid surface. Nature 403: 401-404

Appendix A1

The following sequence of photographs shows the development and decay of the water jet produced by the deflector plate mounted on a foam ring.

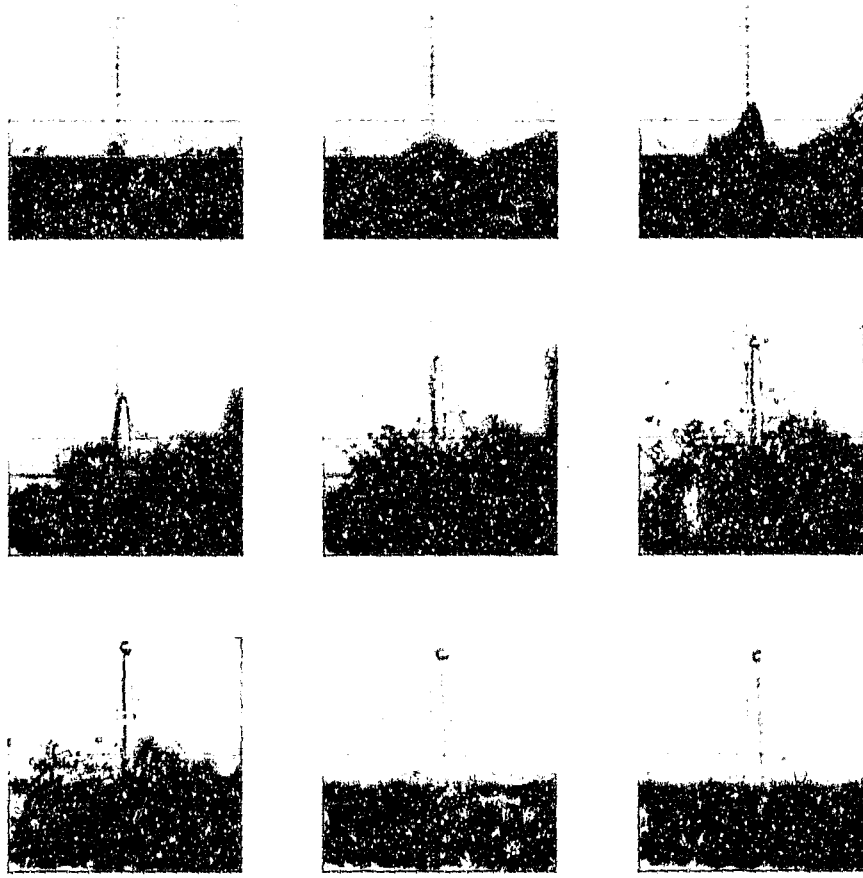

The following sequence of photographs shows the development and decay of the water jet produced by the bellow system with displacement limiter.

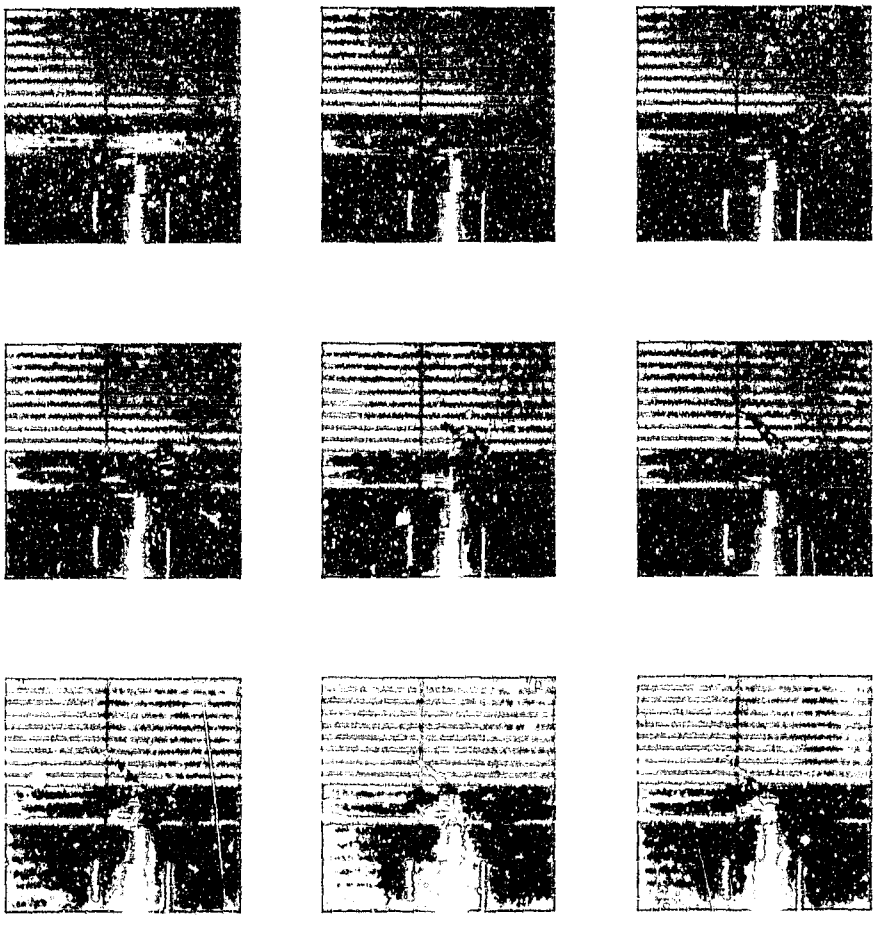

Appendix A2

ICP CALIBRATION DATA

Model 113A21
S/N 7940

Cal Range 0 - 100 PSI
Sens* 24.92 mV/PSI
Linearity* < 1.0 %FS

Input TC > 1 sec
Rise Time 1 µsec
Nat'l Freq 500 kHz
Output Imp < 100 ohms

PCB PIEZOTRONICS

By Ron Burke
Date Sep 2, 1994

* By comparison with reference standard per ISA 037.10. Zero Based best straight line.

Calibration of instrumentation used to certify this sensor is traceable to NIST.

PCB Piezotronics' calibration procedure is in compliance with MIL-STD-45662A.

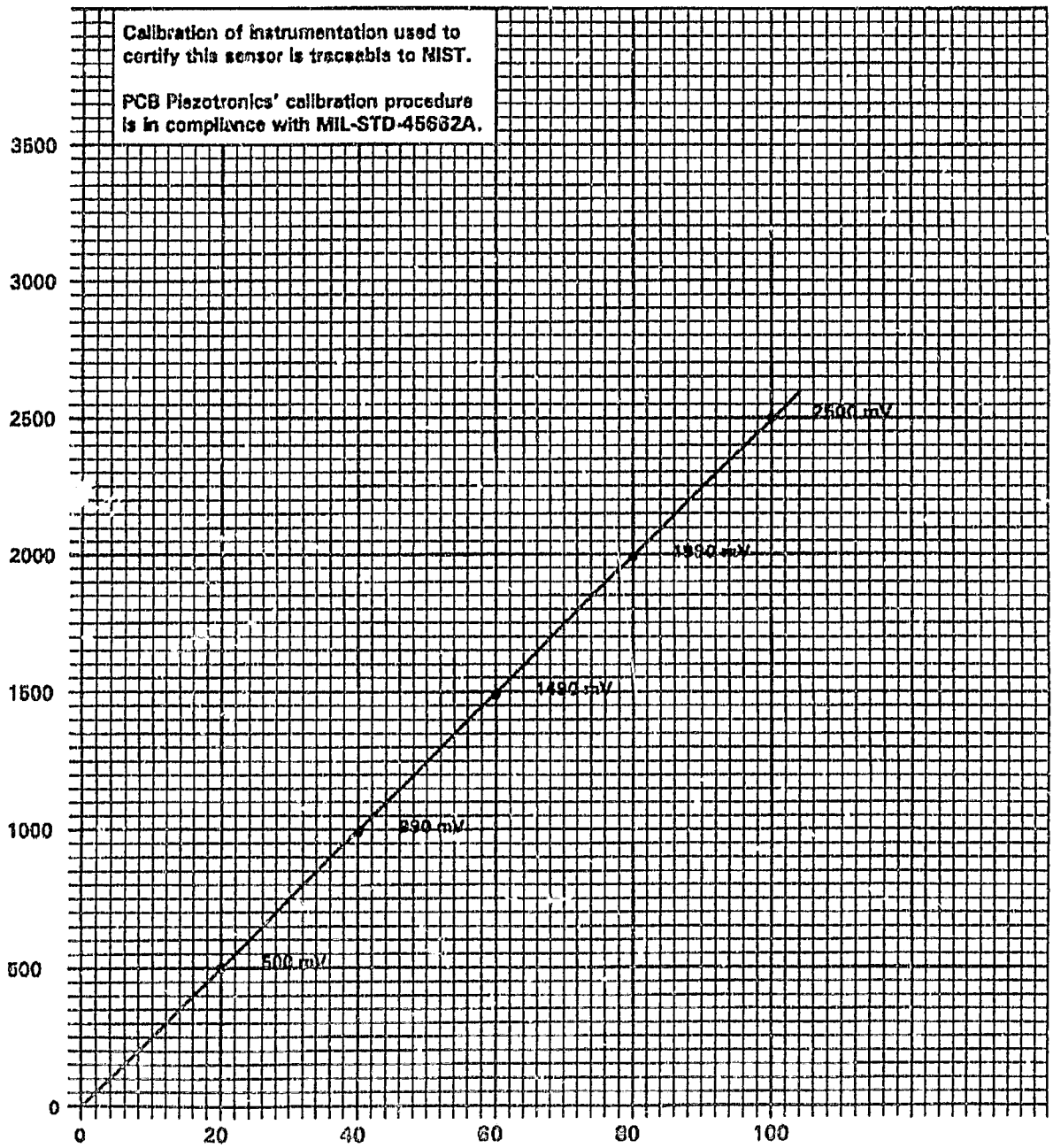

PCB PIEZOTRONICS, INC.
3425 Walden Avenue, Depew NY 14043
Tel:716-684-0001 TWX:710-263-1371

Customer
PO Number
Calibration Traceable to NIST thru project No. 737/0370-40MET49

STANDARD CABLES

Series 002 - GENERAL PURPOSE WHITE COAXIAL: General purpose coaxial cable with an extruded waterproof Teflon insulation jacket; 29 pF/ft nominal cable capacitance, 400 °F (204 °C) maximum temperature, 0.071 inch (1,8 mm) cable diameter. Suitable for most ICP® sensor applications.

Series 003 - LOW NOISE BLUE COAXIAL: High temperature, low noise cable with Teflon wrapped insulation. Internal lubricant reduces noise induced by cable motion; 29 pF/ft nominal cable capacitance, 550 °F (288 °C) maximum temperature, 0.079 inch (2,0 mm) diameter. For use with charge or ICP® sensors.

Series 010 - TRIAXIAL (4-CONDUCTOR): Twisted, shielded four-conductor cable with clear Teflon insulation jacket; 31 pF/ft nominal cable capacitance, 400 °F (204 °C) maximum temperature, 0.1 inch (2,54 mm) cable diameter. For use with ICP® triaxial sensors.

Series 012 - STANDARD BLACK COAXIAL: Low cost, black coaxial cable (RG-58/U) similar to standard household television cable; 29 pF/ft nominal cable capacitance, 140 °F (60 °C) maximum temperature, 0.195 inch (4,95 mm) cable diameter. Ideal for transmitting low impedance signals over short distances.

Series 024 - INDUSTRIAL TWISTED SHIELDED: Twisted, shielded pair with polyurethane insulation jacket; 42 pF/ft nominal cable capacitance, 250 °F (121 °C) maximum temperature, 0.25 inch (6,35 mm) cable diameter. For use with ICP® sensors in high EMI and RFI environments; 90% coverage shield.

Model Number Format: Cable type/Terminating connectors/Designated length
(For example: Model 002A10 is a 10 ft. 002 type cable terminating an 10-32 coaxial connectors.)

10-32 Coaxial Plug to 10-32 Coaxial Plug

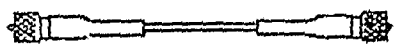

Length:	Available Models:
3 ft (0,9 m)	002A03, 003A03
10 ft (3,0 m)	002A10, 003A10
20 ft (6,1 m)	002A20, 003A20
50 ft (15,2 m)	002A50, 003A50

10-32 Coaxial Plug to BNC Plug

Length	Available Models:
3 ft (0,9 m)	002C03, 003C03
10 ft (3,0 m)	002C10, 003C10
20 ft (6,1 m)	002C20, 003C20
50 ft (15,2 m)	002C50, 003C50

5-44 Coaxial Plug to BNC Plug

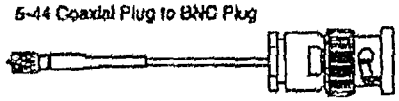

Length	Available Models:
10 ft (3,0 m)	002P10, 003P10
25 ft (7,6 m)	002P25, 003P25

Microtech (4-pin) to three BNC Plugs

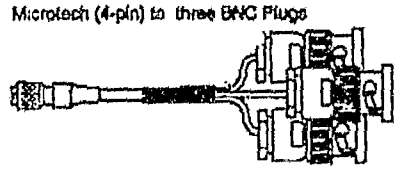

Length	Available Models:
5 ft (1,5 m)	010G05
10 ft (3,0 m)	010G10
15 ft (4,6 m)	010G15
20 ft (6,1 m)	010G20

MS3106 (Military 2-pin) to BNC Plug

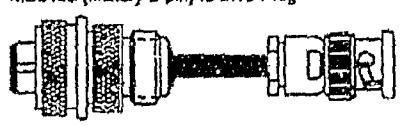

Length	Available Models:
10 ft (3,0 m)	012R10, 024R10
20 ft (6,1 m)	012R20, 024R20
50 ft (15,2 m)	012R50, 024R50
100 ft (30,5 m)	012R100, 024R100

BNC Plug to BNC Plug

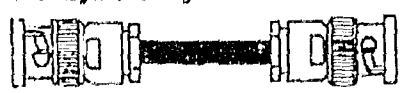

Length	Available Models:
3 ft (0,9 m)	002T03, 003D03, 012A03
10 ft (3,0 m)	002T10, 003D10, 012A10
20 ft (6,1 m)	002T20, 003D20, 012A20

Other lengths and cable types are available . . . consult PCB.

PIEZOTRONICS

PCB PIEZOTRONICS INC. 3425 WALDEN AVENUE • DEPEW, NEW YORK 14043-2495 • PHONE 716-684-0001 • FAX 716-684-0987

Appendix A3

Müller-Platte-Gauge

Piezoelectric Micro Pressure Gauge for High Frequency Ultrasound- and Shock Wave Measurements in Liquids

Typical Applications

The Müller-Platte Gauge was invented a t the University of Aachen 1985 for measurements of high frequency pressure waves in water. Today this probe is the Gold-Standard for pressure measurements of high energy pressure amplitudes. Within these years the Müller-Platte gauge has demonstrated its reliability and durability in multiple experiments worldwide, especially under very high shock wave pressures.

This special gauges is designed for high energy ultrasound measurements as well as for recording blast waves in water up to some kbar. By its small sensitive diameter less than 0,5 mm and the very short rise time of about 50 ns the gauge is the ideal device for distribution measurements especially in focal regions of ultrasonic transducers or e.g. kidney stone lithotriptors.

Other applications are measurements of laser generated shock waves, cavitation effects or applications in the medical research.

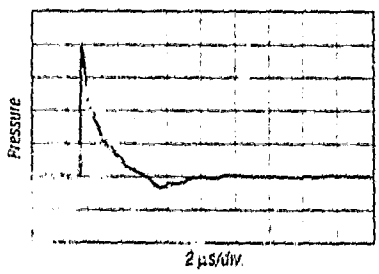

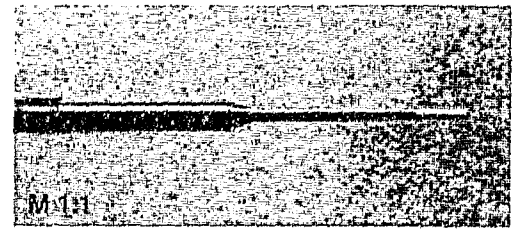

Technical Data:

Pressure range:	-100 to 2000 bar
Calibration:	Shock wave calibration up to 10 bar in water. (Const. sensitivity could be verified up to 320 bar)
Rise time:	50 ns*
Sensitive diam.:	< 0,5 mm
Sensitivity:	Const. up to 10 MHz about 0.5 mV/bar* (incl. 2 m cable)
Tube diam.:	1.2 mm at the tip, 4.0 mm for mounting, stainless steel
Recording:	e.g. to a 1 MOhm Input
Article-No.:	100-100-1
Extent of supply:	Micro pressure gauge with 2 m cable and BNC plug with protective case

M. Müller, M. Platte
Einsatz einer breitbandigen Drucksonde auf PVdF-Basis zur Untersuchung kohärenz erender Stoßwellen in Wasser
Acustica vol. 58, 1985, S. 213-222

M. Müller
Experimental investigations on Focusing of Weak Spherical Shock Waves in Water by Small Ellipsoidal Reflectors
Acustica vol. 64, 1987, S. 85-93

K. Sasaki, G. De Jeneratz, R. P. Salathé
Fragmentation process induced by nanosecond laser pulses
Appl. Physics Letters Vol. 61 (22), 1992

For special applications the gauge can be delivered in nearly any wished size and shape or with different cable length. Please give detailed information (incl. drawing) about your wished application and ask for an offer.

* All gauges are individually different. By this these technical data can vary within 30 %.

Dr. Michael Müller Ingenieurtechnik · Im Brockenfeld 3 · D-52074 Aachen
Telefon/Fax ++49 (0)2 41/70 99 90

Instruction Manual
for
Müller-Platte Needle Gauge

How to use the Müller-Platte Needle Gauge:

This sensor is only designed for fast and high pressure measurements in water. If you want to use it for other liquids than water the probe has to be calibrated in the new enviroment.

1. The sensitivity of the gauge is defined to:

$$U_{probe} = Q_{probe} / C_{sum}$$

In the above equitation

U_{probe}	means the sensitivity of the probe in Volt/bar
Q_{probe}	means the sensitivity of the probe in pC/bar
C_{sum}	is the sum of probe capacity, the capacity of the connected device and , if necessary the capacity of an extension cable in pF

2. For measurements the Needleprobe has to be connected to the 1 MOhm input of a recorder, oscilloscope etc.

3. Do not use or store the Müller-Platte Needleprobe in temperatures beyond 60°C because of depolarisation of the sensor.

4. Do not use the Needleprobe in water for more than 5 hours due to diffusion of water into the sensor material. Start next application after a break of at least 3 hours.

5. To avoid electromagnetic distortion the top of the sensor is coated with a silver ink. During use this might be distroyed due to cavitation effects.Therefore it is recommended to check periodically the coating.
If necessary renew the coating by removing the old coating carefully with a soft paper soaked with acetone and then apply a new thin film of silver coating.

6. The tip of the Needleprobe is very sensitive. Avoid any mechanical stress. The tip can be distroyed

7. . The lifetime of the gauge is limited due to cavitation erosion. You can evaluate it as follows:
100 bar pressure wave × 2000 single measurements = const.

Muller Ingenieurtechnik Dr.-Ing. Michael Muller Im Brockenfeld 3 52074 Aachen Germany Tel./Fax: +49-241 70 99 90
Advance Bank Postbankk Köln Geschäftsführer: Sitz des Unternehmens:
Konto 100 275 1608 Konto 139889-509 Dr.-Ing. Michael Müller Aachen
BLZ 702 300 00 BLZ 370 100 50

Appendix A4

The following is a macro file generated by Autodyn, recording the keystrokes for a typical simulation setup. It excludes the definition of gravity in the negative x direction, which can be found in the global menu under the options submenu.

```
f5
$Mirror
%
Yes
No
$Global
$Material
$Library
%
EXAMPL
$Retrieve
%
YES
NO
NO
NO
NO
NO
NO
NO
NO
NO
NO
#Retrieve this material?
Yes
$Library
%
COMPDS
$Retrieve
%
NO
NO
NO
YES
#Retrieve this material?
Yes
$Library
%
HULL00
$Retrieve
%
NO
NO
NO
```

NO
NO
NO
NO
NO
NO
YES
NO
NO
NO
NO
NO
%
NO
#Retrieve this material?
Yes
Esc
Esc
Esc
$Subgrid
%
SHOCK
%
Euler
%
60
30
$Zoning
$IJ-Range
%
1
30
1
30
$Generate
$Edge
$J-varies
$Arc
%
30
1.00000E+00
6.70000E+01
0.00000E+00
%
7.00000E+00
0.00000E+00
%
1.50000E+01
3.00000E+01
$I-varies

```
$Line
%
       1
  1.00000E+00
%
  0.00000E+00
  0.00000E+00
$J-varies
Esc
$I-varies
$Line
%
      30
  1.00000E+00
%
  0.00000E+00
  3.00000E+01
$J-varies
$Line
%
       1
  1.00000E+00
Esc
$Block
$Jstraight
%
  1.00000E+00
Esc
$View/Mod
Esc
Esc
Esc
Esc
Esc
$Save
%
TRY520
#Overwrite existing file?
Yes
$Modify
$Subgrid
%
SHOCK
$Zoning
$IJ-Range
%
      30
      60
       1
      30
```

```
$Generate
$Edge
$I-varies
$Line
%
      30
  1.00000E+00
%
  2.50000E+01
  3.00000E+01
$I-varies
$Line
%
       1
  1.00000E+00
%
  2.50000E+01
  0.00000E+00
$J-varies
$Line
%
      60
  1.00000E+00
Esc
$Block
$Jstraight
%
  1.00000E+00
Esc
$View/Mod
Esc
Esc
Esc
Esc
Esc
$Save
%
TRY520
#Overwrite existing file?
Yes
$Modify
$Subgrid
%
SHOCK
$Zoning
$IJ-Range
%
       1
      30
       1
```

```
      30
Esc
$Fill
$Block
%
       1
      30
       1
      30
GAIR
%
 5.01900E+00
 6.73328E+05
 2.92484E+02
 0.00000E+00
 0.00000E+00
$Block
%
      30
      60
       1
      30
VOID
Esc
Esc
$View
$Matplot
$Location
Esc
Esc
Esc
Esc
$Save
%
TRY520
#Overwrite existing file?
Yes
$Modify
$Subgrid
%
DEFLECTOR
%
Lagrange
%
       3
      30
$Zoning
$Generate
$Edge
$J-varies
```

```
$Arc
%
       1
  1.00000E+00
  6.70000E+01
  0.00000E+00
%
  7.00000E+00
  0.00000E+00
%
  1.50000E+01
  3.00000E+01
$J-varies
$Arc
%
       3
  1.00000E+00
  6.70000E+01
  0.00000E+00
%
  9.00000E+00
  0.00000E+00
%
  1.70000E+01
  3.00000E+01
$I-varies
$Line
%
      30
  1.00000E+00
$I-varies
$Line
%
       1
  1.00000E+00
Esc
$View/Mod
Esc
$Block
$Jstraight
%
  1.00000E+00
Esc
Esc
Esc
$Fill
$Block
%
       1
       3
```

```
        1
       30
STNL.STEEL
%
  7.86000E+00
  1.34100E+05
  0.00000E+00
  0.00000E+00
  0.00000E+00
Esc
Esc
$View
$Matplot
$Location
Esc
Esc
Esc
Esc
$Save
%
TRY520
#Overwrite existing file?
Yes
$Modify
$Subgrid
%
WATER
%
Lagrange
Esc
$Subgrid
%
WATER
%
Euler
%
       35
       30
$Zoning
$IJ-Range
%
        1
       15
        1
        6
$Generate
$Edge
$J-varies
$Arc
%
```

```
      1
 1.00000E+00
 6.70000E+01
 0.00000E+00
%
 9.00000E+00
 0.00000E+00
%
 1.70000E+01
 3.00000E+01
$I-varies
$Line
%
      1
 ' 00000E+00
%
 2.50000E+01
 0.00000E+00
$J-varies
$Line
%
     15
 1.00000E+00
%
 2.50000E+01
 3.00000E+01
Esc
Esc
$IJ-Range
%
      1
     15
      6
     30
$Generate
$Edge
$J-varies
$Line
%
      1
 1.00000E+00
%
 1.70000E+01
 3.00000E+02
$I-varies
$Line
%
     30
 1.00000E+00
%
```

```
 2.50000E+01
 3.00000E+02
$J-varies
$Line
%
      15
 1.00000E+00
Esc
Esc
$IJ-Range
%
       1
      15
       1
      30
$Generat.
$Block
$Jstraight
%
 1.00000E+00
Esc
Esc
$IJ-Range
%
      15
      35
       1
      30
$Generate
$Predefs
$Box
%
 3.50000E+01
 4.25000E+02
 0.00000E+00
      20
Centered
 0.00000E+00
 3.00000E+02
 0.00000E+00
      29
Centered
Esc
Esc
$View
Esc
Esc
$Fill
$Block
%
```

1
21
1
30
WATER
%
9.98000E-01
4.59008E+04
0.00000E+00
0.00000E+00
0.00000E+00
$Block
%
21
35
1
30
GAIR
%
1.22500E-03
1.91441E+05
0.00000E+00
0.00000E+00
0.00000E+00
$View
$Materials
$Location
Esc
Esc
Esc
Esc
Esc
$View
$Matplot
$Location
Esc
Esc
Esc
Esc
$Save
%
TRY520
#Overwrite existing file?
Yes
f5
$Mirror
%
Yes
No
$Modify

```
$Global
$Edit
$Makeslide
$Matplot
$Location
$Cycles
%
       0
  999999
     200
Esc
$Vecplot
$Cycles
%
       0
  999999
     200
%
 0.00000E+00
      10
 0.00000E+00
 0.00000E+00
 1.00000E+00
Esc
$Conplot
$Cycles
%
       0
  999999
     200
%
PRESSURE
%
      10
 0.00000E+00
 0.00000E+00
 1.00000E+00
Esc
Esc
Esc
Esc
Esc
$Save
%
TRY520
#Overwrite existing file?
Yes
$Modify
$Interact
$Eul/Lag
```

$Polygons
$Gen/Mod
%
DEFLECTOR
$Zoom
$Zoom
$Insert
Esc
Esc
$Add
%
DEFLECTOR1
DEFLECTOR
SHOCK
$Add
%
DEFLECTOR2
DEFLECTOR
WATER
$View
$Next
Esc
Esc
Esc
Esc
$Save
%
TRY520
#Overwrite existing file?
Yes
$Modify
$Subgrid
%
SHOCK
$Options
$Active
%
 0.00000E+00
 5.00000E-02
Esc
Esc
$Subgrid
%
DEFLECTOR
$Options
$Active
%
 0.00000E+00
 5.00000E-02
Esc

Esc
Esc
$Save
%
TRY520
#Overwrite existing file?
Yes
f6
Y